UNIVERSITÄT FÜR BODENKULTUR WIEN
University of Natural Resources
and Life Sciences, Vienna

# Doctoral Dissertation

## Hydrodynamic and Sediment Transport CFD Modelling on different Scales

submitted by

DI Daniel WILDT, MSc

in partial fulfilment of the requirements for the academic degree

Doktor der Bodenkultur (Dr.nat.techn.)

Vienna, May 2022

Supervisor:

Ass.Prof. Priv.-Doz. Dipl.-Ing. Dr.techn. Michael Tritthart
Institute of Hydraulic Engineering and River Research
Department of Water, Atmosphere and Environment

This thesis is submitted in partial fulfilment of the requirements of the degree of Doktor der Bodenkultur (Dr.nat.techn.)

University of Natural Resources and Life Sciences, Vienna

Title

# Hydrodynamic and Sediment Transport CFD Modelling on different Scales

Supervisor

**Ass.Prof. Priv.-Doz. Dipl.-Ing. Dr.techn. Michael Tritthart**
University of Natural Resources and Life Sciences, Vienna
Department of Water, Atmosphere and Environment,Institute of Hydraulic Engineering and River Research
Muthgasse 107, 1190 Vienna, Austria

Additional members of the advisory board

**Priv.-Doz. Dipl.-Ing. Dr.nat.techn. Christoph Hauer and Univ.Prof. Dipl.-Ing. Dr.nat.techn. Dr.h.c. Helmut Habersack**
University of Natural Resources and Life Sciences, Vienna
Department of Water, Atmosphere and Environment,
Institute of Hydraulic Engineering and River Research
Muthgasse 107, 1190 Vienna, Austria

submitted by

**Dipl.-Ing. Daniel Wildt, MSc**
01140454
Email: dw.wildt@gmail.com

24th May 2022

## Acknowledgements

My sincerest thanks to my PhD project supervisor Ass.Prof. Priv.Doz. Dipl.-Ing. Dr.techn. Michael Tritthart for his support and patience in numerous conversations answering all my questions in highest detail. His wide, in-depth knowledge, precision, focus and also targeted way of working provided me the optimum environment for the completion of this thesis. I would also like to mention the additional members in my advisory team Priv.-Doz. Dipl.-Ing. Dr.nat.techn. Christoph Hauer as well as Univ.-Prof. Dipl.-Ing. Dr.nat.techn. Dr.h.c. Helmut Habersack for their continuous support and feedback. Thanks also to my colleagues and friends for an inspiring time at university. I would also like to mention Sencer Yücesan, MSc, we formed a high performing team during our PhD research, having numerous fruitful discussions on CFD and LES modelling. Finally massive thanks to my family and Antonia Spitzer, BSc for their support throughout my studies.

## Funding

This thesis was written as a contribution to the Christian Doppler Laboratory for Sediment Research and Management. In this context, the financial support by the Christian Doppler Research Association, the Austrian Federal Ministry for Digital and Economic Affairs and the National Foundation for Research, Technology and Development is gratefully acknowledged.

The computational results have been achieved using the Vienna Scientific Cluster (VSC).

# Affidavit

I hereby declare that I have authored this dissertation independently, and that I have not used any assistance other than that which is permitted. The work contained herein is my own except where explicitly stated otherwise. All ideas taken in wording or in basic content from unpublished sources or from published literature are duly identified and cited, and the precise references included. Any contribution from colleagues is explicitly stated in the authorship statement of the published papers.

I further declare that this dissertation has not been submitted, in whole or in part, in the same or a similar form, to any other educational institution as part of the requirements for an academic degree.

I hereby confirm that I am familiar with the standards of Scientific Integrity and with the guidelines of Good Scientific Practice, and that this work fully complies with these standards and guidelines.

Vienna, 24th May 2022

Daniel Wildt *(manu propria)*

## Abstract

Sediment management is becoming an increasingly important challenge in river engineering. Measures for maintaining sediment continuity require detailed understanding of underlying transport processes on different scales. Hence the aim of this research is to study hydrodynamic processes related to sediment transport with respect to their process scale using computational fluid dynamics (CFD).

Hydrodynamics and sediment transport have been modelled with different levels of turbulence resolution and particle-fluid momentum coupling. The unsteady development of a sediment plume was studied using a fully two-way coupled Euler-Lagrange large-eddy simulation (LES) model. Results suggest that this transport process undergoes three phases: (i) acceleration phase, (ii) transport phase and (iii) deposition phase. Sediment transport is characterized by different processes in those phases. This needs to be considered for parametrization of sediment transport in large-scale models. Using a second LES model forces on a sediment particle mounted to the channel bed at different exposure levels were studied. Results show strong influence of very large-scale coherent motion on particle entrainment.

An in-house code for the solution of the Reynolds-averaged Navier-Stokes equations (RANS) for rivers has been extended to model particle-driven gravity currents in reservoirs. Validation showed good agreement of model results with experimental data from literature. The developed model can serve as a strategic evaluation tool for optimising sediment management in reservoirs. In addition the implementation of buoyant forces can be an efficient parametrization of processes during the development of a sediment plume as they have been observed on the small-scale LES model.

***Keywords:*** Computational fluid dynamics, Large-eddy simulation, Multiphase flow, Reynolds-averaged simulation, Sediment;

## Zusammenfassung

Sedimentmanagement wird zu einer größer werdenden Herausforderung im Flussbau. Maßnahmen zur Erhaltung der Sedimentdurchgängigkeit erfordern detailliertes Verständnis der zugrunde liegenden Transportprozess auf verschiedenen Skalen. Ziel dieser Arbeit ist die Untersuchung von Hydrodynamik in Verbindung mit Sedimenttransportprozessen unter Berücksichtigung der Prozessskala mittels numerischer Simulationen (CFD).

Hydrodynamische Strömungen und Sedimenttransport wurden mit unterschiedlichem Detaillierungsgrad der Turbulenzauflösung und des Impulsaustausches zwischen Partikeln und Fluid modelliert. Die instationäre Entwicklung einer Sedimentwolke wurde mit einem Euler-Lagrange LES-Modell unter vollständiger Berücksichtigung des Impulsaustausches zwischen Wasser und Sediment untersucht. Aus den Simulationsergebnissen sind drei Phasen dieses Transportprozesses erkennbar: (i) Beschleunigungsphase, (ii) Transportphase und (iii) Ablagerungsphase. Sedimenttransport wird in diesen Phasen durch unterschiedliche Prozesse charakterisiert. Dies muss bei einer Parametrisierung des Sedimenttransports in großskaligen Modellen berücksichtigt werden. Mittels eines zweiten LES-Modells wurden Kräfte auf ein an der Sohle befestigtes Sedimentpartikel unter verschiedenen Abschirmungsgraden untersucht. Die Ergebnisse zeigen einen starken Einfluss von sehr großen Turbulenzstrukturen auf den Bewegungsbeginn.

Ein In-House Code zur Lösung der Reynolds gemittelten Navier-Stokes Gleichungen (RANS) für Flüsse wurde zur Modellierung von Trübeströmungen in Speichern erweitert. Die Validierung zeigte gute Übereinstimmung der Modellergebnisse mit Daten von Experimenten aus der Literatur. Das entwickelte Modell kann als Werkzeug zur Planung von Sedimentmanagement in Speichern verwendet werden. Zusätzlich kann die Implementierung der Auftriebskräfte eine effiziente Parametrisierung von Prozessen darstellen, die im Zuge der Entwicklung der Sedimentwolke im feinskaligen LES Modell beobachtet wurden.



***Schlagworte:*** Numerische Strömungsmodellierung, Large-eddy simulation, Mehrphasenströmung, Reynolds-gemittelte Strömungssimulation, Sediment;

# Contents

# List of Abbreviations

| | |
|---|---|
| BOKU | University of Natural Resources and Life Sciences, Vienna |
| CFD | Computational fluid dynamics |
| DNS | Direct numerical simulation |
| FVM | Finite volume method |
| IAHR | International Association for Hydro-Environment Engineering and Research |
| LES | Large eddy simulation |
| MDPI | Multidisciplinary Digital Publishing Institute |
| MP-PIC | Multiphase particle-in-cell method |
| OpenFOAM | Open source field operation and manipulation |
| PISO | Pressure implicit split operator |
| RANS | Reynolds-averaged Navier-Stokes equations |
| RSim-3D | River simulation in 3D |
| SCI | Scientific Citation Index |
| SIMPLE | Semi-implicit method for pressure-linked equations |
| SPH | Smooth-particle hydrodynamics |
| SSIIM | Sediment simulation in intakes with multiblock option |
| VLSM | Very large-scale motion of coherent structures |

# Nomenclature

## Latin symbols

$c$ .................... volumetric particle concentration $[c] = 1$
$\boldsymbol{F}_b$ .................. buoyant force $[\boldsymbol{F}_b] = \mathrm{N}$
$f$ .................... particle distribution function $[f] = \mathrm{s\,kg^{-1}\,m^{-4}}$
$\boldsymbol{g}$ .................... acceleration due to gravity $[\boldsymbol{g}] = \mathrm{m\,s^{-2}}$
$\boldsymbol{g}'$ ................... reduced gravitational acceleration $[\boldsymbol{g}'] = \mathrm{m\,s^{-2}}$
$k$ .................... turbulent kinetic energy $[k] = \mathrm{m^2\,s^{-2}}$
$R$ ................... effective density ratio $[R] = 1$
$St$ ................... particle Stokes number $[St] = 1$
$S_\phi$ ................... source term of $\phi$
$t$ .................... time $[t] = \mathrm{s}$
$\boldsymbol{u}$ ................... fluid velocity $[\boldsymbol{u}] = \mathrm{m\,s^{-1}}$
$\boldsymbol{v}$ .................... particle velocity $[\boldsymbol{v}] = \mathrm{m\,s^{-1}}$
$y^+$ .................. dimensionless wall distance $[y^+] = 1$

## Greek symbols

$\Gamma$ .................... diffusivity of a conservative property
$\epsilon$ .................... rate of dissipation of $k$ $[\epsilon] = \mathrm{J\,kg^{-1}\,s^{-1}}$
$\rho$ .................... density $[\rho] = \mathrm{kg\,m^{-3}}$
$\phi$ .................... conservative property
$\Omega$ ................... control volume

## Operators

$\nabla = \begin{pmatrix} \frac{\partial}{\partial x} \\ \frac{\partial}{\partial y} \\ \frac{\partial}{\partial z} \end{pmatrix}$ ......... Nabla operator
$\dot{\square}$ ................... Lagrangian derivative

# Part I

# Introduction

# 1 Literature review

## 1.1 Sediment management

Sediment transport plays an important role related to future challenges in hydraulic engineering (Tritthart, 2012; Hauer et al., 2018). Requirements for the ecological functioning of river ecosystems as well as for human uses of rivers and flood protection have to be balanced (IWHW, 2016; Hauer et al., 2018). Despite these increasing challenges there is only limited awareness of this issue. There are still no summarising studies on sediment management. Consequently legal frameworks such as the European Water Framework Directive (European Comission, 2000) and technical standards and norms do not specifically deal with this topic (Hauer et al., 2018).

Reservoir sedimentation is one of the challenges resulting from insufficient sediment management. Storage capacity is lost affecting energy production (Habersack et al., 2000) and sediment continuity interrupted (Boes et al., 2014; Hauer et al., 2018). Different approaches are applied to tackle the problem. In summarising literature they are categorised in different ways. Boes et al. (2014) for example group sediment management measures for reservoirs by the time they are taken with respect to the sediment dynamics:

1. Prevention of sediment inflow into the reservoir,
2. routing of sediments and
3. a posteriori removal of sediments after their accumulation inside the reservoir.

A slightly different concept of grouping sediment management measures is proposed by Hauer et al. (2018). According to their concept sediment management measures are grouped by the location they are implemented at:

1. Catchment wide measures,
2. measures in the reservoir and
3. measures at the dam.

Examples for particular sediment management strategies are reduction of sediment inflow through measures reducing erosion in the catchment (group 1 according to Boes et al., 2014 and Hauer et al., 2018).

A typical measure in the reservoir (group 2 according to Hauer et al., 2018) would be dredging of sediment and dumping it downstream of the dam or reservoir flushing (e. g. Esmaeili et al., 2017; group 3 according to Boes et al., 2014). Routing of sediments (group 2 according to Boes et al., 2014) can be accomplished through sediment bypass tunnels or venting of turbidity currents. Sediment bypass tunnels typically have inlets near the entrance of the reservoir and are mainly suitable for diverting bed load (group 2 according to Hauer et al., 2018). Venting (group 3 according to Hauer et al., 2018) is most efficient for suspended sediments. They are transported through the reservoir by turbidity currents and released through bottom outlets at the dam (Boes et al., 2014).

Routing or venting of sediments are particularly appreciated for both, economical and ecological reasons. In terms of economical benefits, they allow to minimise water losses with respect to the amount of water which would be lost by flushing. As venting enables to maintain sediment continuity to a high degree impacts on ecology and river morphology are reduced (Chamoun et al., 2016).

Routing of sediments by venting or through bypass tunnels requires detailed knowledge of the path of sediment through the reservoir (Chamoun et al., 2016). The position and construction of the inlet structure of such a diversion system has to be optimized with respect to maximum potential sediment intake (IWHW, 2016). Another challenge concerning sediment bypass tunnels is invert abrasion which is observed on such structures (Auel, 2014; IWHW, 2016).

## 1.2 Sediment transport equations

For any of the above described sediment management strategies for reservoirs detailed process understanding of the particular sediment transport processes can substantially increase their efficiency (Hauer et al., 2018). Currently literature is still lacking information on sediment transport in rivers and reservoirs (Hauer et al., 2018). Models of sediment transport are often based on empirical formulas (e. g. Tritthart et al., 2011b; Deltares, 2014). Mass continuity is used in the Exner-equation for modelling bed elevation changes and river morphology (Tritthart et al., 2011c; Tritthart et al., 2011a).

Initiation of motion is one of the main processes which needs to be captured by bed load transport formulas (see also Section 1.3 below). Deterministic bed load equations are based on the assumption of Du Boys (1879) stating that bed load is transported in layers with highest velocities in the top layer and a balance of bed shear stress and bed resistance in the lowest layer (Tritthart et al., 2011b). Hence initiation of motion is based on a critical flow velocity (e. g. Hjulström, 1935), specific flow rate (e. g. Schoklitsch, 1934), water depth or bed shear stress

(e. g. Shields, 1936).

Deterministic equations proposed for modelling bed load by Tritthart et al. (2011b) or implemented in the Delft3D modelling suite (Deltares, 2014) were developed by Meyer-Peter and Müller (1948), Engelund and Hansen (1967), van Rijn (1984a), Parker (1990), Rickenmann (1991), van Rijn (1993), Wu et al. (2000), Wilcock and Crowe (2003) and Gaeuman et al. (2009). The equation by Meyer-Peter and Müller (1948) has been modified by Hunziker (1995) for better representation of armouring effects. Smart and Jäggi (1983) extended the equation of Meyer-Peter and Müller (1948) for slopes up to 20 %. Rickenmann (1991) and Rickenmann (2001) also studied bed load transport for a wide range of bed slopes up to 17 %. In addition Rickenmann (1991) took suspended sediment concentrations up to 22.7 % into account resulting in higher transport rates due to increased density (Tritthart et al., 2011b). Equations by Engelund and Hansen (1967) and Ackers and White (1973) allow to calculate total sediment transport, i. e. the sum of bed load and suspended sediment transport (Tritthart et al., 2011b; Deltares, 2014).

Stochastic bed load equations treat initiation of motion as a probability problem. Examples mentioned by Tritthart et al. (2011b) are the equations by Einstein (1950) and Z. Sun and Donahue (2000). Their higher complexity allows more accurate results only in special cases such as unsteady flow situations with highly turbulent fluctuations. Thus they are hardly used in sediment transport models (Tritthart et al., 2011b).

Advection-diffusion equations are used in many models for modelling suspended sediment transport (Hauer et al., 2018). The equations by Rouse (1939) and Hunt and Inglis (1954) provide estimates for the concentration profile in steady turbulent flow. van Rijn (1984b) presented a method for the calculation of suspended sediment transport from depth-integrated concentration profiles.

## 1.3 Incipient motion of sediment particles

In order to enable a more accurate prediction of initiation of motion by transport equations research has been carried out investigating the forces on sediment particles. Theoretical and experimental studies found in the literature review for the study in Section 4.2 (Yücesan et al., 2021) were published by Hofland et al. (2005), Schmeeckle et al. (2007), Diplas et al. (2008), Celik et al. (2010), Dwivedi et al. (2010), Dwivedi et al. (2011), Celik et al. (2013), Amir et al. (2014) and Schobesberger et al. (2020). Smart and Habersack (2007) carried out field measurements of differential pressures in the bed of gravel bed rivers in New Zealand. Schobesberger et al. (2021) were able to prove in an experimental study that incipient motion of a particle is caused by counter rotating vortices.

Numerical simulations studying forces on a particle have been performed at high levels of turbulence resolution. Chan-Braun et al. (2011) carried out direct numerical simulations (DNS) of turbulent fluid flow in a transitionally rough regime to analyse force and torque on particles of different sizes. The data has been extended by Mazzuoli and Uhlmann (2017) for a fully rough turbulent flow regime. Chan-Braun et al. (2013) further analysed the DNS data from Chan-Braun et al. (2011) with focus on time and length scales of turbulence structures and forces and torque on particles.

Additionally H. Lee and Balachandar (2012) carried out numerical simulations of turbulent flow around particles of different sizes, fully resolving the wall and the rigid particle using an immersed boundary technique. Vowinckel et al. (2016) analysed data of a DNS of turbulent fluid flow, four-way coupled with a Lagrangian model of sediment transport. Particles at the bed were mobile and the influence of particle-particle collision events on incipient motion was shown. Mazzuoli et al. (2018) studied oscillatory flow over a wavy bottom. The bed was reconstructed with spheres from a laser scan of the bottom of a laboratory flume as it has developed during an experiment. In their numerical simulations they analysed turbulence and forces on sediment particles. Ota et al. (2019) studied bedload transport in non-uniform flow using an Euler-Lagrangian model. They quantified the spatial lag effect of bed load transport around a hydraulic structure. Equilibrium and non-equilibrium bed load transport rates were analysed for local scour around a spur and a weir type structure. The experimental setup of Schobesberger et al. (2020) has been reproduced numerically using LES by Yücesan et al. (2022).

## 1.4 Suspended sediment transport CFD modelling

Suspended sediment transport is generally modelled as two phase flow. The ambient fluid phase is mostly handled using the Eulerian approach. In some special cases, e. g. models including large solids which would be covering a high number of cells of an Eulerian fluid model, the fluid phase is modelled using the Lagrangian approach (smooth-particle hydrodynamics – SPH). Transport of the dispersed phase is modelled either on the basis of the Eulerian approach or using the Lagrangian approach. The choice of the method depends on the fraction of the volume which is occupied by particles (Ferziger and Perić, 2002). For high sediment concentrations the Lagrangian method becomes impractical (Dallali and Armenio, 2015).

Euler-Euler models (e. g. Cantero et al., 2008a; Cantero et al., 2008b; Georgoulas et al., 2010; Amoudry, 2014; Kranenburg et al., 2014; Cheng et al., 2017; Stancanelli et al., 2018a; Cheng et al., 2018b) allow to study sediment transport up to very high concentrations. A problem identified by Cheng et al. (2017) and Cheng et al. (2018b) was that despite the suitability of the Euler approach to model high particle concentrations, it is difficult to cover the wide range of particle concentrations as they are relevant for example in sheet flow.

Models based on advection-diffusion equations (Necker et al., 2002; Hsu and P. Liu, 2004; Zhong et al., 2011; An et al., 2012; Dallali and Armenio, 2015) for suspended sediment transport can be considered as one-way coupled Euler-Euler models. This approach has been extended by e. g. Zhong et al. (2011) who developed a transport equation for suspended sediment which has the same form as the classic advection-diffusion equation but accounts for additional information on particle dispersion. This was achieved through a detailed calculation of the relative velocity between particles and fluid. In addition lift force, turbulence of sediment particles and particle-particle interactions are taken into account for the diffusion coefficient. Comparisons of concentration profiles with experiments showed that the extended model by Zhong et al. (2011) is superior to the Rouse-equation (Rouse, 1939) as well as the model of Hunt and Inglis (1954). In a second study Zhong et al. (2014) further investigated the drift velocity. They derived a constitutive relation for the drift velocity solved by the perturbation approach (Druzhinin, 1995). Buoyant forces from the higher density of the sediment suspension compared to clear water can be implemented into models using the advection-diffusion equation through a source term in the fluid-momentum equation (e. g. Necker et al., 2002; An et al., 2012; Dallali and Armenio, 2015; Wildt et al., 2020).

Euler-Lagrangian models (e. g. Squires and Eaton, 1990; Vinkovic et al., 2011; Vowinckel et al., 2016; R. Sun et al., 2017; Cheng et al., 2018a; R. Sun et al., 2018; Elghannay and Tafti, 2018a; D. Liu et al., 2018; Ota et al., 2019; Wildt et al., 2022a) enable the calculation of interaction forces between individual particles and their surrounding fluid. This allows studying the effect of grain size and particle shape (Cheng et al., 2018a). Rotational motion can be included in such models in addition to translational motion (e. g. R. Sun et al., 2017; Crespo et al., 2015; Canelas et al., 2016; Canelas et al., 2017).

Lagrangian-Lagrangian models (e. g. Lobovský and Křena, 2007; Crespo et al., 2015; Canelas et al., 2016; Canelas et al., 2017; Pahar and Dhar, 2017) use meshless smooth particle hydrodynamics (SPH) to model fluid flow. Crespo et al. (2015) developed the `DualSPHysics` code for the solution of CFD models using SPH. The code also allows to study the interaction between fluid and large solid objects. Pahar and Dhar (2017) present a model for sediment transport over an erodible bed. Their fluid module is capable of solving flow inside a porous domain

(e. g. river bed) as well as free flow outside. Test cases they validated the model on include (i) steady granular (dry) flow, (ii) failure of a column made of glass beads (dry, partially submerged, fully submerged) and (iii) dambreak cases.

Turbulence resolving models using large-eddy simulation (LES) (e. g. An et al., 2012; Dallali and Armenio, 2015; R. Sun et al., 2017; Cheng et al., 2018b; D. Liu et al., 2018; Stancanelli et al., 2018a; Elghannay and Tafti, 2018b; Wildt et al., 2022a) and even DNS (e. g. Squires and Eaton, 1990; Vinkovic et al., 2011; Vowinckel et al., 2016) allow to study the influence of turbulent fluctuations on sediment transport and vice-versa. Squires and Eaton (1990) found that there are areas in the turbulence field where particles preferentially accumulate. E. g. particles of intermediate response time accumulate in areas of low vorticity and high strain rate. Hsu and P. Liu (2004), Amoudry (2014) and Kranenburg et al. (2014) have incorporated effects of particles on fluid turbulence into their turbulence models for Reynolds-averaged Navier-Stokes equations (RANS).

Turbulent energy produced at the channel bed is reduced due to the presence of sediment when turbulent eddies move into the main flow zone. As a result the von Kárman constant used to describe the velocity profile in the logarithmic flow area is reduced (Einstein and Ning Chien, 1955). This has been shown in laboratory experiments by Einstein and Ning Chien (1955) and Nezu and Azuma (2004). Results of a four-way coupled Euler-Euler large-eddy simulation of sheet flow by Cheng et al. (2018b) also show a substantial reduction of the von Kárman constant. Ferreira (2015) pointed out influence of the mobility of the bed on the von Kárman constant by dimensional analysis and similarity.

Numerical models have good potential to provide additional benefit alongside physical laboratory studies and field measurements. They allow to observe processes at their process scale (Blöschl and Sivapalan, 1995). Spatially and temporally highly resolved data can be retrieved from numerical simulation results, which is not possible to observe in physical experiments. Thus errors from high integration volumes based on a finite number of samples (Blöschl and Sivapalan, 1995) can be avoided. Limitations of numerical models are necessary simplifications in the mathematical description of processes and averaging of unresolved processes.

## 1.5 Studies on suspended sediment transport

It is expected that dredging and dumping of sediment can become more effective through an optimized selection of the sites where the measure is carried out (IWHW, 2016). Paarlberg et al. (2015) show the usefulness of an investigation tool which allows to explore the feedback of different dredging and dumping strategies.

Using such a tool sediment management can potentially be optimized. In addition a prediction tool for the development of the sediment plume after dumping can help reduce environmental impact of the measure. The implementation of such a tool requires improved process understanding of sediment transport (Hauer et al., 2018; Haimann et al., 2018).

Validated numerical models can be used to study turbidity currents in reservoirs already in the design phase and confirm necessary information for the application of venting. Numerical simulation results are not subject to scaling errors which make physical scale experiments of sediment transport difficult (Hauer et al., 2018). Also for further development of sediment bypass tunnels computational fluid dynamics models might provide additional information (IWHW, 2016). Auel (2014) studied supercritical flow, sediment transport and resulting invert abrasion in sediment bypass tunnels in detail on physical models.

Experimental studies of suspended sediment transport with particular focus on particle-fluid velocity differences have been carried out by e. g. Greimann et al. (1999), Nezu and Azuma (2004) and Muste et al. (2005). Results of those experiments show a lag between particle and fluid velocities. In the outer flow region particle velocities are 4 % to 5 % lower than the fluid velocity, while in the near wall region ($y^+ < 15$) the velocity of the carrier fluid is exceeded by the particle velocity (Nezu and Azuma, 2004; Muste et al., 2005). Turbulence intensities are enhanced in the near-wall region but no turbulence modulation by particles can be observed in the outer region (Nezu and Azuma, 2004).

The main transport mechanism for suspended solids in reservoirs are turbidity currents (De Cesare et al., 2001; Chamoun et al., 2016). Hence hydrodynamic models of reservoirs should account for currents driven by density gradients. Density differences are caused by variations of water temperature, concentrations of a dilute substance and suspended sediment concentrations (Necker et al., 2002; IWHW, 2016).

Lock exchange experiments are a prominent test case for studying density currents physically (Huppert and Simpson, 1980; Bonnecaze et al., 1993; Gladstone et al., 1998; De Rooij and Dalziel, 2001; La Rocca et al., 2008; Musumeci et al., 2017; Stancanelli et al., 2018b) as well as numerically (Necker et al., 2002; Necker et al., 2005; Cantero et al., 2008a; Cantero et al., 2008b; La Rocca et al., 2008; Georgoulas et al., 2010; An et al., 2012; La Rocca et al., 2012; La Rocca et al., 2013; Musumeci et al., 2017; Stancanelli et al., 2018a). In these experiments one part of a container filled with fluid is initially separated by a lock. This confined part is filled with a higher density fluid (e. g. lower temperature, sediment suspension). After removing the lock a density current develops.

Laboratory studies of turbidity currents with particular focus on their development in reservoirs have been carried out by Fan (1960), Baas et al. (2004) and F.-Z. Lee et al. (2014) as well as Chamoun et al. (2017), Chamoun et al. (2018a) and Chamoun et al. (2018b). Baas et al. (2004) investigated the expansion of high-concentration (up to 35 %) turbidity currents on a horizontal plane. Chamoun et al. particularly studied the efficiency of venting of turbidity currents with respect to bed slope (Chamoun et al., 2017), venting degree (Chamoun et al., 2018b) and timing of venting (Chamoun et al., 2018a).

In contrast to lock exchange cases venting of turbidity currents has not yet been extensively investigated using numerical models. Density currents in reservoirs or lakes have been numerically studied by e. g. De Cesare et al. (2001), Lavelli et al. (2002), An and Julien (2014), Lai et al. (2015) and Huang et al. (2019). The model of turbidity currents in Tsengwen Reservoir (Taiwan) during a flood event set up by F.-Z. Lee et al. (2014) is the only numerical study found in literature which includes venting of a real reservoir. Hydrodynamics and sediment transport including bottom elevation changes due to erosion and deposition in the Iffezheim hydropower reservoir have been investigated numerically by Hillebrand et al. (2017). The model SSIIM (Sediment Simulation In Intakes with Multiblock option; NTNU, 2019) they used does not account for buoyant forces but only for the effect of density differences on turbulence (Olsen, 2018).

Most of the studies investigating sediment transport processes in rivers are based on steady flow situations. Time averaged parameters such as velocity and concentration profiles are discussed (e. g. Zhong et al., 2011; Zhong et al., 2014; Cheng et al., 2018b; Cheng et al., 2018a). The above summarized studies of density currents did include unsteady movement of a spatially confined sediment plume in turbulent fluid flow. In contrast to e. g. dumping situations there is usually no superimposed velocity of the surrounding fluid.

A study on the effect of model resolution of hydrodynamic models of rivers has been carried out by Glock et al. (2019). They analysed the influence of model dimensionality on results for water levels, flow velocities and bed shear stress.

Current challenges in sediment management need to be approached taking into account hydrodynamic and sediment transport processes on different scales (Hauer et al., 2018; IWHW, 2016). Computational fluid dynamics (CFD) is a useful method for the detailed study of flow fields. Hydrodynamic modelling offers new opportunities to plan measures in river engineering (IWHW, 2016; Tritthart, 2021). Large eddy simulations (LES) on small models are used to study the effect of fluctuating parameters in turbulent flows. The findings from those small scale, high fidelity models can then be used to optimize Reynolds averaged simulations (RANS) on larger scales (IWHW, 2016).

# 2 Aims and objectives

The overall idea of the research carried out in the course of this thesis is to study hydrodynamic processes related to sediment transport with respect to their process scale and required resolution for their accurate representation (IWHW, 2016). In the study in Section 4.1 of this thesis (Wildt et al., 2020) a strategic evaluation tool, which can be used for planning sediment management in reservoirs (De Cesare et al., 2001; IWHW, 2016), particularly venting of turbidity currents, is developed. Particle-driven gravity currents are implemented into the RSim-3D CFD solver (Tritthart, 2005; Tritthart and Gutknecht, 2007) by adding a source term to the momentum equation. Different implementations of the model were presented at the "International Jubilee Scientific Conference 70th anniversary FHE of the UACEG" in Sofia, Bulgaria (Wildt and Tritthart, 2019, Section 5.1). The final code is validated using experimental data from lock exchange experiments (Gladstone et al., 1998) and laboratory measurements of venting efficiency from Chamoun et al. (2018b).

The studies in Section 4.2 (Yücesan et al., 2021) and Section 4.3 (Wildt et al., 2022a) of this thesis investigate sediment transport mechanisms on fine scales. Large turbulence structures are resolved by LES models. The former study analyses the influence of very large-scale motion of coherent structures on the forces on a single sediment particle mounted to the channel bed with different exposure levels. Time series of forces are investigated by spectrum analysis. The results should enhance process understanding of incipient motion of sediment particles. Particular focus is put on different types of turbulent motion and their influence on particle entrainment.

The latter study investigates the development of a sediment plume as it is expected to occur after dumping of sediment into a river. A LES of turbulent channel flow is two-way coupled with a Lagrangian particle tracking model. The test case is designed to study the fully transient transport of particles by turbulent fluid flow. Sediment is released from a small, confined area in the flow field. Simulation results should reveal interaction processes between fluid and sediment at different times after the sediment entered the flow. This way process understanding of sediment transport in the initial phase after dumping should be enhanced.

Validation of the interaction between particles and fluid in still and turbulent channel flow has been presented at the "6th IAHR Europe Congress" (Wildt et al., 2021, Section 5.2). The variability of the shape and extents of the sediment plume based on arbitrary turbulent fluctuations in the initial velocity field is discussed at the "39th IAHR World Congress" (Wildt et al., 2022b, Section 5.3).

# 3 Methods

CFD models in the studies of this thesis are based on the incompressible Navier-Stokes equations.

$$\frac{\partial \phi}{\partial t} + \nabla \cdot (\boldsymbol{u}\phi) = \nabla \cdot (\Gamma \nabla \phi) + S_\phi \tag{1}$$

The equation describes the transient transport of a conservative property $\phi$ with time $t$ through a three-dimensional domain. It includes advection of $\phi$ by the velocity $\boldsymbol{u}$, diffusion by the diffusion coefficient $\Gamma$ as well as source and sink terms summarised by $S_\phi$ (Ferziger and Perić, 2002). Discretization of the differential equations is accomplished by the Finite Volume Method (FVM).

Turbulence is implemented with different degrees of resolution in the studies of this thesis. The model designed for large-scale studies of entire reservoirs in Section 4.1 (Wildt et al., 2020) uses the Reynolds-averaged Navier-Stokes equations (RANS) based on the standard $k$-$\epsilon$ turbulence model (Launder and Spalding, 1974; Tritthart, 2005). Large eddy simulations (LES) resolving large turbulence structures (Pope, 2000) are carried out in the smaller scale models, mainly aimed at improving process understanding (Yücesan et al., 2021 in Section 4.2 and Wildt et al., 2022a in Section 4.3). The Smagorinsky turbulence model (Smagorinsky, 1963) is used to model sub-grid scale turbulence in LES. The model constants $C_k = 0.02$ and $C_\epsilon = 1.05$ have been determined by Yücesan et al. (2022) in a parametric analysis and agree with literature (Lysenko et al., 2012).

Sediment transport is implemented through an advection-diffusion equation in the model in Section 4.1 (Wildt et al., 2020). The equation has the form of Equation (1) with the volumetric particle concentration $c$ as conservative property. The reduced gravitational acceleration $\boldsymbol{g}'$ is added to the source term of the fluid momentum equation in order to model buoyant forces $\boldsymbol{F}_b$ in the control volume $\Omega$ (Necker et al., 2002; An et al., 2012).

$$\boldsymbol{F}_b = \boldsymbol{g} \cdot \int_\Omega (\rho_s - \rho)\,\mathrm{d}V = \boldsymbol{g} \cdot c \cdot \int_\Omega (\rho_d - \rho)\,\mathrm{d}V \rightarrow \frac{\boldsymbol{F}_b}{\rho} = \boldsymbol{g} \cdot c \cdot \frac{\rho_d - \rho}{\rho} = \boldsymbol{g}' \tag{2}$$

$\boldsymbol{g}$ is the acceleration due to gravity. The density of the water-sediment suspension $\rho_s$ is calculated as the volumetric average of the fluid density $\rho$ and the particle density $\rho_d$ (dispersed phase).

Two-way momentum coupling is implemented in the LES model for the study of the development of the sediment plume in Section 4.3 (Wildt et al., 2022a). Particle movement is modelled based on the Lagrangian approach and coupled to fluid flow using the multiphase particle-in-cell (MP-PIC) method (Andrews and O'Rourke, 1996). The force balance of the interaction forces between particles and fluid is described by the Maxey-Riley equation (Maxey and Riley, 1983). The equation in Lagrangian coordinates is given by Prasath et al. (2019) in the following form:

$$R\dot{\boldsymbol{v}} = \frac{\mathrm{D}\boldsymbol{u}}{\mathrm{D}t} - \frac{1}{St}\left(\boldsymbol{v} - \boldsymbol{u}\right) - \sqrt{\frac{3}{\pi St}}\left(\frac{1}{\sqrt{t}}\left(\boldsymbol{v}\left(0\right) - \boldsymbol{u}\left(0\right)\right) + \int_0^t \frac{\dot{\boldsymbol{u}}\left(s\right) - \dot{\boldsymbol{u}}\left(s\right)}{\sqrt{t-s}}\,\mathrm{d}s\right) \quad (3)$$

$R$ is the effective density ratio which includes added-mass effects, $\boldsymbol{v}$ the particle velocity, $St$ the particle Stokes number and $t$ the current time. Lagrangian derivatives are marked by the dot $\dot{\square}$ symbol (Prasath et al., 2019).

The following forces are accounted for in the model in Section 4.3 (Wildt et al., 2022a):

- lift and drag forces,
- added mass forces,
- pressure force,
- gravity and
- inter-particle stresses.

Basset history forces in the last term of the Maxey-Riley equation (Equation 3) are neglected in the model. The forces are related to the development of the boundary layer around a particle during relative acceleration between particle and fluid (Joshi et al., 2019). Numerical implementation of the time integral involved in this term requires saving large amounts of data. The relative importance of this term in general needs to be further investigated (Cheng et al., 2018b). Prasath et al. (2019) showed the influence of the Basset history force in a number of test cases. For small Stokes numbers the influence of this term is generally expected to be low. Therefore it has also been neglected in similar studies by other authors (e. g. R. Sun et al., 2018; Cheng et al., 2018b; Cheng et al., 2018a).

The forces from particles on the fluid are added to the source term of the fluid momentum equation (Equation 1). Mass conservation is ensured in the MP-PIC method using a particle distribution function $f$ which is transported through the domain by the following equation (Andrews and O'Rourke, 1996; Snider, 2001):

$$\frac{\partial f}{\partial t} + \nabla_{\boldsymbol{x}} \cdot \left(f\boldsymbol{v}\right) + \nabla_{\boldsymbol{v}} \cdot \left(f\frac{\mathrm{d}\boldsymbol{v}}{\mathrm{d}t}\right) = \left(\frac{\partial f}{\partial t}\right)_{\mathrm{coll}} \quad (4)$$

Particle-particle interactions are taken into account through the source term $\left(\frac{\partial f}{\partial t}\right)_{\mathrm{coll}}$ on the right hand side of Equation (4).

Open-source software and in-house codes are used to solve the numerical models in this thesis. This enables full flexibility for the development of the models. In addition future use of the models will not be subject to licensing restrictions. The RANS model designed for large-scale studies of entire reservoirs in Section 4.1 (Wildt et al., 2020) is set-up and solved using RSim-3D (Tritthart, 2005; Tritthart and Gutknecht, 2007). The solver uses the unsteady semi-implicit method for pressure linked equations (SIMPLE) for pressure coupling. Small scale models resolving large turbulence structures (LES), mainly aimed to improve process understanding, in Sections 4.2 and 4.3 (Yücesan et al., 2021; Wildt et al., 2022a) are solved using the open-source package OpenFOAM 6 (Greenshields, 2018). Pressure coupling in these models is accomplished using the pressure implicit split operator (PISO) algorithm.

# Part II

# Publications

# 4 Publications in SCI-listed journals

## 4.1 Water (2020): "CFD Modelling of Particle-Driven Gravity Currents in Reservoirs"

| | |
|---|---|
| Journal: | Water<br>This article belongs to the Special Issue "Advanced Modelling Strategies for Hydraulic Engineering and River Research" |
| Volume: | 12 |
| Number: | 5 |
| Article number: | 1403 |
| DOI: | `https://doi.org/10.3390/w12051403` |
| Authors: | Daniel Wildt, Christoph Hauer, Helmut Habersack and Michael Tritthart |
| Submitted: | 20th April 2020 |
| Accepted: | 10th May 2020 |
| Published: | 15th May 2020 |

Article available open access: `https://www.mdpi.com/2073-4441/12/5/1403`

Highlights:

- Density currents are implemented into the RSim-3D solver via a source term in the momentum equation.
- The buoyancy implementation is validated using literature data of lock exchange experiments.
- The solvers ability to model venting of turbidity currents in a reservoir is tested using test cases from literature.

water

MDPI

Article

# CFD Modelling of Particle-Driven Gravity Currents in Reservoirs

**Daniel Wildt** [1,2,*], **Christoph Hauer** [1,2], **Helmut Habersack** [2] **and Michael Tritthart** [1,2]

[1] Christian Doppler Laboratory for Sediment Research and Management, University of Natural Resources and Life Sciences Vienna, Muthgasse 107, 1190 Vienna, Austria; christoph.hauer@boku.ac.at (C.H.); michael.tritthart@boku.ac.at (M.T.)

[2] Institute of Hydraulic Engineering and River Research, Department of Water–Atmosphere–Environment, University of Natural Resources and Life Sciences Vienna, Muthgasse 107, 1190 Vienna, Austria; helmut.habersack@boku.ac.at

* Correspondence: daniel.wildt@boku.ac.at; Tel.: +43-1-47654-81935

Received: 20 April 2020; Accepted: 10 May 2020; Published: 15 May 2020

check for updates

**Abstract:** Reservoir sedimentation results in ongoing loss of storage capacity all around the world. Thus, effective sediment management in reservoirs is becoming an increasingly important task requiring detailed process understanding. Computational fluid dynamics modelling can provide an efficient means to study relevant processes. An existing in-house hydrodynamic code has been extended to model particle-driven gravity currents. This has been realised through a buoyancy term which was added as a source term to the momentum equation. The model was successfully verified and validated using literature data of lock exchange experiments. In addition, the capability of the model to optimize venting of turbidity currents as an efficient sediment management strategy for reservoirs was tested. The results show that the concentration field during venting agrees well with observations from laboratory experiments documented in literature. The relevance of particle-driven gravity currents for the flow field in reservoirs is shown by comparing results of simulations with and without buoyant forces included into the model. The accuracy of the model in the area of the bottom outlet can possibly be improved through the implementation of a non-upwind scheme for the advection of velocity.

**Keywords:** turbidity currents; sediment; reservoir; venting; computational fluid dynamics

## 1. Introduction

Reservoir sedimentation is an increasingly important challenge that operators worldwide are facing [1–4]. Storage capacity lost results in a decrease of energy production [5]. Moreover the interruption of sediment continuity impacts the downstream river morphology causing ecological problems. Thus efficient sediment management is important for economical, technical and environmental reasons [1,6].

Turbidity currents are the main transport mechanisms for fine sediments in reservoirs. They can even redistribute the material inside the reservoir [7]. In literature turbidity currents are also referred to as particle-driven gravity currents. They represent a group of density currents in which density differences result from the spatial distribution of concentration of a particulate substance. In contrast to other density currents where density differences are caused by e.g., concentration variations of a diluted substance or by temperature variations there occurs a relative velocity between the dispersed phase and the ambient phase [8]. This relative velocity is a result of gravitational (settling) and inertia forces [9].

Field observations of turbidity currents are difficult to accomplish due to their rare occurrence, for example during floods [9,10]. In addition turbidity currents usually form on the bottom of large and deep reservoirs [7] which are difficult to reach. Thus the analysis of such currents in real reservoirs is often limited to time series of point measurements of flow properties at different locations. Some studies focus on the analysis of the consequences of turbidity currents such as bottom elevation changes [7,11]. The use of satellite imaginary for turbidity measurements over larger areas (e.g., [12]) is not considered applicable for the study of turbidity currents, because this method provides turbidity data only for the near surface region of the reservoir. In addition, in most cases the spatial resolution of the available images will not be high enough.

Physical laboratory experiments have been undertaken to enhance process understanding of density currents in general (e.g., [13–16]) and also particle-driven gravity currents in particular (e.g., [17–23]). Lock exchange experiments are a common approach of studying gravity currents. They feature a certain volume of sediment laden fluid which is released into still ambient fluid by removing a lock which is initially separating two compartments [13,15,16,18–20]. The main parameter studied in these experiments is the flow front advance of the gravity current with time. In addition, the current height and sediment deposition are often recorded.

Huppert and Simpson [13] discuss several theoretical concepts describing gravity currents and study their efficiency in the laboratory on lock exchange experiments. They categorize the temporal development of the turbidity current into three regimes: (i) Right after the release of the suspension the gravity current passes through the slumping phase, in which the buoyant force is in balance with the counterflow of the ambient fluid; (ii) After this initial phase, in which the velocity is fairly constant, the gravity current is in the inertia-buoyancy phase in which it is balanced by forces of inertia; (iii) The final stage of a gravity current is the viscous-buoyancy regime where it is balanced by viscous forces [13].

Experiments with constant inflow and sediment supply have been carried out (amongst others) by Baas et al. [21] and Sequeiros et al. [22,23]. The former studied the expansion of high-concentration turbidity currents on a horizontal plate and the following deposition of sediments on that plate [21]. The latter carried out experiments with constant inflow and sediment supply studying self acceleration of turbidity currents due to sediment uptake [22].

Venting of turbidity currents has the potential of enabling highly efficient sediment management in reservoirs, satisfying economical as well as ecological needs [3,10,17,24]. The aim of this sediment management strategy is to route turbid water through bottom outlets as soon as it reaches the dam [3]. Water losses through venting are generally lower than the amount of water lost by flushing. In addition, sediment continuity can be maintained to a high degree [3,24]. As for any sediment management strategy for reservoirs, a detailed process understanding of the driving sediment transport processes is particularly crucial for efficient venting of turbidity currents [1,24].

Laboratory studies investigating particularly the formation and evolution of turbidity currents in a reservoir during venting have been performed by Fan and Chamoun et al., The former gathered general knowledge on turbidity currents and their development during venting [17]. The latter elaborated optimum conditions for venting in terms of bed slope of the reservoir [25], venting degree [24] and timing of venting [26]. With the advance of computational fluid dynamics (CFD), the experimental set-up of lock exchange experiments has been taken up for numerical studies [8,9,14,27–31]. Flow in these models is purely driven by gradients in the spatial distribution of density. Thus they provide an efficient test case for the validation of solvers for models of density currents. In models particularly for the simulation of fluid flow in reservoirs the set-up of lock exchange experiments imitates the inflow of turbid water during a short term storm event.

Sediment transport in these models is implemented in different detail. One-way coupling of momentum exchange between the ambient and the dispersed phase can be achieved using advection-diffusion equations [8,29,32]. In these models the particle velocity equals the sum of the fluid velocity and the fall velocity. Hence forces of inertia are neglected [8,29]. In addition, the dispersed phase is neglected in the mass conservation equation. Buoyant forces are accounted for through a source term in the momentum equation and neglected for all other terms rather than gravitational terms (Boussinesq approximation) [8,29,33]. This limits the applicability of such models to small mass loadings [8,29].

An et al. [29] simulated different kinds of gravity currents including particle driven gravity currents produced by lock exchange experiments from Gladstone et al. [19]. The focus of this study was on the differences in large eddy simulations and Reynolds averaged simulations of gravity currents. Similarly, Stancanelli et al. [30] studied the differences of LES and RANS numerically but using the setup of Musumeci et al. [15] and Stancanelli et al. [16], where the high density fluid was released into an oscillating ambient fluid [30]. Both models ([29,30]) were solved using the commercial FLOW-3D CFD code.

On the basis of their results An et al. [29] classify particle-driven gravity currents into three regimes with respect to the deposition rate of the sediment. When particles are small (e.g., $d < 16\,\mu m$) and hence fall velocity is low deposition has only little influence on the propagation of the gravity current (suspended regime). When suspended particles are larger (e.g., $16\,\mu m < d < 40\,\mu m$), the propagation of the gravity current is highly influenced by the fall velocity (mixed regime). Particle-driven gravity currents with larger particles (e.g., $d > 40\,\mu m$) rapidly loose momentum due to deposition (deposition regime). Exemplary particle sizes mentioned above apply to particles with a relative density of $\rho_{\text{rel}} = 3.22$. [29].

Necker et al. [8] studied the development of a particle-driven gravity current in several further aspects. The numerical data is compared to experimental data of DeRooij and Dalziel [20]. Additional data is retrieved from a high resolution numerical model as well as laboratory experiments carried out by Bonnecaze et al. [18]. Main points studied by Necker et al. were (i) the structure of the flow front, (ii) conversion of potential energy to kinematic energy and (iii) dissipation of energy due to particle settling. In addition the difference between 2D and 3D models of turbidity currents is discussed. Resuspension of particles is considered to the point that the authors show using Shields critical velocities [34] that resuspension is unlikely to occur in the studied flows [8].

Two-way coupling is necessary for higher mass loads and to account for inertial effects [9,31,35]. A model treating water and sediment as separate continua has been set up using the commercial code FLUENT by Georgoulas et al. [9]. With this model they reproduced the lock exchange experiments of Gladstone et al. [19] and simulated the expansion of high concentration turbidity currents on a horizontal plane as physically investigated by Baas et al. [21]. Cantero et al. [31,35] accounted for inertial effects using an Eulerian equilibrium approach. They carried out a direct numerical simulation of turbidity currents on a 2D Eulerian-Eulerian model.

A simplified approach for modelling the two-phase flow of a water-sediment suspension including buoyant forces has been proposed by LaRocca et al. [14,27] using the two-layer shallow water equations. Their approach is based on the assumption that the upper layer of lighter fluid remains flat during the motion. In addition to the commercial codes mentioned above, also the freeware Delft3D-FLOW model [33] developed by Deltares provides the capability of modelling particle-driven gravity currents for river applications.

Despite this large number of studies on investigating the basic process of the formation and development of turbidity currents in test cases physically and numerically, only a reduced number of works on turbidity currents in operational reservoirs has been found in literature. Exemplary, simulations of turbidity currents in reservoirs during flood events have been carried out for the Luzzone Lake, Switzerland [7], the Lugano Lake, Switzerland/Italy [36] and the Imha Reservoir, South Korea [32]. The former two models were solved using the CFX-4 code, while the latter was solved with the FLOW-3D model presented in an earlier study by the same authors [29].

Hillebrand et al. [37] simulated the flow field and sediment transport including bottom elevation changes in the Iffezheim hydropower reservoir. They used the freeware SSIIM developed at the Norwegian University of Science and Technology (NTNU) [38] for their model. This code accounts for the effects of density changes on turbulence but not for buoyant forces [39].

A two-dimensional simulation of turbidity currents in the Shimen Reservoir, Taiwan, has been carried out by Huang et al. [10], using the 2D layer-averaged turbidity current model SRH2D [40]. The method used to model turbidity currents in this model is similar to what has been proposed by LaRocca et al. [14,27]. For the study of venting Huang et al. applied a two stage approach using the empirical Rouse equation [41] for the estimation of the sediment released through the outlets at the dam.

The model set up by Leeet al. [11] simulating turbidity currents in Tsengwen Reservoir in Taiwan during typhoon-induced food events is the only model found in literature in which venting is included. The model based on the CFX-12.0 code was validated against a laboratory experiment with a setup similar to the experiments carried out by Chamoun et al. [24–26]. Additionally, the model of the real reservoir was validated using concentration measurements at different elevations near the dam. Based on their results, Lee et al., developed a formula for the estimation of the concentration of the vented suspension [11].

Apart from the study by Lee et al. [11] no other 3D model applications particularly studying venting of turbidity currents have been found in literature. On the one hand, such a numerical tool can provide the basis for the design of an efficient venting system for reservoirs Lee et al., Numerical models are more flexible for geometry adaptions than physical models. They are free of scaling errors and allow an analysis of the entire flow field in high detail. They can be used to study the development of a turbidity current at the actual site of a reservoir which is usually difficult to rebuild in every detail in a laboratory. On the other hand, Lee et al. pointed out that the required fine discretization and thus long computation times make it impractical to run such a model on a normal desktop computer in real time [11].

Hence this study aims to develop a numerical model allowing to study turbidity currents in real reservoirs. The basic hydrodynamic model used is RSim-3D [42–44]. This model is adopted for the simulation of turbidity currents through a source term in the momentum equations. Basic model verification and validation is carried out reproducing the lock exchange experiments by Gladstone et al. [19]. Moreover, results of the experiments by Chamoun et al. [24–26] were used for further optimization of the tool to study the development of turbidity currents in reservoirs. Thus, in a second step, these experiments are reproduced with the developed model.

## 2. Materials and Methods

### *2.1. Governing Equations and Model Setup*

#### 2.1.1. Hydrodynamic Model

RSim-3D is a computational fluid dynamics code solving the incompressible three-dimensional Navier-Stokes equations on a polyhedral mesh [42,45]. The equations are Reynolds averaged optionally using the standard $k$-$\epsilon$ [42] or the $k$-$\omega$ [46] turbulence model.

$$\frac{\partial \phi}{\partial t} + \nabla \cdot (\boldsymbol{u}\phi) = \nabla \cdot (\Gamma \nabla \phi) + S_\phi \tag{1}$$

$\phi$ in Equation (1) represents the conservative property which is transported through the domain. It is replaced with the velocity $\boldsymbol{u}$ for the momentum equation in the respective direction or 1 for the continuity equation. Similarly the diffusion coefficient $\Gamma$ is dependent on the particular conservative property. For the momentum equations, the diffusion coefficient is calculated as $\Gamma = \rho \cdot (\nu + \nu_t)$ where $\nu$ represents the dynamic viscosity of the fluid and $\nu_t$ the turbulent viscosity. The turbulent viscosity is estimated based on the standard $k$-$\epsilon$ turbulence model [47]. $\rho$ is the fluid density. Sources and sinks are added in the source term $S_\phi$. For the momentum equations the source term includes the pressure gradient $\frac{1}{\rho} \cdot \nabla p$. For the mass conservation equations $S_\phi$ is generally 0 with the exception of Dirichlet boundaries [42].

#### 2.1.2. Sediment Transport Model

Suspended sediment transport is modelled using an advection-diffusion equation which is of the same generic form as the Navier-Stokes Equation (1). This approach has already been used for similar models in literature (e.g., [29,38]). The conservative property $\phi$ is the volumetric sediment concentration $c$. Sediment diffusivity is calculated as the quotient of turbulent viscosity and the Schmidt number.

Sediment settling is implemented through the source term $S_c$ by adding the term $\boldsymbol{v}_s \cdot \nabla c$, where $\boldsymbol{v}_s$ is the fall velocity of the particles. A set of different equations for the estimation of the fall velocity of particles with a diameter $d_s$ has been added to the code. The implemented approaches include the formula by Atkinson et al. in which the fall velocity in $\mathrm{m\,s^{-1}}$ equals the particle diameter in m to the power of 1.3 [48]. In addition Stokes fall velocity [49] has been added to the code in a three-dimensional form. The equation is piecewise continuous and has discontinuities at $d_s = 100\,\mu\mathrm{m}$ and $d_s = 1000\,\mu\mathrm{m}$.

$$\boldsymbol{v}_s = \begin{cases} \frac{1}{18\nu} \cdot \boldsymbol{g} \cdot \frac{\rho_d - \rho_s}{\rho_s} \cdot d_s^2 & d_s < 100\,\mu\mathrm{m} \\ 10\frac{\nu}{d_s}\left(\left(\frac{\boldsymbol{g}}{|\boldsymbol{g}|} + \boldsymbol{g} \cdot \frac{0.01\cdot(\rho_d - \rho_s)}{\rho_s \cdot \nu^2} \cdot d_S^3\right)^{\frac{1}{2}} - \frac{\boldsymbol{g}}{|\boldsymbol{g}|}\right) & 100\,\mu\mathrm{m} < d_s < 1000\,\mu\mathrm{m} \\ 1.1 \cdot \left(\boldsymbol{g} \cdot \frac{\rho_d - \rho_s}{\rho_s} \cdot d_s\right)^{\frac{1}{2}} & d_s > 1000\,\mu\mathrm{m} \end{cases} \tag{2}$$

$\boldsymbol{g}$ is the acceleration due to gravity, $\rho_d$ particle density (dispersed phase) and $\rho_s$ the density of the particle fluid suspension. The latter is calculated as the volume average of the fluid density $\rho$ and the particle density $\rho_d$ [19,24].

$$\rho_s = c \cdot \rho_d + (1 - c) \cdot \rho \tag{3}$$

Tritthart et al. [50] analysed different approaches [48,49,51] for estimating settling velocity. They found that their results differ up to three orders of magnitude. In consequence the selection of the approach for estimating fall velocity should be the outcome of a calibration process. For the experiments reproduced in the validation of the code in this study best results have been achieved using the Stokes fall velocity [49] in Equation (2).

When sediment particles reach the bottom cell, they can settle "through" the bottom boundary and this way leave the domain. In preliminary tests this approach has proven to be most efficient for the cases studied in this article. Other approaches like applying a reference sediment concentration [49] based on bottom shear stress [34] or accumulating sediment in the bottom cell are mesh dependent. For later analysis of the amount of sediment deposited, the volume of sediment that has settled through the bottom cell is recorded.

Resuspension of sediment is not included in the implementation of bottom exchange used in this study. However it is not expected that the process plays an important role in the investigated cases as the laboratory channels did not have a loose bed [19,24]. Particles accumulating on the bottom through settling are neglected. In addition flow velocities are generally low in the test cases in this study [8]. Nevertheless resuspension might become relevant when applying the model to real reservoirs with loose beds [22,23].

#### 2.1.3. Buoyant Forces

The difference of $\rho_s$ Equation (3) between regions with different suspended sediment concentration $c$ induces a buoyant force that drives the turbidity current. The buoyant force $\boldsymbol{F}_b$ acting on a suspension volume $\Omega$ can be calculated using the archimedian principle in the following way [14,29]:

$$\boldsymbol{F}_b = \boldsymbol{g} \cdot \int_\Omega (\rho_s - \rho)\,\mathrm{d}V = \boldsymbol{g} \cdot c \cdot \int_\Omega (\rho_d - \rho)\,\mathrm{d}V \rightarrow \frac{\boldsymbol{F}_b}{\rho} = \boldsymbol{g} \cdot c \cdot \frac{\rho_d - \rho}{\rho} = \boldsymbol{g}' \tag{4}$$

The reduced gravity $g'$ defined in Equation (4) is added as a source term to the momentum equation. According to the Boussinesq approximation, density variations are neglected for terms other than the gravitational ones [8,29,33].

2.1.4. Discretization

The Navier-Stokes Equation (1) including the advection-diffusion equation as well as the source terms described above are discretized on a polyhydral mesh applying the finite volume method. The dominant cell shape of the horizontal descretization is hexahedral, while the vertical mesh is structured [42,43]. A plan view on a mesh for the numerical solution of the experiments from Gladstone et al. [19] is displayed in Figure 1.

Pressure coupling is accomplished by the SIMPLE algorithm (Semi-Implicit Method for Pressure-Linked Equations) [42,45] which is iterated until convergence (all residuals $\epsilon \leq 10^{-3}$) at each time step. For unsteadiness fully implicit time discretization is applied.

*2.2. Code Validation and Mesh Sensitivity Analysis*

Code validation was carried out with particular focus on its capability of modelling turbidity currents. This capability has been here newly implemented into the RSim-3D code. The hydrodynamic model of RSim-3D has already been validated in various test cases (e.g., [42,43,52]) as well as real river applications (e.g., [52,53]). In addition the suspended sediment transport model has been used for several earlier studies (e.g., [44,54–57])

The code was validated against results of a set of lock exchange experiments published by Gladstone et al. [19]. The experiments feature a 5.7 m long and 0.2 m wide channel with horizontal bed and constant water level of 0.4 m. On one end of the channel a 0.2 m long section is initially separated by a lock and filled with water-sediment suspension instead of clear water (see Figure 1). The volumetric concentration of the suspension amounts to 3490 ppm. Amongst other data, time series of flow front advance distances after removal of the lock are provided for several different experimental runs. The experiments differ in the grain size of the sediment. The density of the sediment used by Gladstone et al. was 3217 kg m$^{-3}$ [19]. Sediment density, volumetric sediment concentration and channel width as characteristic length scale correspond to a Grashof number of about $1.9 \times 10^8$.

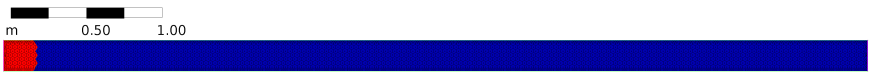


**Figure 1.** Plan view on the initial situation of the lock exchange experiments carried out by Gladstone et al. [19] on a hexahedral mesh with 3 cm cell diameter; red: $c = 3490$ ppm, blue: $c = 0$ ppm.

The following four experiments carried out by Gladstone et al. [19] have been reproduced numerically using the RSim-3D code with the newly implemented source term accounting for buoyant forces:

- Case A: one grain fraction with $d_s = 25\,\mu$m and $v_s = 0.8$ mm s$^{-1}$.
- Case D: two grain fractions to equal amounts with $d_{s1} = 25\,\mu$m and $d_{s2} = 69\,\mu$m and $v_{s1} = 0.8$ mm s$^{-1}$ and $v_{s2} = 5.8$ mm s$^{-1}$, respectively.
- Case G: one grain fraction with $d_s = 69\,\mu$m and $v_s = 5.8$ mm s$^{-1}$.
- Case R: five grain fractions to equal amounts with $d_{s1} = 17\,\mu$m, $d_{s2} = 37\,\mu$m, $d_{s3} = 63\,\mu$m, $d_{s4} = 88\,\mu$m and $d_{s5} = 105\,\mu$m and $v_{s1} = 0.3$ mm s$^{-1}$, $v_{s2} = 1.7$ mm s$^{-1}$, $v_{s3} = 4.8$ mm s$^{-1}$, $v_{s3} = 9.4$ mm s$^{-1}$ and $v_{s5} = 11.3$ mm s$^{-1}$, respectively.

Flow front advance in the lock exchange experiments was monitored by Gladstone et al., by measuring the distance between the flow front and the gate in regular intervals of 3 s [19]. In the numerical model the position of the flow front is defined at the cell centre of the cell furthest from the gate in the second layer above the bottom which has a sediment concentration higher than 10 ppm (see Figure 2).

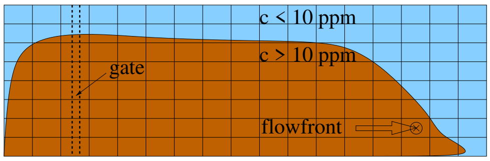


**Figure 2.** Scheme visualising the definition of the flow front position in the numerical model results.

To study the discretization error and test mesh convergence the model was run on four different meshes using five different time steps. Table 1 displays the cell sizes and time steps with approximate maximum Courant numbers which were used in the numerical model of the lock exchange experiments [19].

**Table 1.** Meshes, time step and approximate maximum Courant number for the mesh sensitivity analysis.

| $\Delta t$ | Meshes | 5v110 | 3v120 | 3v130 | 2v140 |
|---|---|---|---|---|---|
| | horizontal spacing in cm | 5 | 3 | 3 | 2 |
| s | number of vertical layers | 10 | 20 | 30 | 40 |
| | total number of cells | 7280 | 42 160 | 63 240 | 172 200 |
| 1.00 | | 2.2 | 4.7 | 7.2 | – |
| 0.50 | | 1.2 | 2.5 | 3.9 | – |
| 0.20 | max. Courant number | 0.5 | 1.1 | 1.7 | 2.2 |
| 0.10 | | 0.3 | 0.5 | 0.8 | 1.1 |
| 0.05 | | 0.1 | 0.3 | 0.4 | 0.6 |

The following boundary conditions were applied in the model: no-slip boundary condition for the bottom and side walls, a symmetry boundary condition for the free surface and a zero gradient velocity boundary condition with fixed pressure at the outlet. Although there was no inflow velocity in the physical experiments [19], an inflow velocity of $1.25 \times 10^{-5}$ m s$^{-1}$ (0.001 L s$^{-1}$) was applied at the inlet for stability reasons.

### *2.3. Test Case for the Study of Turbidity Current Venting Efficiency*

The applicability of the RSim-3D-solver for the optimization of venting of turbidity currents in reservoirs was studied by reproducing the experimental set-up of Chamoun et al. [24]. In these experiments 0.001 m$^3$ s$^{-1}$ of a sediment suspension with a volumetric concentration of 2.3% ($\hat{=}$27 g L$^{-1}$) was constantly fed into a laboratory channel. The channel representing a reservoir is initially filled with clear water so that the water depth amounts to 0.8 m. The dimensions of the channel are 6.7 m in length and 0.27 m in width. A bottom outlet 0.12 m high and 0.09 m wide is placed at the end of the channel through which water is vented at a specific flow rate [24–26].

Sediment properties used in the venting experiments are: $d_{10}$ = 66.5 µm, $d_{50}$ = 140 µm, $d_{90}$ = 214 µm with a density of $\rho_d$ = 1160 kg m$^{-3}$ [24–26]. Concentration, density and channel width correspond to a Grashof number of $4.1 \times 10^8$. This is of the same order of magnitude as the Grashof number in the lock exchange experiments [19] (see above). For the numerical model eight fractions of sediment size listed in Table 2 were used.

**Table 2.** Characteristic grain size distribution used for the numerical model of the venting experiments [24].

| Grain Size in µm | 67 | 80 | 90 | 110 | 140 | 150 | 160 | 214 |
|---|---|---|---|---|---|---|---|---|
| Stokes fall velocity Equation (2) in mm s$^{-1}$ | 0.4 | 0.6 | 0.7 | 0.9 | 1.5 | 1.7 | 2.0 | 3.5 |
| volumetric fraction at inflow in ppm | 2328 | 2328 | 2328 | 4655 | 4655 | 2328 | 2328 | 2328 |
| share of total sediment in % | 10 | 10 | 10 | 20 | 20 | 10 | 10 | 10 |

In their experiments Chamoun et al., tested the influence of the ratio of vented flow rate to the inflowing discharge (venting degree $\phi_{\mathrm{VENT}}$) on venting efficiency. For this purpose the vented sediment concentration was continuously recorded. In addition sediment deposition was measured at multiple locations along the channel [24].

From the concentration and the density $\rho_s$ of the vented suspension and the vented flow rate $Q_{\mathrm{VENT}}$ the aspiration height $h_L$ according to Fan [17] is calculated [24].

$$\left(\frac{\rho_s-\rho}{\rho}\cdot\frac{g\cdot(-h_L)^5}{Q_{\mathrm{VENT}}^2}\right)^{\frac{1}{5}} = -1.2 \Rightarrow h_L = \sqrt[5]{(-1.2)^5\cdot\frac{\rho\cdot Q_{\mathrm{VENT}}^2}{(\rho_s-\rho)\cdot g}} \tag{5}$$

When the height of the turbidity current at the dam is higher than this theoretical value, only turbid water is vented [10,17,24].

Venting efficiency was analysed with respect to global venting efficiency (GVE). Global venting efficiency is defined for a time step $t$ as the ratio of the total sediment mass that has entered the reservoir to the vented mass of sediment until $t$ [24].

$$GVE(t) = \frac{\int_0^t c_{\mathrm{in}}\cdot Q_{\mathrm{in}}}{\int_0^t c_{\mathrm{vent}}\cdot Q_{\mathrm{vent}}} \tag{6}$$

Venting time is normalized for the sake of results comparison on the basis of the aspiration height $h_L$ in Equation (5) [24].

$$\bar{t} = g'\cdot\frac{t-T_{\mathrm{vi}}}{h_L} \tag{7}$$

$T_{\mathrm{vi}}$ in Equation (7) is the time when venting starts ($T_{\mathrm{vi}} = 150$ s in all cases).

For the numerical model of venting the same types of boundary conditions were used, that were also applied in the lock exchange cases (see above). The flow rate at the inlet is set to 0.001 m$^3$ s$^{-1}$. The outlet situation including the bottom outlet for venting have been modelled in the following way: A quadratic channel with 4.4 cm edge length was attached to the end wall of the flume. This represents the venting pipe with a diameter of 5.0 cm which has the same cross sectional area. The edges between the end wall of the flume and the venting channel were rounded so that a 9 cm wide section is left open in the end wall.

Cells at the entrance to the venting channel that have cell centres higher than 12 cm above the bottom were assigned with a no-slip wall boundary condition to limit the height of the bottom outlet opening. Further downstream in the venting channel cells with cell centres less than 5 cm above the bottom are assigned with the wall boundary condition to limit the height of the venting pipe. In cases with a venting degree of $\phi_{\mathrm{VENT}} < 100\%$ the two uppermost cell layers are left open to enable overflow over the "weir". Venting degrees of $\phi_{\mathrm{VENT}} < 100\%$ are implemented into the numerical model by assigning a fixed velocity to the "open" cells below the internal wall. The velocity in the bottom boundary cells is interpolated using a wall function [42]. Higher venting degrees of $\phi_{VENT} \geq 100\%$ are implemented through the pressure boundary condition at the outlet. The water level there is lowered with respect to the volume decrease in the channel.

After the "inlet" into the venting pipe only four cell layers in the upper third of the channel are assigned the no-slip wall boundary condition. This way the height of the venting channel is increased again to enable a stable zero-gradient outlet boundary condition.

The domain is discretized using dominantly hexahedral cells in horizontal direction and a structured mesh in vertical direction. The area of the venting pipe is meshed using dominantly quadrilateral cells. The hexahedral cells have a diameter of about 3 cm. In vertical direction 40 cell layers are used. This cell size has been found most practical in a mesh sensitivity analysis carried out by Lee et al. [11] using a similar experimental setup. Results of the mesh sensitivity analysis using the lock exchange experiments [19] in Section 4.2 show that this discretization is reasonable for the RSim3D-code as well. In total the mesh has 118,800 cells. A time step of 0.1 s is used for time discretization.

## 3. Results

### 3.1. Flow Front Advance in Lock Exchange Experiments

Figure 3 displays the development of the turbidity current in the lock exchange experiments after removal of the lock. The images show the water sediment suspension plunging below the clear water and then travelling along the bottom of the channel.

Initially the turbidity current has a triangular shape with the surface slanted towards the front of the current (Figure 3a). After the acceleration of the current, the shape of the current becomes rectangular. Its height decreases only slightly with time (Figure 3b–d).

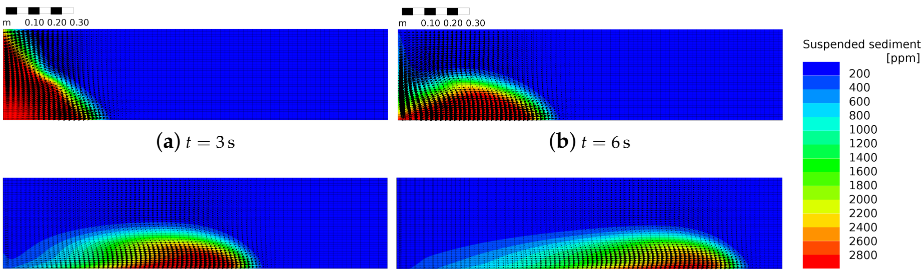


(**a**) $t = 3\,\mathrm{s}$ (**b**) $t = 6\,\mathrm{s}$

(**c**) $t = 12\,\mathrm{s}$ (**d**) $t = 18\,\mathrm{s}$

**Figure 3.** Formation of the turbidity current after release of the sediment suspension into clear water in the lock-exchange experiment (case A, longitudinal section [19]); flow direction from left to right, concentration contours in ppm.

The results of the flow front advance in the numerical model are plotted against literature results [19] in Figure 4. The plots show the increasing distance between the flow front and the lock position with ongoing time after the lock removal. The initial velocity of the turbidity currents with different sediment particle size is similar in all cases. Flow front advance is decaying with time depending on the fall velocities of the particles in the respective case. In cases with small particle sizes and thus low fall velocity (e.g., case A in Figure 4a) the velocity of the turbidity current decreases only slightly. In contrast, a sharp bend is visible in the flow front advance of case G where particles are larger and thus settle faster (e.g., case G in Figure 4c).

The flow front advance in Figure 4 from the numerical simulations on coarser meshes is generally underestimated. With refinement of the mesh the results of the numerical model approach the results of the physical model. Hardly any difference is visible in results of the flow front advance from the simulations on the second finest and the finest mesh.

*Water* **2020**, *12*, 1403 

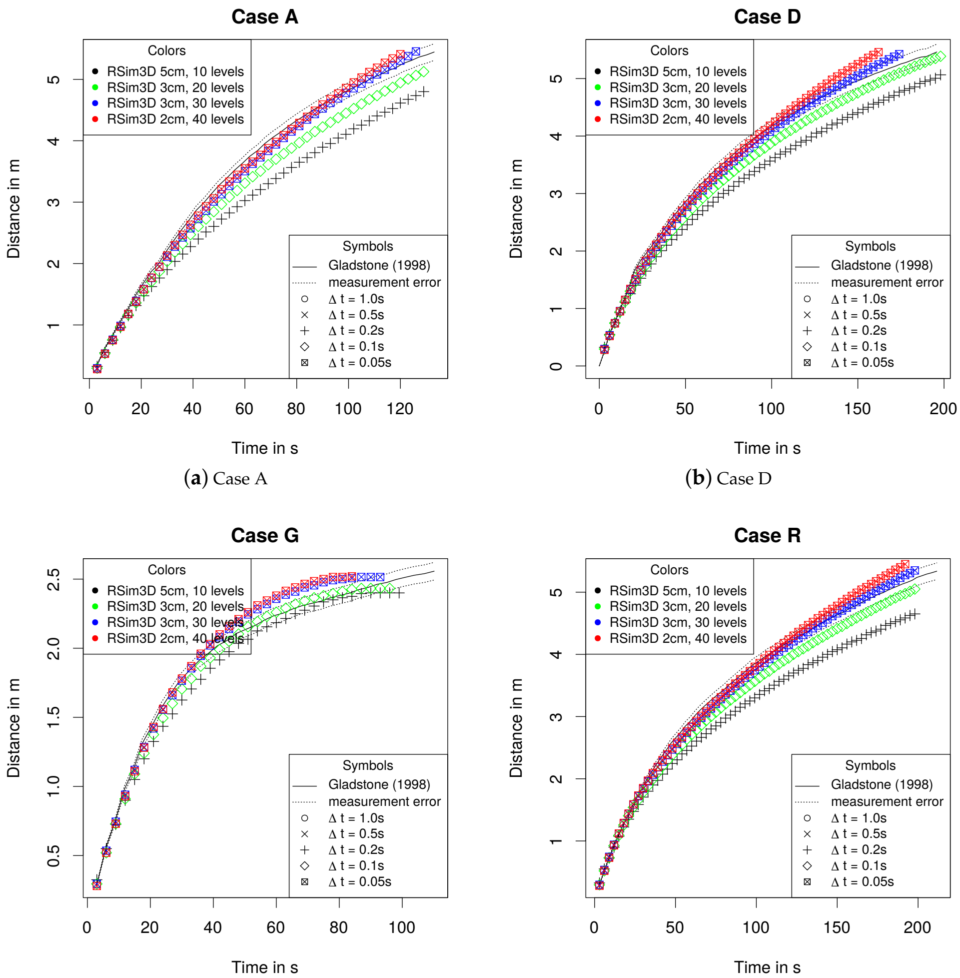


(**a**) Case A (**b**) Case D (**c**) Case G (**d**) Case R

**Figure 4.** Flow front advance; the time steps correspond to a Courant number of approximately 0.5: (**a**) Case A $d = 25\,\mu m$. (**b**) Case D $d_1 = 25\,\mu m$, $d_2 = 69\,\mu m$. (**c**) Case G $d = 69\,\mu m$. (**d**) Case R $d_1 = 17\,\mu m$, $d_2 = 37\,\mu m$, $d_3 = 63\,\mu m$, $d_4 = 88\,\mu m$, $d_5 = 105\,\mu m$. In cases including more than one grain size the total sediment concentration is uniformly distributed across all fractions.

*3.2. Computational Effort of the Numerical Models of the Lock Exchange Experiments*

Table 3 displays the computation time required for Case D of the lock exchange experiments on different meshes and with different time steps. The simulations were run in parallel on an Intel i7-3770 (16 GB RAM) processor using four cores. Parallelization was realised using OpenMP.

*Water* **2020**, *12*, 1403 

**Table 3.** Computation time for Case D of the lock exchange experiment on different meshes and with different time steps.

| $\Delta t$ | Meshes | 5v110 | 3v120 | 3v130 | 2v140 |
|---|---|---|---|---|---|
| s | horizontal spacing in cm | 5 | 3 | 3 | 2 |
| | number of vertical layers | 10 | 20 | 30 | 40 |
| | total number of cells | 7280 | 42 160 | 63 240 | 172 200 |
| 1.00 | Computation time in h | 0.5 | 12.8 | 17.0 | – |
| 0.50 | | 0.6 | 10.8 | 17.7 | – |
| 0.20 | | 0.7 | 11.5 | 17.0 | 57.0 |
| 0.10 | | 0.7 | 12.1 | 17.5 | 60.7 |
| 0.05 | | 0.8 | 13.4 | 18.0 | 67.0 |

The computation times in Table 3 show that the computational effort mainly increases with mesh refinement. Although the reduction of the time step requires the equations to be solved at additional time steps, computation time increases by a far lower factor than the number of time steps is increased. For some cases computation time could even be reduced by decreasing the time step.

### *3.3. Venting*

Figure 5 displays sediment contours at time $t = 150\,\mathrm{s}$ (right before the start of venting) in the numerical model of the experiments from Chamoun et al. [24]. The plan view (Figure 5a) shows the decreasing sediment concentration along the length of the turbidity current as a result of dilution and settling. The height of the current can be observed in the longitudinal section (Figure 5b). The contour plot shows the decreasing height of the turbidity current from the inlet towards the current head. At the head the current height is increasing again.

Sediment concentration decreases strongly along the first metre of the channel to approximately 25% of the inlet concentration (Figure 5a). Along the remaining part of the channel, sediment concentration is more or less constant with about 20% of the inlet concentration. The current head is apparent through the sharp drop in concentration to almost 0 ppm.

Similarly, the turbidity current height with respect to sediment concentration in the longitudinal section in Figure 5b drops mainly along the first half of a metre of the channel. From that point the slope of the surface of the current is relatively small. The minimum current height is located about 1.5 m behind the current head. From this point onwards, the current height starts to increase again.

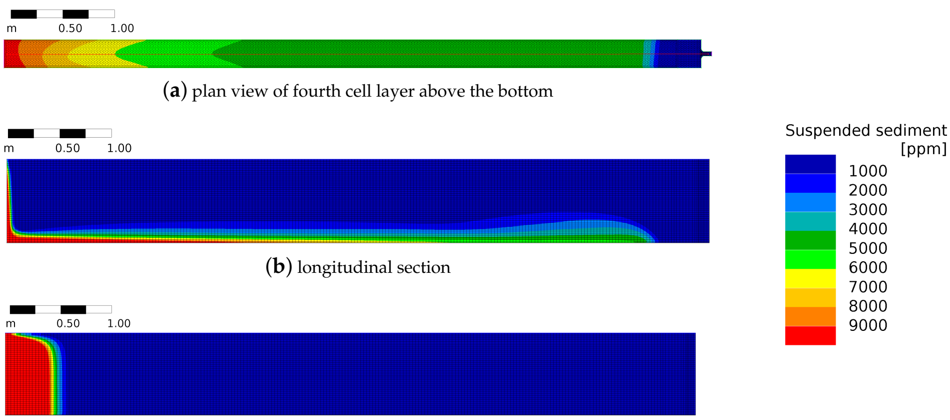


(**a**) plan view of fourth cell layer above the bottom

(**b**) longitudinal section

(**c**) longitudinal section, no buoyant forces

**Figure 5.** Sediment concentration contours in ppm at the start of venting ($t = 150\,\mathrm{s}$, maximum concentration: 23,000 ppm).

*Water* **2020**, *12*, 1403 

For the purpose of comparison one extra simulation was run in which the source term for bouyant forces Equation (4) was neglected. The longitudinal section of the concentration field in the results of this simulation at $t = 150$ s is displayed in Figure 5c. The figure shows that the sediment has been transported less than half a metre from the inlet. This transport is only driven by the velocity at the inflow boundary. The height of the current reduced slightly as a result of settling.

Figure 6a displays the velocity of the turbidity current along the channel length normalized with a fall velocity of 0.0015 m s$^{-1}$ at time $t = 150$ s. It can be seen that the velocity of the turbidity current decays along its length. At the beginning of the channel the velocity is almost 60 times the fall velocity. In the current head the velocity is constant with a magnitude of approximately 30 times the fall velocity. In the front of the current head the velocity drops sharply. At all points along the channel the normalized velocity of the current was slightly higher in the numerical model than in the physical model [24].

The temporal evolution of the sediment concentration of the vented suspension at a venting degree of $\phi_{\mathrm{VENT}} = 80\%$ is displayed in Figure 6b. After an initial peak vented sediment concentration of about 17% of the inlet concentration at the start of venting, the concentration approaches a constant value of about 11–12% of the inflow concentration. The concentration measured in the physical experiment [24] fluctuates around this value with an amplitude of about 5% of the inflow concentration.

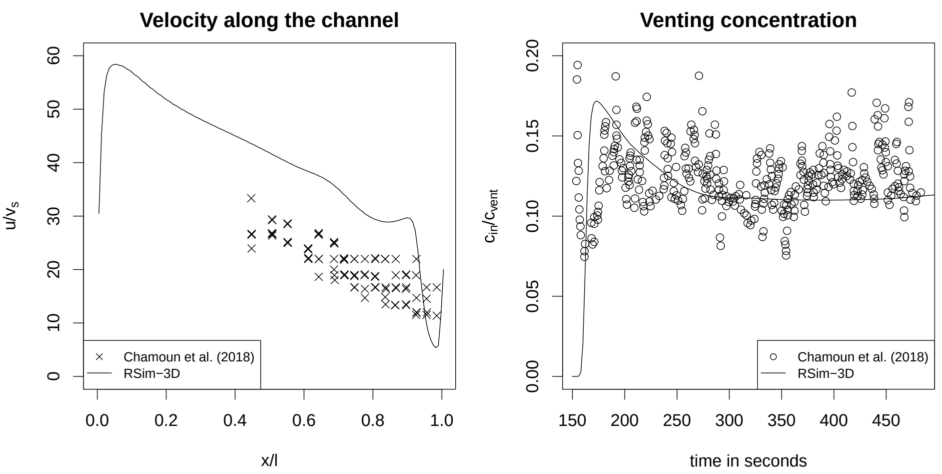


(**a**) velocity along the channel at $t = 150$ s

(**b**) concentration time series after bottom outlet opening with $\phi_{\mathrm{VENT}} = 80\%$

**Figure 6.** Results of the venting experiments [24].

Figure 7 displays a longitudinal section of the concentration field after 350 s of venting ($t = 500$ s). At this point the flow should have reached steady state condition [24]. The images show the reflection of the turbidity current at the end wall of the channel and the return flow caused by the reflection. The return flow is decreasing with increasing venting degree.

The lower the venting degree, the further the return flow travels back towards the inlet of the channel. As the return flow causes additional resistance for the arriving turbidity current, the turbidity current slows down and increases in height. This way at venting degrees of $\phi_{\mathrm{VENT}} < 100\%$ two regions with a circular flow patterns form, visible in Figure 7a,b.

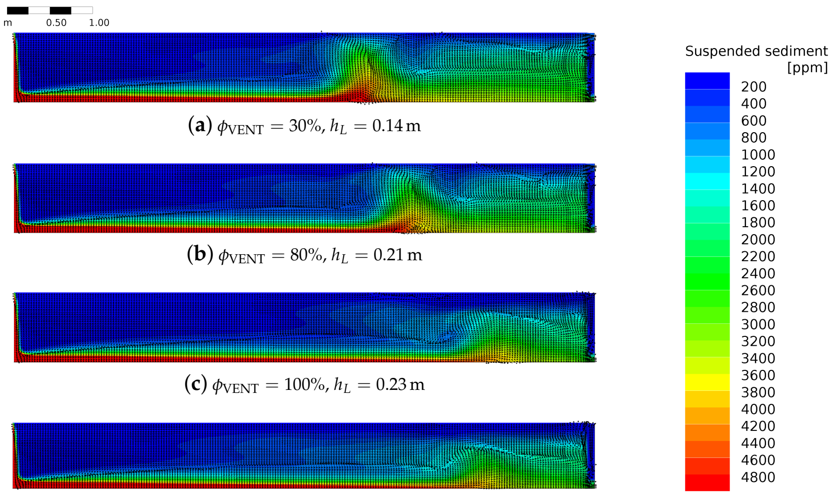


**Figure 7.** Longitudinal section through the sediment concentration field in the channel with suspended sediment concentration contours in ppm at different venting degrees $\phi_{\text{VENT}}$. The plots display a situation 350 s after the start of venting when steady state conditions have been reached. The velocity field is displayed by velocity vectors (unscaled).

Figure 8 displays global venting efficiency and the normalized venting time $\bar{t}$. Global venting efficiency is initially strongly increasing at the start of venting. The slope of the lines is then decreasing to a constant value when the flow in the channel reaches a steady state.

The initial slope of the lines for global venting efficiency ($\bar{t} < 200$) in Figure 8 is higher in the numerical model results than in the outcomes of the physical model. This causes a slightly higher global venting efficiency in the numerical model. After this initial period, the slope of the lines for global venting efficiency from the numerical model matches the slope of the respective lines from the physical model.

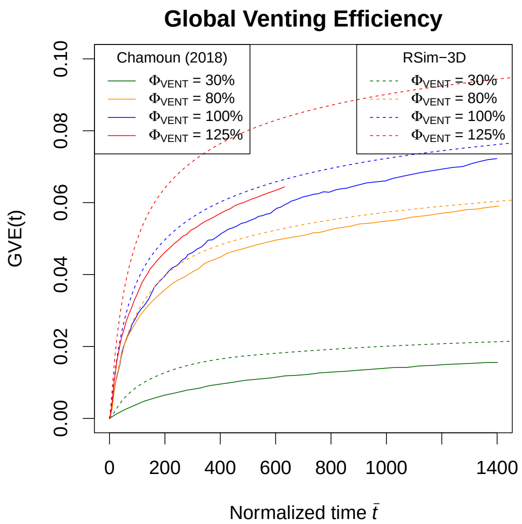


**Figure 8.** Global venting efficiency at different venting degrees $\phi_{\text{VENT}}$.

### 3.4. Sediment Deposition Along the Channel

For the case with a venting degree of $\phi_{\text{VENT}} = 80\%$ sediment deposition along the channel has been recorded and compared to respective measurements by Chamoun et al. [24]. The results of sediment deposition are displayed in Figure 9.

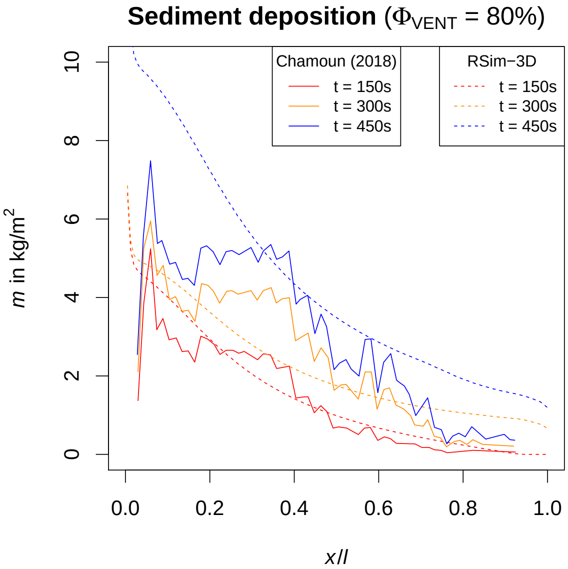


**Figure 9.** Sediment deposition along the channel at a venting degree of $\phi_{\text{VENT}} = 80\%$.

Figure 9 shows decreasing sediment deposition along the channel length. While the initial peak of sediment deposition is right at the inflow section in the numerical model results it occured slightly downstream in the physical model. For the time steps $t = 150$ s (start of venting) the deposition in the simulation results from the RSim-3D solver agrees fairly well with the measured deposition in the laboratory experiments [24]. At $t = 300$ s the accumulation of sediment in the second quarter of the channel visible in the physical model results is not reproduced in the numerical model, while the remaining sections are in agreement. At $t = 450$ s sediment deposition in the numerical model is overestimated compared to the physical model along the first third of the channel length.

## 4. Discussion

### 4.1. Code Verification and Validation

The general formation of the current at different time steps during the slumping phase in Figure 3 can be compared to theoretical models and pictures from laboratory experiments (e.g., [13]). Theory in literature suggests that the total volume of the current remains constant during the slumping phase of a gravity current. In addition, the height of the current is assumed to be constant along its length so it can be approximated with rectangular boxes [13]. This theory holds true for the numerically modelled particle-driven gravity current. Particularly at time steps $t = 12$ s and $t = 18$ s in Figure 3c,d the surface of the turbidity current is relatively flat. Discrepancies between the results of the numerical model and the theory of gravity currents [13] can be explained by the process of particle settling. Due to this process the sediment load in the current is continuously decreasing and potential energy is lost [8].

Initial velocity of the numerically modelled particle-driven gravity current is constant and of the same magnitude for about 20 s in all cases displayed in Figure 4. This is typical for the slumping phase [13,19]. After this phase the flow front advance decays depending on the fall velocity of the particles which is described by An et al. [29].

According to the particle-driven gravity classification with respect to the deposition rate [29], the turbidity current in case A corresponds to a mixed regime. This is in contrast to case G which features a turbidity current in the deposition regime. In the latter the deceleration as a result of the setting of particles [29] can clearly be observed at $20\,\mathrm{s} < t < 40\,\mathrm{s}$ (see Figure 4c). This shows that the code is capable of modelling the effect of particle settling described by An et al. [29].

The comparison of the flow front advance in the physical [19] and numerical model in Figure 4 allows a quantitative comparison of the results. Using sufficiently fine meshes it has been achieved to reproduce the particle-driven gravity current for all four grain size distributions considered with reasonable accuracy.

It is assumed that inaccuracies in the flow front distance towards the end of each experiment are a result of post-processing. Gladstone et al. [19] visually determined the position of the flow front which might involve inaccuracies when the turbidity becomes low as a result of dilution. In addition, when the concentration gradient at the flow front decreases the position of the flow front in the numerical model is more sensitive to the choice of the minimum concentration defining the flow front (10 ppm, see Section 3.1).

### *4.2. Mesh Sensitivity Analysis and Quantitative Error Analysis*

To study mesh convergence Figure 10 displays the position of the flow front at time $t = 111\,\mathrm{s}$ for cases A, D and R and $t = 84\,\mathrm{s}$ for case G, respectively. The displayed results have been retrieved from simulations on different meshes and with different time steps. In all cases the curve flattens with increasing mesh refinement, showing mesh convergence. The curves have the steepest slope between the results of the meshes `3v120` (42,160 cells) and `3v130` (63,240 cells). Between those two meshes a refinement is only made in the vertical direction. This suggests that sufficient fine vertical spatial discretization is particularly crucial for modelling turbidity currents. Further discussion of the mesh convergence on the basis of the grid convergence index [58,59] has been dismissed. The complexity of the mesh and different refinement ratios in horizontal and vertical direction make this approach impractical.

For cases A, D and R the flow front advance in Figure 10 approaches a value within the boundaries of accuracy of the measured flow front advance from the physical model [19]. In case G flow front advance in the numerical model is higher than the measured flow front advance. This suggests that the fall velocity estimated using Equation (2) might be too low. In such cases the accuracy can possibly be optimized for the particular particles in the suspension by calibration with respect to fall velocity (see also Section 2.1.2).

Table 4 displays normalized Euclidean norms ($p2$-norms, Equation (8)) of the error (difference) $\boldsymbol{\epsilon}$ between the flow front advance in the numerical and the physical model. To compare the error norms of simulations with different numbers of saved time steps, the norms are normalized by division by the number of data points $n$.

$$||\boldsymbol{\epsilon}||_2 = \frac{\boldsymbol{\epsilon} \cdot \boldsymbol{\epsilon}}{n} \tag{8}$$

For all cases $p2$-norms in Table 4 remain relatively constant or are even slightly increasing with refinement from the second finest to the finest mesh. Similarly, the reduction of the time step from the second lowest to the lowest did only result in minor changes of the error norms. This suggests that the discretization error has been reduced to a minimum. The remaining error is driven by other factors rather than spatial or temporal discretization. These include model assumptions such as the estimation of fall velocity using Equation (2) or simplifications (see Section 2.1). Thus mesh convergence has been achieved.

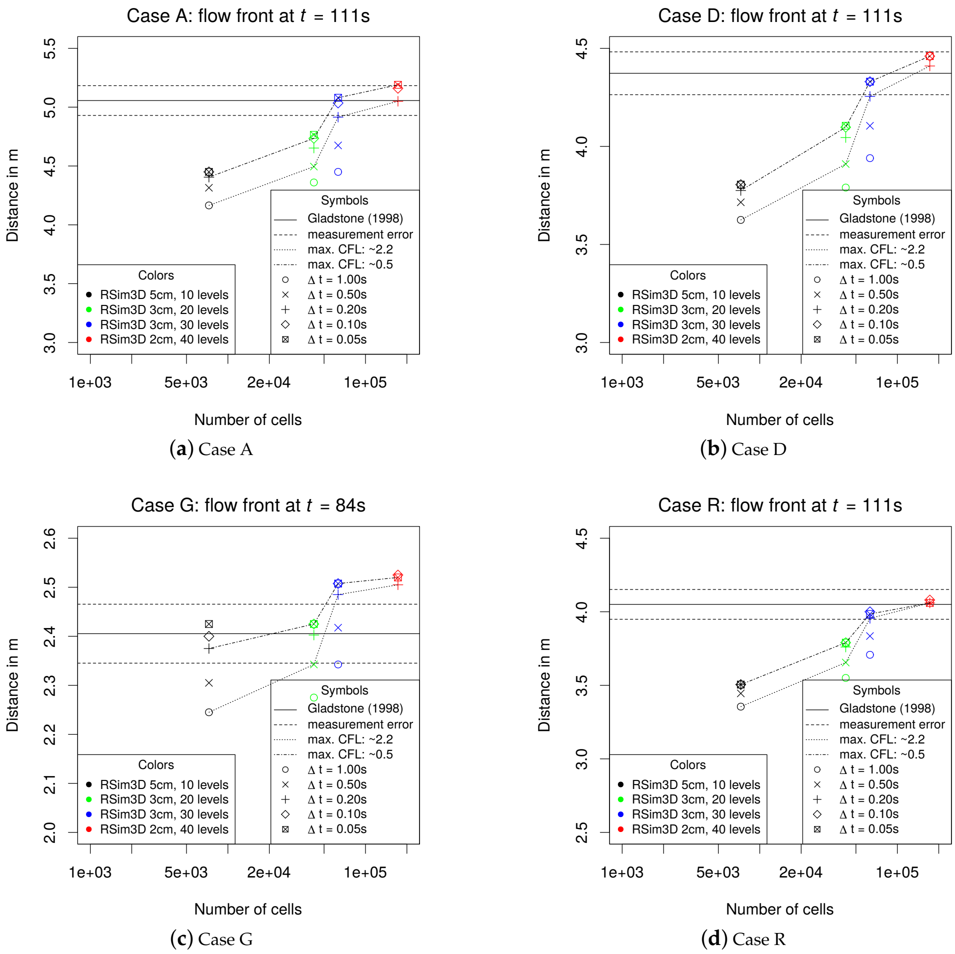


**Figure 10.** Mesh convergence of the numerical models of lock exchange experiments. The cases differ in their composition of particle sizes in the suspension: (**a**) Case A $d = 25\,\mu\text{m}$. (**b**) Case D $d_1 = 25\,\mu\text{m}$, $d_2 = 69\,\mu\text{m}$. (**c**) Case G $d = 69\,\mu\text{m}$. (**d**) Case R $d_1 = 17\,\mu\text{m}$, $d_2 = 37\,\mu\text{m}$, $d_3 = 63\,\mu\text{m}$, $d_4 = 88\,\mu\text{m}$, $d_5 = 105\,\mu\text{m}$. In cases including more than one grain size the total sediment concentration is uniformly distributed across all fractions.

For cases A, D and R $p2$-norms are decreasing with the first three steps of mesh refinement. While a decrease of the error has been achieved with further mesh refinement to the finest mesh in case A, error norms are slightly increasing on the finest mesh in the other cases.

In contrast $p2$-norms in case G are increasing with refinement of the mesh `3v120`. This can be explained with the overestimation of the flow front advance in this model (see above and Figure 4c, Figure 10c). Despite this, the $p2$-norm is approaching a constant value on the fine meshes which shows that mesh convergence has been achieved (see above).

In conclusion, a horizontal cell size of 3 cm and 30 vertical layers (63,240 cells) are necessary for achieving the highest accuracy of the model of the lock exchange experiments. This agrees well with the results of the mesh sensitivity analysis of Georgoulas et al. [9]. They found an entirely structured hexahedral mesh with 68,950 cells to be most practical for a numerical model of the lock exchange experiments from Gladstone et al. [19].

**Table 4.** Euclidean norms of the difference between the flow front in the physical [19] and numerical model with different spatial and temporal discretization. The cases differ in their composition of particle sizes in the suspension: Case A $d = 25\,\mu m$; Case D $d_1 = 25\,\mu m$, $d_2 = 69\,\mu m$; Case G $d = 69\,\mu m$ and Case R $d_1 = 17\,\mu m$, $d_2 = 37\,\mu m$, $d_3 = 63\,\mu m$, $d_4 = 88\,\mu m$, $d_5 = 105\,\mu m$. In cases including more than one grain size the total sediment concentration is uniformly distributed across all fractions.

| $\Delta ts$ | 5v110 | 3v120 | 3v130 | 2v140 | 5v110 | 3v120 | 3v130 | 2v140 |
|---|---|---|---|---|---|---|---|---|
| | | Case | A | | | Case | D | |
| 1.00 | 0.515 | 0.315 | 0.224 | – | 0.405 | 0.245 | 0.128 | – |
| 0.50 | 0.396 | 0.216 | 0.110 | – | 0.309 | 0.145 | 0.049 | – |
| 0.20 | 0.318 | 0.127 | 0.035 | 0.017 | 0.237 | 0.072 | 0.017 | 0.021 |
| 0.10 | 0.282 | 0.091 | 0.018 | 0.011 | 0.213 | 0.051 | 0.013 | 0.024 |
| 0.05 | 0.273 | 0.077 | 0.013 | 0.011 | 0.230 | 0.049 | 0.011 | 0.022 |
| | | Case | G | | | Case | R | |
| 1.00 | 0.026 | 0.018 | 0.006 | – | 0.348 | 0.186 | 0.080 | – |
| 0.50 | 0.014 | 0.006 | 0.002 | – | 0.276 | 0.107 | 0.028 | – |
| 0.20 | 0.008 | 0.003 | 0.004 | 0.007 | 0.221 | 0.056 | 0.010 | 0.020 |
| 0.10 | 0.006 | 0.002 | 0.006 | 0.010 | 0.210 | 0.045 | 0.008 | 0.021 |
| 0.05 | 0.005 | 0.002 | 0.007 | 0.010 | 0.229 | 0.047 | 0.007 | 0.016 |

In order to get best results on a certain mesh a sufficiently small time step is required. While reducing the time step substantially improves the accuracy of the results (see Figure 10 and Table 4) it comes at only minimum additional computational effort (see Table 3). The low increase in computation time compared to the additional number of time steps for which the equations need to be solved can be explained by the smaller number of iterations required for the SIMPLE solver to converge at each time step.

### 4.3. Venting

The shape of the turbidity current in Figure 5 matches the data from the physical experiments [24]. The height of the current in the results of the numerical model is about 40% of the channel height. This is 10% less than the current height observed by Chamoun et al. [24]. The reason for this underestimation can possibly be insufficient accuracy of the Stokes fall velocity Equation (2). In addition, the approximation of the grain size distribution in Table 2 might be inaccurate since only values for $d_{10}$, $d_{50}$ and $d_{90}$ are provided by Chamoun et al. [24]. The return flow caused by the reflection of the turbidity current at the end wall described in literature (e.g., [17,24]) is also visible in the results from the numerical model in Figure 5.

The development of convective velocity along the channel length in Figure 6a from the numerical model is similar to the measured velocity from the physical model [24]. This comes with the restriction that absolute value of normalized velocity is higher in the numerical model than the measured velocity in the physical one. As the ratio between the numerically modelled and measured velocity is more or less constant, it is assumed that this offset is caused by using only the fall velocity of the particle diameter $d_{50}$ for normalization of flow velocity. This very likely does not sufficiently represent the mixture of particles driving the turbidity current. Fall velocities of particles in the suspension range from $0.4\,mm\,s^{-1}$ to $3.7\,mm\,s^{-1}$ (see also Table 2). The normalized velocity in the numerical model would agree with the measured velocity in the physical model, when a fall velocity of 2.3 mm was used for normalization.

The average sediment concentration of the vented suspension is similar in the numerical and physical model [24]. The limitation in this comparison is that the temporal variation of the concentration which has been measured in the physical model has not been captured with the numerical model.

It is not expected that this temporal variation causes substantial influence on the results for overall venting performance prediction. Venting performance usually is analysed integrated over time (see e.g., Equation (6)).

In the longitudinal sections of the concentration field with different venting degrees $\phi_{VENT}$ in Figure 7 return flow is clearly visible in cases with a venting degree lower than 1 (Figure 7a,b). This return flow is lower in the models with a venting degree of $\phi_{VENT} = 100\%$ and $\phi_{VENT} = 125\%$ in Figure 7c,d. Furthermore the figure also shows that the height of the turbidity current reduces with increasing venting degree $\phi_{VENT}$. This matches observations described by Chamoun et al. [24].

While a clear difference in the concentration contours in Figure 7 is visible comparing the cases with $\phi_{VENT} = 30\%$ (Figure 7a), $\phi_{VENT} = 80\%$ (Figure 7b) and $\phi_{VENT} = 100\%$ (Figure 7c) the concentration field does not appear to change with further increase of the venting degree to $\phi_{VENT} = 125\%$ (Figure 7d). This agrees with the conclusion of Chamoun et al. that highest venting efficiency can be achieved with a venting degree of $\phi_{VENT} = 100\%$ [24].

Comparing global venting efficiency of the numerical model with global venting efficiency of the physical model [24] in Figure 8 reveals that venting efficiency is generally overestimated in the numerical model. The overestimation of global venting efficiency in the numerical model is particularly high in the case with the highest venting degree $\phi_{VENT} = 125\%$. A possible explanation for this is the second order upwind discretization of the convection part of the Navier-Stokes momentum Equation (1) in the RSim-3D code. This scheme does not allow influence of a downstream cell on convection of velocity. Thus "suction" from the bottom outlet is only propagated to upstream cells through the pressure source term in the momentum equation and the pressure correction equation. This might cause an underestimation of the velocity in the area of the bottom outlet. As a result less clear water is vented through the bottom outlet and the concentration of the vented suspension is overestimated. To overcome this issue, a non-upwind scheme for the advection of velocity could be implemented in the model.

Sediment deposition along the channel could also be captured fairly well with the developed solver. Particularly for the earliest time step ($t = 150$ s) displayed in Figure 9 the deposited amount of sediment in the numerical model agrees well with the laboratory measurements [24]. In the physical model results [24] a plateau in sediment deposition occurs along the second quarter of the channel which is not captured by the numerical model. In addition, at the latest time step ($t = 450$ s) sediment deposition along the first third of the channel length is overestimated in the numerical model. The reason for the discrepancies between the sediment deposition in the numerical and physical model results is credited to the missing implementation of resuspension in the numerical model (see Section 2.1.2). While in reality a balance between sediment deposition and resuspension might be reached in the upstream section of the channel as soon as enough sediment has accumulated on the bottom, the latter process is not captured by the numerical model. Thus, the accumulation of sediment at the bottom is overestimated. In addition sediment might be transported from the first quarter to the second quarter of the channel as bed load. Bed load transport is also not considered in the current version of the model.

### 4.4. Applicability of the Code to Real Reservoirs

The results of the test cases show that the developed code can accurately model turbidity currents. Using the code it seems to be possible to numerically model the turbidity current from the entrance into the reservoir to the dam without having to rely on empirical models. This provides an advantage compared to earlier studies (e.g., [10]). In addition the solver RSim-3D has been developed with particular focus on river applications [42] while earlier studies were relying on commercial CFD codes with focus on other applications (e.g., [7,11,32,36]). This specialization of the RSim-3D solver allows to efficiently apply the developed code to real reservoirs in their natural size and shape.

The effect of density gradients as a result of different spatially distributed sediment concentrations can be seen by comparing Figure 5b,c. The development of the sediment plume is substantially different in the simulation including the source term for buoyant forces (Figure 5b) compared to Figure 5c. This observation agrees with the statement of DeCesare et al. that turbidity currents are the main transport mechanism for sediments in reservoirs [7]. In consequence it can be concluded that buoyant forces should be a substantial part of computational fluid dynamics models of reservoirs.

Limitations in the current version of the model are related to the storage type of the reservoir. Water in reservoirs for long term storage often has a different temperature than the inflowing water. Thus density differences also result from temperature gradients which are neglected in the current version of the model. Hence the application of the RSim-3D solver for turbidity currents is limited to reservoirs for short term storage.

The mesh sensitivity study shows that reasonable results can be achieved even on rather coarse meshes. The computation time on a desktop computer of the model of the lock exchange cases was less than half an hour using the coarsest mesh (`5vl12`, 7280 cells) and between two and three days (depending on the convergence) using the finest mesh (`2vl40`, 172,200 cells, see Table 3). This is particularly relevant considering the problem of long computation times with 3D models of turbidity currents in reservoirs mentioned by Lee et al. [11]. Although the computation time is still too long for real-time studies, the model may allow a detailed analysis of the turbidity current in a reservoir in reasonable time. In order to finally confirm the applicability of the RSim-3D code to model turbidity in real reservoirs a test using a real reservoir geometry remains to be done as future work.

## 5. Conclusions

The existing hydrodynamic code RSim-3D [42,45] was successfully extended to model particle-driven gravity currents. Test cases show that the numerical model converges with mesh refinement and reduction of the time step. The flow front advance in lock exchange experiments agrees well with the literature data [19]. The general relevance of including gravity currents into computational fluid dynamics models of reservoirs is emphasized by comparing two simulations with and without buoyant forces. The results show that the flow in the studied test case is substantially driven by buoyant forces. Accuracy can potentially be increased through calibration of fall velocity. Further development of the model can be done by the implementation of bottom exchange including resuspension which is not mesh dependent.

Turbidity currents with continuous sediment inflow from experiments of Chamoun et al. [24] have successfully been reproduced numerically using the developed code. A comparison of the concentration field during venting shows the influence of the venting degree on the sediment distribution in the channel. A limitation of the model is the upstream propagation of the "suction" from the bottom outlet during venting. It is assumed that this is due to the second order upwind discretization scheme used for convection of velocity in the momentum equations. As a result, the vented sediment concentration at the bottom outlet is overestimated in the numerical model, particularly at higher venting degrees of $\phi_{\mathrm{VENT}} > 100\%$. Thus to improve the accuracy of the numerical code in the immediate area of the bottom outlet a non-upwind scheme for the advection of velocity can be implemented.

Moreover, sediment deposition could be captured fairly well with the numerical model. This comes with the restriction of the missing implementation of resuspension of sediment. In addition, sediment transported as bed load in the physical model was not transported in the numerical model.

In conclusion, the test cases show that RSim-3D with the newly implemented functionality to model density currents provides the general capability to study turbidity currents in real reservoirs. The computational effort is low enough that reasonable results can be achieved on a current desktop computer in less than one week's time.

**Author Contributions:** Conceptualization: D.W. and M.T.; Data curation: D.W.; Formal analysis: D.W.; Funding acquisition: M.T., C.H. and H.H.; Investigation: D.W.; Methodology: D.W. and M.T.; Project administration M.T. and C.H.; Resources: M.T. and C.H.; Software: D.W. and M.T.; Supervision: M.T. and C.H. and H.H.; Validation: D.W., M.T. and C.H.; Visualization: D.W.; Writing—original draft: D.W.; Writing—review & editing: M.T., C.H. and H.H.; All authors have read and agreed to the published version of the manuscript.

**Funding:** This paper was written as a contribution to the Christian Doppler Laboratory for Sediment Research and Management. In this context, the financial support by the Christian Doppler Research Association, the Austrian Federal Ministry for Digital and Economic Affairs and the National Foundation for Research, Technology and Development is gratefully acknowledged.

**Acknowledgments:** The computational results presented have been achieved in part using the Vienna Scientific Cluster (VSC).

**Conflicts of Interest:** The authors declare no conflict of interest. The funders had no role in the design of the study; in the collection, analyses, or interpretation of data; in the writing of the manuscript, or in the decision to publish the results.

## Abbreviations

The following abbreviations are used in this manuscript:

| | |
|---|---|
| CFD | computational fluid dynamics |
| GVE | global venting efficiency |
| VENT | venting |

## References

1. Hauer, C.; Wagner, B.; Aigner, J.; Holzapfel, P.; Flödl, P.; Liedermann, M.; Tritthart, M.; Sindelar, C.; Pulg, U.; Klösch, M.; et al. State of the art, shortcomings and future challenges for a sustainable sediment management in hydropower: A review. *Renew. Sustain. Energy Rev.* **2018**, *98*, 40–55. [CrossRef]
2. Esmaeili, T.; Sumi, T.; Kantoush, S.A.; Kubota, Y.; Haun, S.; Ruther, N. Three-Dimensional Numerical Study of Free-Flow Sediment Flushing to Increase the Flushing Efficiency: A Case-Study Reservoir in Japan. *Water* **2017**, *9*, 900. [CrossRef]
3. Chamoun, S.; De Cesare, G.; Schleiss, A.J. Managing reservoir sedimentation by venting turbidity currents: A review. *Int. J. Sediment Res.* **2016**, *31*, 195–204. [CrossRef]
4. Boes, R.; Auel, C.; Müller-Hagmann, M.; Albayrak, I. Sediment bypass tunnels to mitigate reservoir sedimentation and restore sediment continuity. In *Reservoir Sedimentation*; Taylor & Francis Group: London, UK, 2014; pp. 221–228. [CrossRef]
5. Habersack, H.; Bogner, K.; Schneider, J.; Brauner, M. Catchment-Wide Analysis of the Sediment Regime with Respect to Reservoir Sedimentation. *Int. J. Sediment Res.* **2000**, *16*, 159–169.
6. Omelan, M.; Visscher, J.; Rüther, N.; Stokseth, S. Sediment management for sustainable hydropower development. In Proceedings of the 13th International Symposium on River Sedimentation (ISRS 2016), Stuttgart, Germany, 19–22 September 2016; Wieprecht, S., Haun, S., Weber, K., Noack, M., Terheiden, K., Eds.; CRC Press Taylor & Francis Group: London, UK, 2017; pp. 1132–1140.
7. De Cesare, G.; Schleiss, A.; Hermann, F. Impact of turbidity currents on reservoir sedimentation. *J. Hydraul. Eng.* **2001**, *127*, 6–16. [CrossRef]
8. Necker, F.; Härtel, C.; Kleiser, L.; Meiburg, E. High-resolution simulations of particle-driven gravity currents. *Int. J. Multiph. Flow* **2002**, *28*, 279–300. [CrossRef]
9. Georgoulas, A.; Angelidis, P.; Panagiotidis, T.; Kotsovinos, N. 3D Numerical modelling of turbidity currents. *Environ. Fluid Mech.* **2010**, *10*, 603–635. [CrossRef]
10. Huang, C.C.; Lin, W.C.; Ho, H.C.; Tan, Y.C. Estimation of Reservoir Sediment Flux through Bottom Outlet with Combination of Numerical and Empirical Methods. *Water* **2019**, *11*, 1353. [CrossRef]
11. Lee, F.Z.; Lai, J.S.; Tan, Y.C.; Sung, C.C. Turbid density current venting through reservoir outlets. *KSCE J. Civ. Eng.* **2014**, *18*, 694–705. [CrossRef]
12. Liu, L.; Wang, Y. Modelling Reservoir Turbidity Using Landsat 8 Satellite Imagery by Gene Expression Programming. *Water* **2019**, *11*, 1479. [CrossRef]
13. Huppert, H.E.; Simpson, J.E. The slumping of gravity currents. *J. Fluid Mech.* **1980**, *99*, 785–799. [CrossRef]

14. La Rocca, M.; Adduce, C.; Sciortino, G.; Pinzon, A. Experimental and numerical simulation of three-dimensional gravity currents on smooth and rough bottom. *Phys. Fluids* **2008**, *20*, 106603. [CrossRef]
15. Musumeci, R.; Viviano, A.; Foti, E. Influence of Regular Surface Waves on the Propagation of Gravity Currents: Experimental and Numerical Modeling. *J. Hydraul. Eng.* **2017**, *143*. [CrossRef]
16. Stancanelli, L.M.; Musumeci, R.E.; Foti, E. Dynamics of Gravity Currents in the Presence of Surface Waves. *J. Geophys. Res. Ocean.* **2018**, *123*, 2254–2273. [CrossRef]
17. Fan, J.H. Experimental studies on density currents. *Sci. Sin.* **1960**, *4*, 275–303.
18. Bonnecaze, R.T.; Huppert, H.E.; Lister, J.R. Particle-driven gravity currents. *J. Fluid Mech.* **1993**, *250*, 339–369. [CrossRef]
19. Gladstone, C.; Phillips, J.C.; Sparks, R.S.J. Experiments on bidisperse, constant-volume gravity currents: propagation and sediment deposition. *Sedimentology* **1998**, *45*, 833–843. [CrossRef]
20. De Rooij, F.; Dalziel, S.B. Time- and Space-Resolved Measurements of Deposition under Turbidity Currents. In *Particulate Gravity Currents*; Blackwell Science Ltd.: Oxford, UK, 2001; pp. 207–215. [CrossRef]
21. Baas, J.H.; Van Kesteren, W.; Postma, G. Deposits of depletive high-density turbidity currents: A flume analogue of bed geometry, structure and texture. *Sedimentology* **2004**, *51*, 1053–1088. [CrossRef]
22. Sequeiros, O.; Naruse, H.; Endo, N.; Garcia, M.; Parker, G. Experimental study on self-accelerating turbidity currents. *J. Geophys. Res. Ocean.* **2009**, *114*. [CrossRef]
23. Sequeiros, O.; Spinewine, B.; Beaubouef, R.; Sun, T.; Garcia, M.; Parker, G. Bedload transport and bed resistance associated with density and turbidity currents. *Sedimentology* **2010**, *57*, 1463–1490. [CrossRef]
24. Chamoun, S.; De Cesare, G.; Schleiss, A.J. Venting of turbidity currents approaching a rectangular opening on a horizontal bed. *J. Hydraul. Res.* **2018**, *56*, 44–58. [CrossRef]
25. Chamoun, S.; De Cesare, G.; Schleiss, A.J. Management of turbidity current venting in reservoirs under different bed slopes. *J. Environ. Manag.* **2017**, *204*, 519–530. [CrossRef] [PubMed]
26. Chamoun, S.; De Cesare, G.; Schleiss, A.J. Influence of Operational Timing on the Efficiency of Venting Turbidity Currents. *J. Hydraul. Eng.* **2018**, *144*. . [CrossRef]
27. La Rocca, M.; Adduce, C.; Sciortino, G.; Pinzon, A.; Boniforti, M. A two-layer, shallow-water model for 3D gravity currents. *J. Hydraul. Res.* **2012**, *50*, 208–217. [CrossRef]
28. La Rocca, M.; Prestininzi, P.; Adduce, C.; Sciortino, G.; Hinkelmann, R. Lattice Boltzmann simulation of 3D gravity currents around obstacles. *Int. J. Offshore Polar Eng.* **2013**, *23*, 178–185.
29. An, S.; Julien, P.Y.; Venayagamoorthy, S.K. Numerical simulation of particle-driven gravity currents. *Environ. Fluid Mech.* **2012**, *12*, 495–513. [CrossRef]
30. Stancanelli, L.; Musumeci, R.; Foti, E. Computational Fluid Dynamics for Modeling Gravity Currents in the Presence of Oscillatory Ambient Flow. *Water* **2018**, *10*, 635. [CrossRef]
31. Cantero, M.I.; Balachandar, S.; García, M.H. An Eulerian–Eulerian model for gravity currents driven by inertial particles. *Int. J. Multiph. Flow* **2008**, *34*, 484 – 501. [CrossRef]
32. An, S.; Julien, P.Y. Three-Dimensional Modeling of Turbid Density Currents in Imha Reservoir, South Korea. *J. Hydraul. Eng.* **2014**, *140*, 05014004. [CrossRef]
33. Deltares. *Delft3D-FLOW*; Deltares: Delft, The Netherlands, 2014.
34. Shields, A. Anwendung der Ähnlichkeitsmechanik und der Turbulenzforschung auf die Geschiebebewegung. In *Mitteilungen der Preußischen Versuchsanstalt für Wasser- Erd- und Schiffbau*; Preußische Versuchsanstalt für Wasser- Erd- und Schiffbau: Berlin, Germany, 1936.
35. Cantero, M.; García, M.; Balachandar, S. Effect of particle inertia on the dynamics of depositional particulate density currents. *Comput. Geosci.* **2008**, *34*, 1307–1318. [CrossRef]
36. Lavelli, A.; Boillat, J.J.; De Cesare, G. Numerical 3D modelling of the vertical mass exchange induced by turbidity currents in Lake Lugano (Switzerland). In Proceedings 5th International Conference on Hydro-Science and- Engineering (ICHE-2002), Warsaw, Poland, 18–21 September 2002.
37. Hillebrand, G.; Klassen, I.; Olsen, N.R.B. 3D CFD modelling of velocities and sediment transport in the Iffezheim hydropower reservoir. *Hydrol. Res.* **2017**, *48*, 147–159. [CrossRef]
38. NTNU—Norwegian University of Science and Technology. SSIIM. 2019. Available online: http://folk.ntnu.no/nilsol/ssiim/ (accessed on 18 January 2020).
39. Olsen, N.R.B. *SSIIM*; Norwegian University of Science and Technology: Trondheim, Norway, 2018.
40. Lai, Y.G. Two-Dimensional Depth-Averaged Flow Modeling with an Unstructured Hybrid Mesh. *J. Hydraul. Eng.* **2010**, *136*, 12–23. [CrossRef]

41. Rouse, H. Modern conceptions of the mechanics of fluid turbulence. *Trans. Am. Soc. Civ. Eng.* **1937**, *102*, 463–505.
42. Tritthart, M. Three-dimensional numerical modelling of turbulent river flow using polyhedral finite volumes. In *Wiener Mitteilungen*; Vienna University of Technology: Vienna, Austria, 2005; Volume 193.
43. Tritthart, M.; Schober, B.; Liedermann, M.; Habersack, H. Development of an integrated sediment transport model and its application to the Danube River. In Proceedings of the 33rd IAHR Congress, Vancouver, BC, Canada, 9–14 August 2009; pp. 876–883.
44. Tritthart, M.; Schober, B.; Habersack, H. Non-uniformity and layering in sediment transport modelling 1: Flume simulations. *J. Hydraul. Res.* **2011**, *49*, 325–334. [CrossRef]
45. Tritthart, M.; Gutknecht, D. Three-Dimensional Simulation of Free-Surface Flows Using Polyhedral Finite Volumes. *Eng. Appl. Comput. Fluid Mech.* **2007**, *1*, 1–14. [CrossRef]
46. Farhadi, A.; Mayrhofer, A.; Tritthart, M.; Glas, M.; Habersack, H. Accuracy and comparison of standard k-E with two variants of k- turbulence models in fluvial applications. *Eng. Appl. Comput. Fluid Mech.* **2018**, *12*, 216–235. [CrossRef]
47. Launder, B.; Spalding, D. The numerical computation of turbulent flows. *Comput. Methods Appl. Mech. Eng.* **1974**, *3*, 269–289. [CrossRef]
48. Atkinson, J.F.; Chakraborti, R.K.; VanBenschoten, J.E. Effects of Floc Size and Shape in Particle Aggregation. In *Flocculation in Natural and Engineered Environmental Systems*, 1st ed.; CRC Press: Boca Raton, FL, USA, 2004; Chapter 5, pp. 95–120.
49. Van Rijn, L.C. Sediment Transport, Part II: Suspended Load Transport. *J. Hydraul. Eng.* **1984**, *110*, 1613–1641. [CrossRef]
50. Tritthart, M.; Hauer, C.; Haimann, M.; Habersack, H. Three dimensional variability of suspended load transport in rivers and its ecological implications in terms of reservoir flushing and reservoir drawdown. In Proceedings of the 38th IAHR World Congress, Panama City, FL, USA, 1–6 September 2019; pp. 3568–3575. [CrossRef]
51. Thonon, I.; Perk, M. Measuring suspended sediment characteristics using a LISST-ST in an embanked flood plain of the River Rhine. *IAHS-AISH Publ.* **2003**, *283*, 37–44,
52. Glock, K.; Tritthart, M.; Habersack, H.; Hauer, C. Comparison of Hydrodynamics Simulated by 1D, 2D and 3D Models Focusing on Bed Shear Stresses. *Water* **2019**, *11*, 226. [CrossRef]
53. Tritthart, M.; Liedermann, M.; Habersack, H. Modelling spatio-temporal flow characteristics in groyne fields. *River Res. Appl.* **2009**, *25*, 62–81. [CrossRef]
54. Tritthart, M.; Liedermann, M.; Schober, B.; Habersack, H. Non-uniformity and layering in sediment transport modelling 2: River application. *J. Hydraul. Res.* **2011**, *49*, 335–344. [CrossRef]
55. Haimann, M.; Hauer, C.; Tritthart, M.; Prenner, D.; Leitner, P.; Moog, O.; Habersack, H. Monitoring and modelling concept for ecological optimized harbour dredging and fine sediment disposal in large rivers. *Hydrobiologia* **2018**, *814*, 89–107. [CrossRef]
56. Glas, M.; Glock, K.; Tritthart, M.; Liedermann, M.; Habersack, H. Hydrodynamic and morphodynamic sensitivity of a river's main channel to groyne geometry. *J. Hydraul. Res.* **2018**, *56*, 714–726. [CrossRef]
57. Tritthart, M.; Haimann, M.; Habersack, H.; Hauer, C. Spatio-temporal variability of suspended sediments in rivers and ecological implications of reservoir flushing operations. *River Res. Appl.* **2019**, *35*, 918–931. [CrossRef]
58. Roache, P.J. *Fundamentals of Verification and Validation*; Hermosa Publishers: Socorro, NM, USA, 2009.
59. Slater, J.W. Examining Spatial (Grid) Convergence. 2008. Available online: https://www.grc.nasa.gov/www/wind/valid/tutorial/spatconv.html (accessed on 20 December 2019).

## 4.2 Water (2021): "Interaction of Very Large Scale Motion of Coherent Structures with Sediment Particle Exposure"



| | |
|---|---|
| Journal: | Water<br>This article belongs to the Special Issue "Advanced Modelling Strategies for Hydraulic Engineering and River Research"<br>The article has been highlighted as *Feature Paper* and *Editor's Choice*. |
| Volume: | 13 |
| Number: | 3 |
| Article number: | 248 |
| DOI: | https://doi.org/10.3390/w13030248 |
| Authors: | Sencer Yücesan, Daniel Wildt, Philipp Gmeiner, Johannes Schobesberger, Christoph Hauer, Christine Sindelar, Helmut Habersack and Michael Tritthart |
| Submitted: | 28th November 2020 |
| Accepted: | 16th January 2021 |
| Published: | 20th January 2021 |

Article available open access: https://www.mdpi.com/2073-4441/13/3/248


Highlights:

- LES models of turbulent channel flow over a smooth and a rough bed are set up.
- Time series of lift and drag forces on a particle, fully exposed over the smooth bed and half exposed and fully hidden over the rough bed were analysed.
- The influence of very large-scale motion of coherent structures on particle entrainment is shown.

water

MDPI

Article

# Interaction of Very Large Scale Motion of Coherent Structures with Sediment Particle Exposure

**Sencer Yücesan [1,2,*], Daniel Wildt [1,2], Philipp Gmeiner [1,2], Johannes Schobesberger [1,2], Christoph Hauer [1,2], Christine Sindelar [2], Helmut Habersack [2] and Michael Tritthart [2]**

[1] Christian Doppler Laboratory for Sediment Research and Management, Muthgasse 107, 1180 Vienna, Austria; daniel.wildt@boku.ac.at (D.W.); philipp.gmeiner@boku.ac.at (P.G.); johannes.schobesberger@boku.ac.at (J.S.); christoph.hauer@boku.ac.at (C.H.)

[2] Institute of Hydraulic Engineering and River Research (IWA), University of Natural Resources and Life Sciences, Muthgasse 107, 1180 Vienna, Austria; christine.sindelar@boku.ac.at (C.S.); helmut.habersack@boku.ac.at (H.H.); michael.tritthart@boku.ac.at (M.T.)

* Correspondence: s.yuecesan@boku.ac.at

**Abstract:** A systematic variation of the exposure level of a spherical particle in an array of multiple spheres in a high Reynolds number turbulent open-channel flow regime was investigated while using the Large Eddy Simulation method. Our numerical study analysed hydrodynamic conditions of a sediment particle based on three different channel configurations, from full exposure to zero exposure level. Premultiplied spectrum analysis revealed that the effect of very-large-scale motion of coherent structures on the lift force on a fully exposed particle resulted in a bi-modal distribution with a weak low wave number and a local maximum of a high wave number. Lower exposure levels were found to exhibit a uni-modal distribution.

**Keywords:** coherent structures; hairpin-vortex packets; hydrodynamic forces; particle entrainment; very-large-scale motions; turbulent channel flow



**Citation:** Yücesan, S.; Wildt, D.; Gmeiner, P.; Schobesberger, J.; Hauer, C.; Sindelar, C.; Habersack, H.; Tritthart, M. Interaction of Very Large Scale Motion of Coherent Structures with Sediment Particle Exposure. *Water* **2021**, *13*, 248. https://doi.org/10.3390/w13030248

Received: 28 November 2020
Accepted: 16 January 2021
Published: 20 January 2021



## 1. Introduction

Coherent structures in the vicinity of the wall region in turbulent flow have received significant attention after the pioneering findings of hairpin-like vortices [1] that possess spatial coherence. Boundary layer studies found that the streamwise elongated coherent structures carry intense turbulent kinetic energy (TKE) in the near wall region [2]. Velocity streaks are the primary examples of this. Kline et al. [3] described the motion of low-speed fluid flow from the viscous sublayer to the outer portions of the inner region as ejections, which are responsible for the production of TKE, whereas sweeps are responsible for the movement of high speed fluid flow towards the viscous sublayer. This quasi-cyclic organized motion of fluid flow is referred to as bursting [4]. Furthermore, it was indicated that the large-scale motion (LSM) of three-dimensional coherent structures resides within the buffer and the logarithmic layer [4]. From this resulted an early classification of coherent structures, which were limited to wall-bounded low Reynolds number flows, i.e., a scale of size $\mathcal{O}(\delta)$, where $\delta$ is the boundary layer thickness [4].

Later advances revealed the existence of two different scales in turbulent flows. These are LSM and very-large-scale motion (VLSM) of coherent structures [5]. Kim et al. described that VLSM are gathered from small hairpin packets to form long packets that are spatially much longer than the LSM. They found that a bi-modal distribution in the spectrum analysis of velocity fluctuations results in two separate wavelengths that correspond to VLSM and LSM. Since then, VLSM has been investigated in pipe flows [5,6], turbulent flows [7–11], and open channel flows [12–17].

Hydrodynamic forces, in particular drag and lift, acting on a sediment particle in turbulent flows have been extensively studied through experiments [18–27] and numerical simulations [28–34]. Recent investigations applied vortex-detection methods in order to identify the coherent structures that are responsible for the generation of hydrodynamic forces. Chan-Braun et al. [30] reported that streamwise elongated velocity streaks in the buffer-layer are the responsible mechanisms for the correlation between the streamwise velocity fluctuations and drag force. Vowinckel et al. [31] studied the entrainment of a sediment particle over a fixed bed of a square arragement of spheres. They reported the existence of streamwise aligned, counter-rotating structures at the onset of particle entrainment. While these two studies adressed the influence of coherent structures on the hydrodynamic forces of particles, their study was limited to velocity streaks within the buffer layer. Schobesberger et al. [35] performed an experimental investigation of a sediment particle resting on a smooth-wall and identified the passing LSM of coherent structures at the onset of particle entrainment. A complementary numerical study of this experiment, investigating a single sediment particle fully exposed to turbulent open channel flow on a smooth-wall, was performed by Yücesan et al. [34], in the following referred to as the $M2$ case. They found out that vortices that were characterised by their spatial scale (in particular, in the wall-normal direction) to be similar or larger than that of the sediment particle produced a significant simultaneous increase of lift and drag forces, while interactions with small scale coherent structures resulted in negligible changes in hydrodynamic forces.

Early investigations of the drag force while using spectrum analysis reported that low frequency streamwise velocity fluctuations produce a quasi-steady drag force [36]. In addition to that, high frequency fluctuations were found to amplify the nonlinearity due to high order velocity fluctuations in the spectrum curve, which is highly dependant on the exposure level of the particle. Experimental studies of Cameron et al. [15,17] were the first to analyse the effect of VLSM on the drag force of a spherical roughness element. Their premultiplied spectrum analysis of the drag force was characterised with two modes of scales which were low-frequency and high-frequency peaks. Low frequency peaks were characterised by the influence of VLSM, whereas high frequency peaks were addressed to the influence of the pressure field in the vicinity of the particle. Their study also reported that the magnitude of the spectral peaks increases with increasing particle exposure and channel depth. The premultiplied spectrum of the drag force of a fully hidden particle was not affected by the VLSM due to a shielding effect which was also identified by Dwivedi et al. [36]. While Chan-Braun et al. [30] were the first to identify a bi-modal distribution of scales in the spectrum analysis of the drag force, their study evaluated neither VLSM nor the effect of particle exposure.

Lift force is the less understood component of the hydrodynamic forces on a sediment particle compared to the drag force. Recent investigations reported that lift force is poorly correlated with the streamwise and vertical velocities and vertical momentum flux based on the measurements at the upstream side as well as at the top side of the particle [22]. Smart & Habersack [21] reported that pressure difference above and beneath the particle is large enough to entrain the particle. Dwivedi et al. [25] noted that increasing particle exposure resulted in an increase of the skewness of the lift force. Their study also reported co-spectra of the lift force and the flow field. Furthermore, a spectrum analysis of the lift force was reported to exhibit two scaling ranges [37].

Today, our understanding of the interrelation between coherent structures and the drag force has been established through varying particle exposure, auto- and cross-correlation of the flow field, high order statistics and spectrum analysis. However, observations on the lift force acting on the sediment particles were only limited to time series of pressure measurements. Therefore, the effect of LSM and VLSM on the lift force still remains widely unknown. The aim of the present study is to perform numerical simulations in order to analyse the effect of LSM and VLSM on the lift force. The numerical simulation employs two different configurations of a rough boundary, which are denoted as $SP1$ and $SP2$ cases, in order to study the effect of roughness elements on the hydrodynamic forces. A comparison is performed with the aforementioned $M2$ case, in which a particle on a smooth-wall is fully exposed to the flow [34]. Auto and Cross-correlation of the hydrodynamic forces, in particular the lift force, with the flow field has been evaluated. The spectra and the premultiplied spectra of the velocity fluctuations as well as the hydrodynamic forces acting on the particle are presented and discussed.

## 2. Numerical Methods

### *2.1. Domain and Boundary Conditions*

A systematic variation of the exposure level of a spherical sediment particle of fixed size $d = 0.026$ m was performed, placed in an array of spherical roughness elements and exposed to turbulent flow with a high Reynolds number. The numerical simulation consists of two configurations of the bottom wall with different sizes of the roughness elements in a square arrangement. The diameter of the roughness elements in the $SP1$ and $SP2$ cases is characterised as $d/2$ and $d$, respectively. The particles were separated from each other by a distance of $\Delta p = 0.154d$, where $\Delta p$ is the shortest distance between the particles. The ratio of the roughness elements to the channel height is characterised by $d/h = 0.076$ in the $SP1$ case and $d/h = 0.152$ in the $SP2$ case, where $h$ is the channel height. The selection of the particle diameter was based on the entrainment conditions of a single sediment particle exposed to fully developed turbulent open channel flow as described in the experimental study by Schobesberger et al. [35]. The no-slip/no-penetration $u_i = 0$ boundary condition was applied on the sediment particle surface. A schematic is presented in Figure 1 to illustrate the setup of the simulation in the $SP1$ and $SP2$ cases. An open channel flow (OCF) was considered with the dimensions of $0.9 \times 0.171 \times 0.3$ m. The streamwise, wall-normal and spanwise directions in a Cartesian coordinate system were denoted by $x$, $y$ and $z$, respectively. Throughout the manuscript $\langle . \rangle$ indicates time averaging.

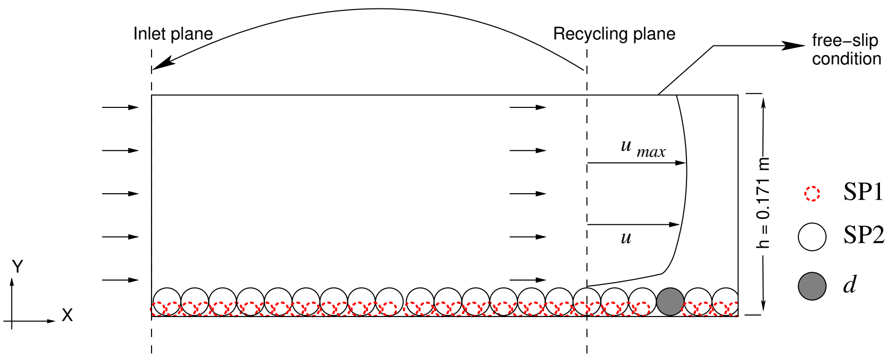


**Figure 1.** Principle sketch of the flow field in the concurrent simulation for the $SP1$ and $SP2$ cases.

A concurrent simulation method was employed to compute a fully developed turbulent open channel velocity profile in the streamwise direction [38,39]. The method uses a plane orthogonal to the flow direction located in the downstream region of the channel to sample the instantaneous velocity and pressure field which is then used as an inlet condition. Therefore, the approach flow in the simulation is characterised as a fully developed rough-wall turbulent open channel velocity profile.

The simulation employed a no-slip/no-penetration $u_i = 0$ boundary condition at the bottom wall, the lateral walls as well as for the roughness elements, $\partial u/\partial y = \partial w/\partial y = 0$, $v = 0$ at the free surface and $\partial u_i/\partial x = 0$ at the outlet, where $u, v$ and $w$ are the streamwise, wall-normal and spanwise velocities, respectively. The outlet is located $\approx$5.8$d$ (or $\approx$7308 $(\nu/u_\tau)$ in viscous units) downstream of the center of volume of the particle. While this is expected to be large enough to avoid any influence of the outlet boundary condition on the hydrodynamic forces acting on the particle, a further downstream extension of the domain would have been desirable, but proved computationally unfeasible. The domain of the simulation was discretized with a fully structured mesh by $24.24 \times 10^6$ and $19.17 \times 10^6$ cells in the $SP1$ and $SP2$ cases, respectively. The boundary layer thickness $\delta$ was calculated based on the maximum mean streamwise velocity $u(y)_{max}$ in the wall-normal direction at the top of the spherical sediment particle. Similarly, the friction velocity $u_\tau$ has been estimated based on the extrapolation of the linear segment of the total stress curve. The streamwise length of the recycling plane was chosen according to the analysis of the two-point correlation (TPC) of velocity fluctuations along the streamwise direction depicted in Figure 2. The correlations were observed to drop to zero $\approx 5d$ away from the inlet for the $SP1$ and $SP2$ cases.

The grid densities near the sediment particle in the present simulations were calculated for the $SP1$ ($s^+ \approx 1$) and $SP2$ ($s^+ \approx 1.2$) cases. Additionally, the position of the first grid node from the wall was set to $y^+ \approx 1.5$ and $y^+ \approx 1.7$ for the $SP1$ and $SP2$ cases, respectively, which is well below ten wall units. Positions of the grid nodes within the domain in all other directions are within 25 wall units. Therefore, the grid resolution is expected to be fine enough to resolve most of the energy within the channel. Details of the simulation parameters, including the $M2$ case [34], are summarized in Table 1.

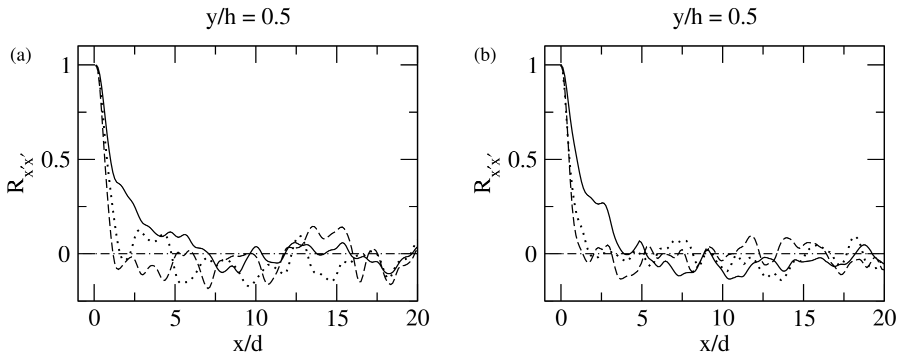


**Figure 2.** TPC of velocity fluctuations ($u'$, $v'$, $w'$ presented with ($-$), ($--$), ($\bullet$), respectively) at the center of the bulk along streamwise ($R_{x'x'}$) direction: (**a**) $SP1$; (**b**) $SP2$ case.

**Table 1.** Simulation parameters: $U_b = \frac{1}{h}\int_0^h \langle u \rangle dy$ is the spatially and temporally averaged bulk velocity, $u_\tau = \sqrt{\langle \tau_w \rangle / \rho}$ the spatially averaged friction velocity at the bottom wall, $Re_b = hU_b/\nu$ is the bulk Reynolds number, $Re_\tau = hu_\tau/\nu$ is the friction Reynolds number, $\delta$ is the boundary layer thickness, $\Delta x^+, \Delta y^+, \Delta z^+$ and $\Delta s^+$ are the grid spacing along streamwise, wall-normal, spanwise and sediment particle in viscous units, respectively, $T^+ = TU_b/h$ is total simulation time in which the statistical information was collected without taking into account turbulent transition.

| Case | $U_b/u_\tau$ | $Re_b$ | $Re_\tau$ | $\delta$ | $\Delta x^+$ | $\Delta y^+$ | $\Delta z^+$ | $\Delta s^+$ | $T^+$ |
|---|---|---|---|---|---|---|---|---|---|
| $M2$ | 23.25 | 71,755 | 3443 | $0.585h$ | 15.5 | 7.7 | 15.5 | 1.9 | 125 |
| $SP1$ | 9.10 | 75,327 | 8284 | $0.666h$ | 16.5 | 1.5 | 16.5 | 1 | 79.3 |
| $SP2$ | 7.42 | 77,096 | 10,373 | $0.737h$ | 24.5 | 1.7 | 24.5 | 1.2 | 94 |

### 2.2. Methodology and Turbulence Statistics

Large Eddy Simulation (LES) of the unsteady Navier-Stokes and continuity equations was performed to compute the incompressible, Eulerian flow field. The numerical setup of the simulation is identical to Yücesan et al. [34]. The OpenFOAM [40] open-source software package has been used for the numerical simulations. Convective terms were discretized using an upwind-biased method, gradient terms by a central differencing scheme. The time derivative was discretized by an implicit backward differencing method. In order to preserve temporal accuracy, the Courant number was kept $\leq$0.5. The accuracy of the numerical schemes in time and space is of second order.

*Water* **2021**, *13*, 248 

The time-averaged velocity field was gathered based on plane-averaged velocity data sampled at $x/d \approx 28.27$. The effective flow height was calculated as $h_{eff} = h - d_{eff}$, where $d_{eff}$ is the artificial position of the wall defined as $d_{eff} = 0.8d/2$ and $d_{eff} = 0.8d$ for the $SP1$ and $SP2$ cases, respectively. Figure 3a depicts the mean streamwise velocity normalized by the bulk velocity. The resulting velocity profiles show that the maximum velocities occurred below the water surface, indicating the presence of secondary currents (SC) in the channel [41]. Secondary currents can be a significant mechanism of delivery of momentum from and towards the channel boundaries if the aspect ratio (width to depth) is lower than a certain value. Despite the influence of the SC in our numerical study, we have omitted their effect as the scope of the present manuscript is not the interrelation between VLSM and SC. The root mean square of velocity fluctuations for the $SP1$ and $SP2$ cases are presented in Figure 3b and compared to the smooth-wall case $M2$. A visualization of the mean velocity magnitude of the flow field is depicted in Figure 4.

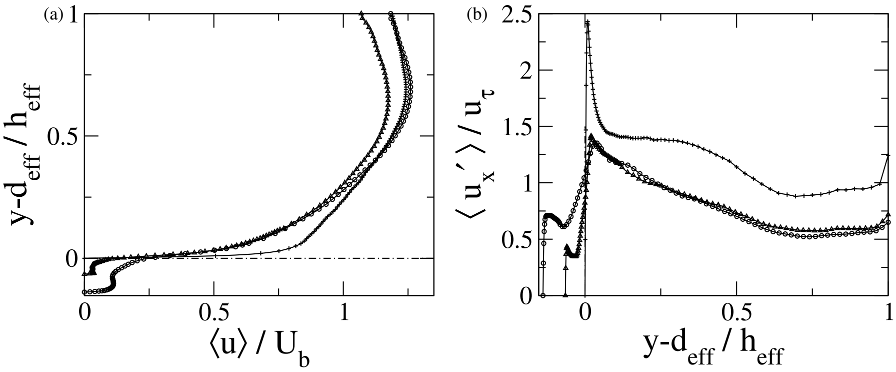


**Figure 3.** Normalized mean streamwise velocity for the $SP1$ ($\triangle$) and $SP2$ ($\circ$) cases, compared to the mean centerline velocity profile for $M2$ ($+$) (**a**); root mean square of velocity fluctuations for the $SP1$ ($\triangle$) and $SP2$ ($\circ$) cases, compared with the smooth-wall case $M2$ ($+$) (**b**).

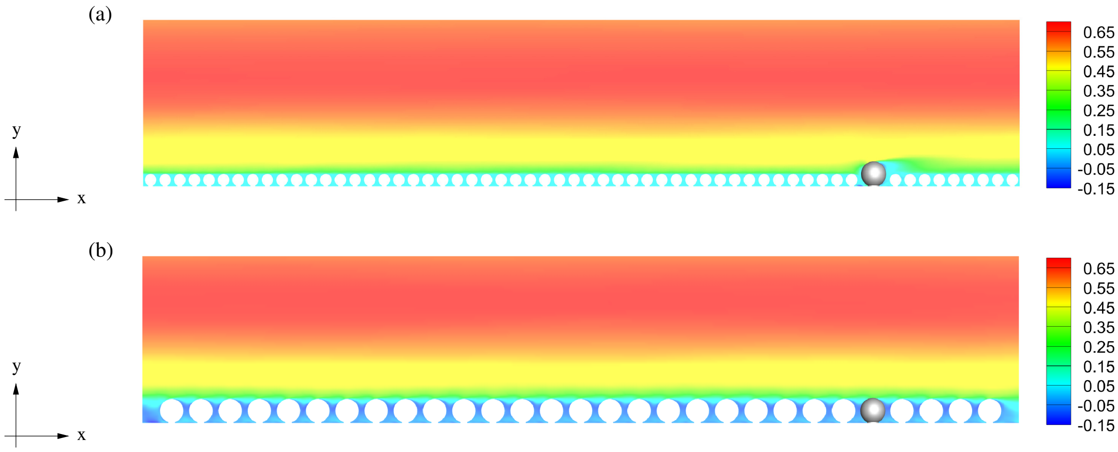


**Figure 4.** Streamwise aligned cross-sectional plane for the $SP1$ (**a**) and $SP2$ (**b**) cases. The mean streamwise velocity of the flow field presented with colour contours.

## 3. Results and Discussion

### 3.1. Hydrodynamic Forces Acting on the Spherical Particle

Hydrodynamic forces acting on the spherical sediment particle are defined, as follows,

$$\boldsymbol{F} = -\int_s p\boldsymbol{n}\, ds + \int_s \boldsymbol{\tau} \cdot \boldsymbol{n}\, ds \tag{1}$$

where $\boldsymbol{F}$ is the total surface force that is acting on the target spherical particle, $\boldsymbol{n}$ is the surface normal vector, $s$ is the surface of the particle, $p$ is the kinematic pressure, and $\boldsymbol{\tau}$ is the stress tensor.

The computation of drag and lift coefficients is based on the hydrodynamic force formulation,

$$F_{\{D,L,Z\}} = \frac{1}{2} U_b^2\, A\, C_{\{D,L,Z\}} \tag{2}$$

where $U_b$ is the bulk velocity, $A = \pi D^2/4$ is the planform reference area of the spherical sediment particle, $F_D$ is the drag force, $F_L$ is the lift force, $F_Z$ is the lateral force, $C_D$ is the drag coefficient, $C_L$ is the lift coefficient, and $C_Z$ is the lateral force coefficient. Table 2 summarizes the statistics of the hydrodynamic forces, including the $M2$ case [34] in order to present the variation of the forces.

**Table 2.** Statistics of forces acting on the stationary sediment particle: $\sigma_D/\langle F_D\rangle$ is the standard deviation of the instantaneous drag force normalized by the mean drag, $\sigma_L/\langle F_L\rangle$ is the standard deviation of the instantaneous lift force normalized by the mean lift, $F_D^+ = \langle F_D\rangle/\rho\nu^2$ is the mean drag force presented in dimensionless form, where $\rho$ is the density of the fluid, $F_L^+ = \langle F_L\rangle/\rho\nu^2$ is the mean lift force presented in dimensionless form, $S_{D,L,Z}$ and $F_{L_{D,L,Z}}$ are the skewness and flatness of the regarding instantaneous forces, respectively.

| Case | $\sigma_D/\langle F_D\rangle$ | $\sigma_L/\langle F_L\rangle$ | $F_D^+$ ($\times 10^{-6}$) | $F_L^+$ ($\times 10^{-6}$) | $S_D$ | $S_L$ | $S_Z$ | $F_{L_D}$ | $F_{L_L}$ | $F_{L_Z}$ |
|---|---|---|---|---|---|---|---|---|---|---|
| $M2$ | 0.094 | 0.284 | 19.5 | 4.98 | 0.138 | 0.119 | 0.037 | 2.624 | 2.91 | 2.899 |
| $SP1$ | 0.347 | 0.47 | 10.3 | 4.1 | 0.441 | 0.262 | −0.016 | 3.315 | 3.361 | 3.321 |
| $SP2$ | 0.912 | 1.15 | 4.22 | 2.49 | 0.002 | 0.462 | −0.249 | 3.399 | 4.134 | 3.723 |

The mean drag coefficients $\langle C_D\rangle$, as shown in Figure 5, corresponding to the $SP1$ and $SP2$ cases, were identified as 0.211 and 0.082, respectively. The increase of the drag coefficient is associated with the exposed area of the particle to turbulent open channel flow. The coefficient of variation of the drag force $\sigma_D/\langle F_D\rangle$ increases with decreasing particle exposure. The $SP2$ case yielded a ratio of 0.912, whereas the $SP1$ case resulted in a significantly lower ratio of 0.347. The standard deviation of the drag force was observed to decrease with increasing particle exposure. However, the rate of change in the drag force is more pronounced than that of the variation of the standard deviation; therefore, the coefficient of variation approached $\approx 1$ for a fully hidden particle in $SP2$. The investigations of Schmeeckle et al. [22] show that the coefficient of variation of the drag force for a fully hidden particle becomes unity, whereas increasing exposure yielded a lower ratio, which is in line with our findings. High order statistics showed that the skewness of the drag is small for the $SP1$ and $SP2$ cases. The flatness of the drag forces exhibits a decrease with increasing exposure level. The half-exposed and fully exposed particles yielded similar flatness coefficients $\approx 0.33$ as compared to the $M2$ case.

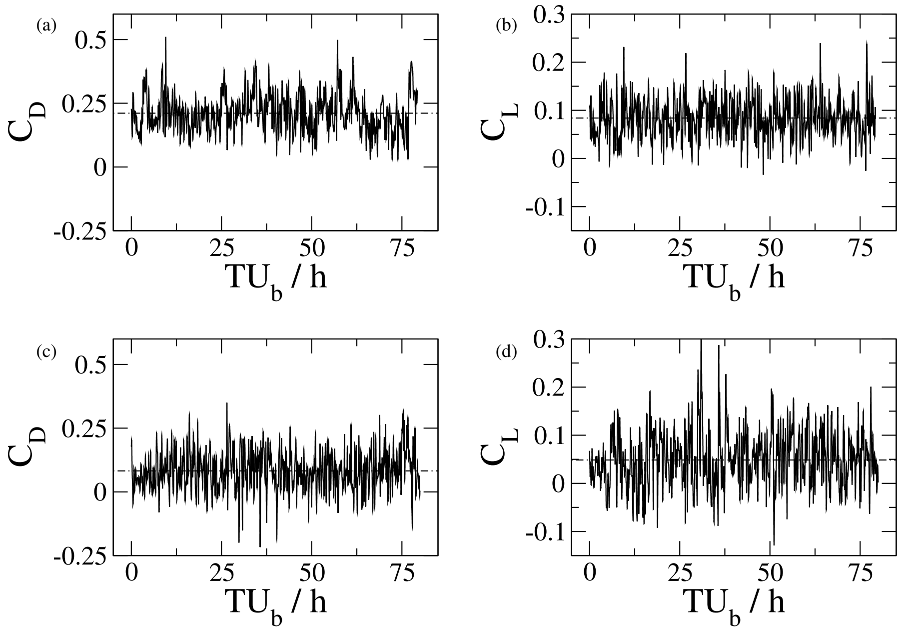


**Figure 5.** Time series of the drag and lift coefficients for the $SP1$ (**a**,**b**) and $SP2$ (**c**,**d**) cases.

Table 2 presents the variation of the mean lift force with respect to the particle exposure. Our results show that the mean lift force increases with increasing particle exposure. However, the standard deviation of the fluctuations of the lift force exhibited a decreasing trend with higher particle exposure. Earlier investigations conducted by Zeng et al. [42] in a low Reynolds number channel flow reported an increase of the lift coefficient with decreasing distance from the smooth-wall. The lift force on a rough boundary with varying elevation level was investigated by Schmeeckle et al. [22], who reported a decrease of the mean lift force with increasing distance of the particle from the bottom wall, simultaneously increasing exposure. Thus, it was observed that a particle residing on the bottom wall without an elevation increase results in an increase of the lift force with rising exposure. On the other hand, only increasing the elevation level with or without roughness elements yields a decrease of the positive pressure force generated at the bottom part of the particle. A possible explanation of this behaviour is that increasing the particle exposure results in an increase of the stagnation pressure at the leading edge, which, in turn, increases the lift force with a higher exposure level. High order statistics (i.e., skewness and flatness) of the lift force exhibit an increasing trend with decreasing exposure. The skewness of the lift force in the $SP2$ case was observed as $F_{L_L} = 0.462$, while increased exposure (i.e., $SP1$) yielded $F_{L_L} = 0.262$. The flatness of the $M2$ case exhibits a nearly Gaussian distribution, whereas the $SP1$ and $SP2$ cases resulted in a higher flatness coefficient.

### 3.2. Auto-Correlation Function of Lift and Drag Forces

Figure 6 shows the Auto-Correlation Functions (ACF) of the hydrodynamic forces on the spherical sediment particle for the $SP1$ and $SP2$ cases. The time lag was normalized with outer scaling.

Auto-correlation of the fluctuations of the drag force was observed to decay faster at a smaller lag with decreasing exposure of the particle. Auto-correlation of the drag in the $SP2$ case drops to the zero axis more rapidly when compared to the half-exposed particle in the $SP1$ case, as visible from Figure 6a. The findings of Yücesan et al. [34] also confirm the decaying trend, as a fully exposed particle exhibits even a higher correlation over a larger lag. A possible explanation of this systematic decaying trend is associated with the streamwise elongated coherent structures, which results in a high auto-correlation over a large lag. A similar finding by Amir et al. [37] concluded that the cross-correlation of two particles positioned along the flow direction with a distance apart is higher with respect to the particles that are positioned spanwise, which is in line with our findings. ACF of the drag force in the $SP2$ case exhibits a local minimum of $-0.083$ at $TU_b/h = 0.3$, whereas the $SP1$ case does not exhibit any local minimum. A possible reason of the local minimum, observed only in the $SP2$ case, was assumed to be the effect of pressure forces, in particular fluctuations of the pressure field near the bottom wall, according to previous studies [37,43].

ACF of the fluctuations of the lift force for the $SP1$ and $SP2$ cases in Figure 6b showed a close promiximity of decay over lag when compared to the auto-correlation of drag forces. Therefore, the auto-correlation of the lift forces is less likely to be influenced by the varying particle exposure in the investigated setup. This explains that streamwise elongated coherent structures do not affect the lift force over a larger lag. In Figure 6b, it can be seen that the $SP1$ case does not result in a local minimum, instead drops to the zero axis at $TU_b/h \approx 0.25$ and fluctuates. A comparison of the auto-correlation between fluctuations of the drag and lift forces in the $SP1$ case indicates that the lift force more rapidly drops to the zero axis, whereas the ACF of the lift force in the $SP2$ case exhibits a drop over a slightly longer time.

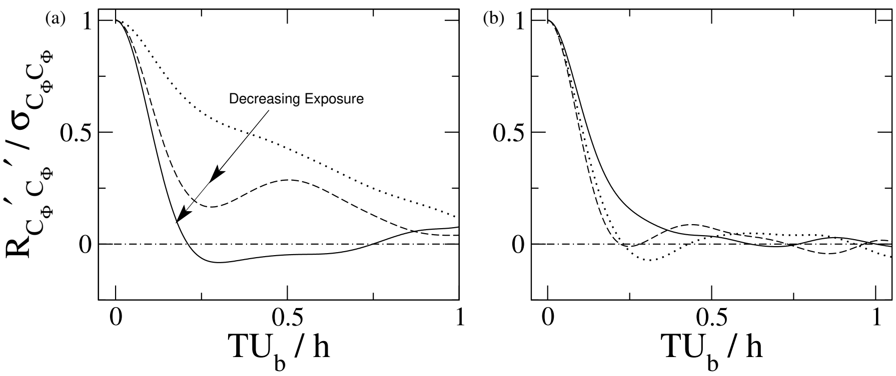


**Figure 6.** Auto-correlation functions of drag (**a**) and lift (**b**) coefficients for the $SP2$ ($-$) and $SP1$ ($--$) cases, when compared with the literature results of the $M2$ case in Yücesan et al. [34] ($\cdots$).

### 3.3. Cross-Correlation Function of Lift and Drag Forces

Cross-correlation functions (CCF) of the drag and lift forces, as well as their correlation with respect to the flow properties, in particular streamwise and wall-normal velocity fluctuations, were analysed in order to understand how flow structures relate to the hydrodynamic forces in the vicinity of the particle. The flow parameters were sampled at two specific locations to assess the influence of the streamwise position on the correlation coefficients. The wall-normal position was kept constant at $y = 1.15d$, whereas two different streamwise positions were selected: at one spherical diameter ($d$) upstream of the particle ($x/d = -1$) and at the top of the particle at ($x/d = 0$).

Figure 7 presents the CCF between drag and lift coefficients of the particle in the $SP1$ and $SP2$ cases and it provides a comparison with respect to the $M2$ case of Yücesan et al. [34]. In general, positive correlation indicates that fluctuations of the drag and lift forces have the same positive sign, whereas the minimum peaks indicate the opposite signs of fluctuating values [32]. Fluctuations of the drag and lift forces for the $SP1$ and $SP2$ cases at zero lag $TU_b/h = 0$ are weakly correlated: $R_{C_D{}'C_L{}'}/\sigma_{C_D}\sigma_{C_L} = (-0.055, -0.042)$. The $SP2$ case exhibits local minimum and maximum correlation coefficients of $(-0.363, 0.249)$ at

*Water* **2021**, *13*, 248 

$TU_b/h = (-0.114, 0.11)$ with a separation time between the local maxima and minima $\Delta TU_b/h = 0.224$, whereas the $SP1$ case results in local maximum and minimum coefficients of $(-0.265, 0.216)$, with a separation time of $\Delta TU_b/h = 0.21$. Therefore, the time lags for which the maximum and minimum peaks are observed, are almost identical in both cases. The $SP2$ case exhibits a slightly higher lag of $\approx +0.014$ between the peak points of its correlation when compared to the $SP1$ case. A possible explanation of this behaviour is that bulk velocity in $SP2$ is higher as compared to the $SP1$ case, thus the wavelength of the correlation in the $SP2$ case is larger. The correlation coefficient of both cases indicates that the $SP2$ case is uncorrelated over a larger lag. However, the half-exposed particle in case $SP1$ results in weak fluctuations of correlation. The amplitude of the negative correlation coefficient is significantly reduced in the $SP1$ case, when compared to $SP2$, as also visible from Figure 7. However, the gap between the maximum positive peaks of the correlation coefficient of these two cases remains less affected with a slightly higher positive correlation of the $SP2$ case. Thus, the fully hidden particle in case $SP2$ results in a higher amplitude of the correlation when compared to the half-exposed particle in $SP1$.

The correlation coefficient between the drag and lift forces in previous studies on a rough-wall [30,32,44,45] was reported to have a local maximum at $\approx (0.23 - 0.55)$, and a local minimum at $\approx -0.5$ for a single particle, which is in line with our findings. A similar investigation [37] studied the correlation of two adjacent particles and a maximum correlation coefficient of 0.115 was reported. The most surprising result reported by [34] is the CCF between fluctuations of the drag and lift forces of a single sediment particle resting on a smooth-wall, which does not exhibit a local minimum, but two maximum peaks, which indicates that drag and lift forces result in a positively fluctuating correlation.

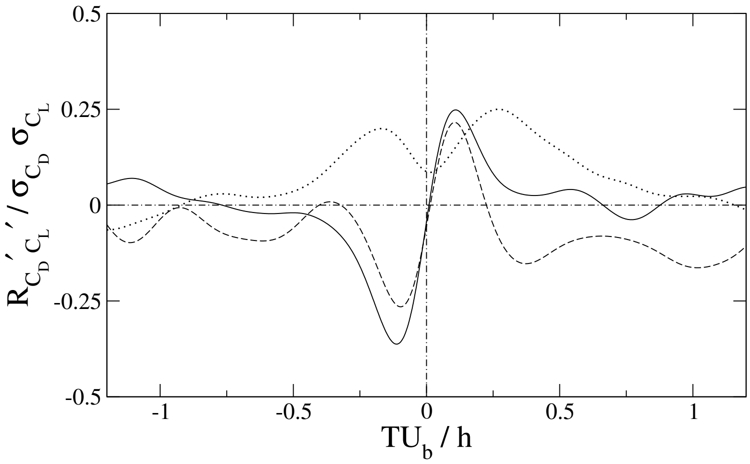


**Figure 7.** Cross-correlation function of the fluctuations of the drag and lift forces for the $SP2$ $(-)$ and $SP1$ $(--)$ cases, compared with the literature results of the $M2$ case in Yücesan et al. [34] $(\cdots)$.

Table 3 provides the minimum and maximum values of the correlation coefficients of the hydrodynamic forces $(C_D, C_L)$ with respect to the flow properties $(u', v')$. The samples of the velocity fluctuations were taken at two separate streamwise positions, in particular one particle diameter upstream $(x/d = -1)$ and at the top of the particle $(x/d = 0)$. Our results show that all of the presented cases exhibit a weak correlation, although the correlation coefficients in the $SP1$ case exhibit slightly more pronounced values when compared to the $SP2$ case. Thus, a correlation of the flow variables and hydrodynamic forces was considered to be neglible, which corresponds to the findings of [22].

**Table 3.** Cross-correlation of the streamwise and wall-normal velocity fluctuations at two separate locations with respect to the hydrodynamic forces.

| | $x/d = -1$ | | | $x/d = 0$ | | |
|---|---|---|---|---|---|---|
| **Case** | $R_{u'C_D'}/\sigma_{u'C_D'}$ | $R_{u'C_L'}/\sigma_{u'C_L'}$ | $R_{v'C_L'}/\sigma_{v'C_L'}$ | $R_{u'C_D'}/\sigma_{u'C_D'}$ | $R_{u'C_L'}/\sigma_{u'C_L'}$ | $R_{v'C_L'}/\sigma_{v'C_L'}$ |
| $SP1$ | (−0.174, 0.234) | (−0.100, 0.117) | (−0.142, 0.090) | (−0.182, 0.241) | (−0.097, 0.104) | (−0.106, 0.097) |
| $SP2$ | (−0.099, 0.110) | (−0.101, 0.078) | (−0.095, 0.095) | (−0.108, 0.106) | (−0.101, 0.068) | (−0.107, 0.086) |

### 3.4. Spectrum Analysis

The power spectrum and premultiplied power spectrum of the streamwise velocity fluctuations as well as fluctuations of the drag and lift forces acting on the sediment particle were computed. The spectrum analysis of the velocity fluctuations was performed based on samples that were taken at the top of the spherical particle $(x/d = 0)$ at a distance $y = 1.15d$ away from the bottom wall. Premultiplied spectra of the streamwise velocity fluctuations are used in order to identify the presence of the very-large-scale motion of the coherent structures and their respective wavelengths. The very-large-scale and large-scale coherent structures are corresponding to low frequency and high frequency fluctuations, respectively. They were identified in many studies in turbulent channel flows [8,9], turbulent pipe flows [5,6], and rough-bed channel flows [14,15,17]. Figure 8 provides a visual impression of the passing vortices in terms of their size and spatial development. Clockwise and counter-clockwise rotating vortices are both extending up to the channel height $(y = h)$.

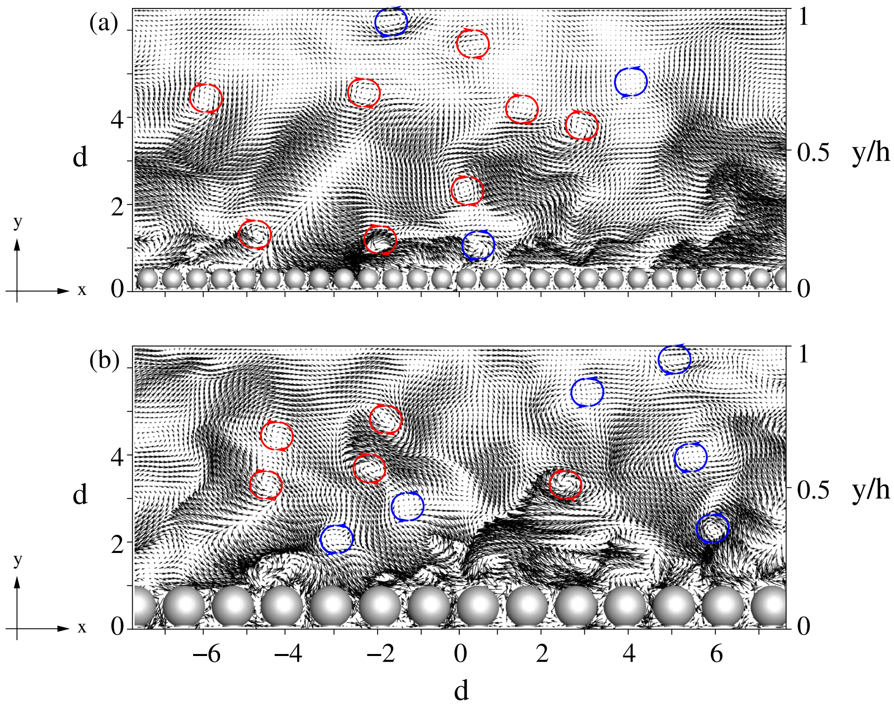


**Figure 8.** Streamwise aligned cross-sectional plane for the $SP1$ (**a**) and $SP2$ (**b**) cases, showing the instantaneous velocity fluctuations. Vortices rotating clockwise (red) and counter-clockwise (blue) are indicated, extending up to the channel height $(y = h)$.

The visualization of the energy spectrum corresponding to the velocity field was performed by applying the discrete Fourier transformation of the whole time-series of the streamwise velocity fluctuations. A windowing operation of the signal was not applied, due to very large size of the time-series, which is constituted of $N$ = 44,721 and $N$ = 61,894 samples for the $SP1$ and $SP2$ cases, respectively. The wave number of the spectra was calculated based on Taylor's frozen turbulence hypothesis of $k_x = 2\pi f / u_{b_{(M2,SP1,SP2)}}$ with the assumption that convection velocity is equal to the mean bulk velocity. Although some studies [5,14] have reported the deficiency of Taylor's hypothesis, the convection velocities that were reported in the literature based on a rough-wall [32,37] were found to be within the range of (0.66–0.72)$U_b$. Therefore, a higher wave number would be expected in the determination of the true wave number than in our assumption. Thus, we consider an underestimated wave number to actually strengthen our results.

Figure 9a–f show the results of the energy spectrum analysis, corresponding to the $M2$, $SP1$, and $SP2$ cases, respectively. Figure 9a,c,e depict the energy spectra of the velocity fluctuations. The trend of the energy spectrum in all cases exhibits a slight increase within the low wave number region until a local maximum was obtained. Despite the high amplitude fluctuations present in the spectra of the signal, a clear trend of the power law ($k^{-1}$) is visible, which separates the low wave number and high wave number regions. Kim et al. [5] interpreted the beginning of the power law $k^{-1}$ region as an indication of the low wave number mode. Based on the beginning of the power law $k^{-1}$, where a maximum local peak occurs in the low wave number region of the $M2$ case, we decided to select $k_x h/2 \approx 0.5$ in order to separate low wave numbers from the high wave number regime. The wave number for which the beginning of the power law occurs in the spectra was observed to decrease with an increasing diameter of the roughness elements. In the $SP1$ case, the beginning of the power law was observed at $k_x h/2 \approx 0.4$, whereas the $SP2$ case resulted in a slightly lower wave number $k_x h/2 \approx 0.3$.

The area under the premultiplied spectrum curve can be interpreted as the corresponding energy levels at specific wave numbers [5]. Therefore, we have presented premultiplied spectra of the velocity fluctuations in Figure 9b,d,f in order to study the energy contents with corresponding wave numbers. A local maximum in the premultiplied spectra in the low wave number range is visible for all of the cases. The energy content of low wave number peaks for the $M2$, $SP1$, and $SP2$ cases resulted in $S_u(k_x h)/2u_\tau^2 = 0.213$, 0.175, and 0.179, respectively. Thus, the results indicate that an increasing particle height in the channel decreases the strength of the VLSM, which may even suppress the evolution of the VLSM of coherent structures due to the presence of a very large roughness height as compared to the boundary layer thickness which influences the logarithmic layer [9]. On the other hand, high wave number fluctuations were observed to decrease with increasing diameter of the roughness elements.

Spectrum and premultiplied spectrum analysis of the drag force was conducted in order to understand the effect of VLSM and LSM of coherent structures on the hydrodynamic forces. The $M2$ and $SP1$ cases resulted in a bi-modal distribution in the premultiplied spectra, as visible in Figure 10. The local maxima within the low wave number range resulted in a significant decrease with increasing roughness element height or decreasing particle exposure, although premultiplied spectra of the velocity fluctuations of the $M2$, $SP1$ and $SP2$ cases exhibited similar local maximum values. Therefore, our findings are in line with previous investigations [14,36]. The influence of the VLSM on the $SP2$ case is negligible. The area under the high wave number premultiplied spectrum curve of the fluctuations of the drag force corresponding to the LSM of the coherent structures was observed to decrease with an increasing roughness element height, although the magnitude of the local maximum was observed to be independant of the protrusion level, wxcept for the $M2$ case. The investigation conducted by Cameron et al. [14] reported that the high wave number peaks are due to the influence of the pressure field in the vicity of the particle. Our results lend to support the same conclusion, because hydrodynamic forces for varying exposure levels showed that the mean drag force decreases with decreasing particle exposure.

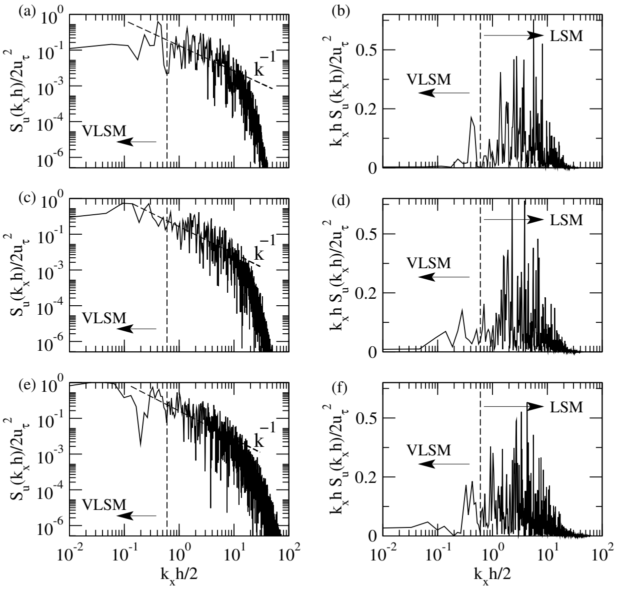


**Figure 9.** Energy spectrum analysis of the velocity fluctuations; (**a**–**f**) correspond to the *M*2, *SP*1 and *SP*2 cases, respectively; (**a**,**c**,**e**) depict energy spectra, whereas (**b**,**d**,**f**) depict the premultiplied energy spectra.

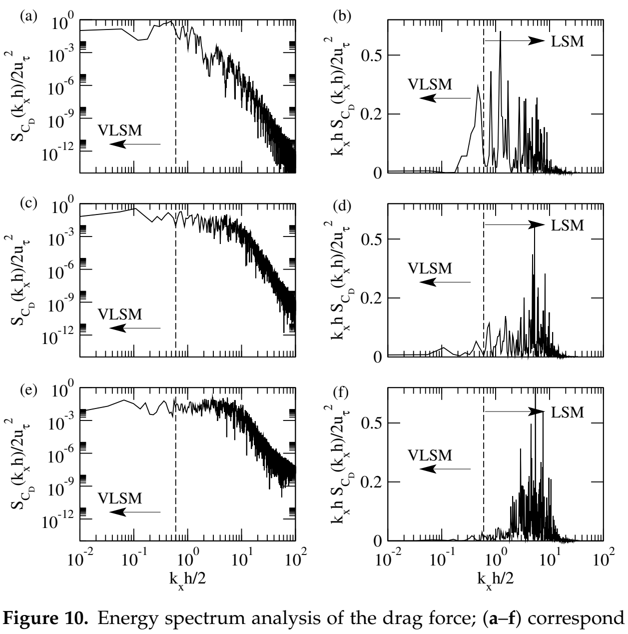


**Figure 10.** Energy spectrum analysis of the drag force; (**a**–**f**) correspond to the *M*2, *SP*1 and *SP*2 cases, respectively; (**a**,**c**,**e**) depict energy spectra, whereas (**b**,**d**,**f**) depict premultiplied energy spectra.

Figure 11 depicts the spectrum of the lift force and its corresponding premultiplied spectrum. The premultiplied spectra of the lift force of the fully exposed particle ($M2$) resulted in a bi-modal distribution, which was similar to the premultiplied spectra of the drag force, exhibiting a weak local maximum within the low wave number region at $k_x h/2 \approx 0.5$. Cases $SP1$ and $SP2$ only exhibited a uni-modal distribution within the low wave number range. The energy contents of the local maximum of the high wave number fluctuations significantly decreased with decreasing particle exposure.

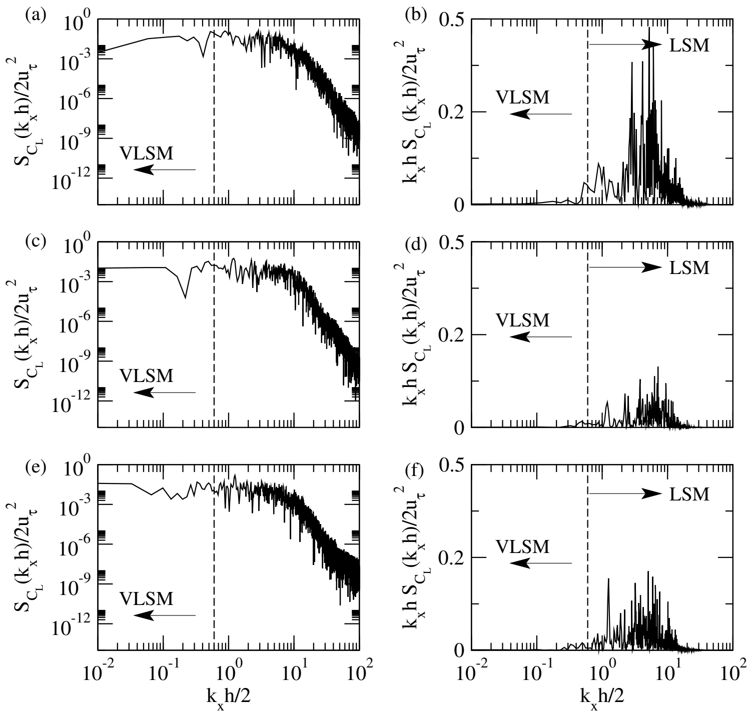


**Figure 11.** Energy spectrum analysis of the lift force; (**a**–**f**) correspond to the $M2$, $SP1$ and $SP2$ cases, respectively; (**a**,**c**,**e**) depict energy spectra, whereas (**b**,**d**,**f**) depict the premultiplied energy spectra.

## 4. Conclusions

Large Eddy Simulation of an open channel flow with two varieties of rough-wall boundary conditions has been carried out. The results were compared to the literature results of Yücesan et al. (2021), *Journal of Hydraulic Research*, for a single sediment particle that was mounted on a smooth-wall in fully developed turbulent open channel flow. Mean drag and lift forces were calculated and it was observed that the hydrodynamic forces decrease in magnitude with decreasing particle exposure, whereas the coefficient of variation increased. Thus, the rate of change in the mean hydrodynamic force is greater than the standard deviation and, consequentially, force fluctuations along the streamwise and wall-normal directions become more significant due to the increasing shielding effect.

The auto-correlation functions of the hydrodynamic forces were investigated and the drag force was observed to decay faster with decreasing particle exposure, while the rate of decay of the auto-correlation function of the lift force was observed to be almost independent of the particle exposure. Correlations between drag and lift forces were computed, and it was found that the cross-correlation function resulted in a higher coefficient for a fully exposed particle when compared to a half-exposed particle.

The premultiplied spectra of the velocity fluctuations were studied for the $M2$, $SP1$, and $SP2$ cases, and two modes of spectral peaks were identified: a low wave number peak indicating the presence of VLSM in the turbulent open channel and a high wave number peak indicating the influence of the LSM of the coherent structures. The local maxima within the low wave number regimes for the rough-wall cases were observed to be smaller in magnitude as compared to the smooth-wall case. Premultiplied spectra of the drag force showed that the fully exposed particle was characterised by a bi-modal shape, which was composed of peaks of a low wave number and high wave number. Similarly, the half-exposed particle exhibited peaks of a weak low wave number and a high wave number. The energy content of the fluctuations of the drag force in the premultiplied spectra were observed to decrease with decreasing exposure, despite that the magnitude of the premultiplied spectral peaks in the $M2$ and $SP1$ cases were determined to be identical. The fully hidden particle in the $SP2$ case was observed to be unaffected by the VLSM, which may be due to the shielding effect that yields no influence on the drag force. Fluctuations of the lift force on a smooth-wall reveal the existence of a weak local maximum within the low wave number region and a high amplitude peak at high wave numbers. Thus, fluctuations of the lift force of a single particle mounted on a smooth-wall were identified to possess a bi-modal distribution. However, this behaviour was not observed for the $SP1$ or $SP2$ cases. These results indicate that VLSM may not have an influence on the lift force of a particle on a rough-wall. The energy content of the premultiplied spectra of the fluctuations of the lift force within the high wave number region exhibits a decreasing trend for the rough-wall cases in comparison to the smooth-wall boundary. The influence of the LSM of the coherent structures gives an explanation for this observation, which may influence the pressure field serving as the responsible mechanism in the vicinity of the particle.

**Author Contributions:** Conceptualization: S.Y., C.H. and M.T.; Data curation: S.Y.; Formal analysis: S.Y.; Funding acquisition: C.H., H.H. and M.T.; Investigation: S.Y.; Methodology: S.Y.; Project administration S.Y., C.S., C.H., H.H. and M.T.; Resources: S.Y., C.S., C.H., H.H. and M.T.; Software: S.Y., P.G.; Supervision: C.H., H.H. and M.T.; Validation: S.Y., D.W., P.G., J.S., C.S., C.H., H.H. and M.T.; Visualization: S.Y.; Writing—original draft: S.Y.; Writing—review & editing: S.Y., D.W., J.S., C.S., C.H., H.H. and M.T.; All authors have read and agreed to the published version of the manuscript.

**Funding:** The financial support by the Christian Doppler Research Association, the Austrian Federal Ministry for Digital and Economic Affairs and the Austrian National Foundation of Research, Technology and Development is gratefully acknowledged.

**Institutional Review Board Statement:** Not applicable.

**Informed Consent Statement:** Not applicable.

**Data Availability Statement:** The data presented in this study are available on request from the corresponding author.

**Acknowledgments:** The computational results presented have been achieved using the Vienna Scientific Cluster (VSC).

**Conflicts of Interest:** The authors declare no conflict of interest. The funders had no role in the design of the study; in the collection, analyses, or interpretation of data; in the writing of the manuscript, or in the decision to publish the results.

## Abbreviations

The following abbreviations are used in this manuscript:

| | |
|---|---|
| LSM | Large-Scale Motion |
| TKE | Turbulent Kinetic Energy |
| VLSM | Very-Large-Scale Motion |

## References


1. Theodorsen, T. Mechanism of turbulence. In Proceedings of the Second Midwestern Conference of Fluid Mechanics, Ohio State University, Columbus, OH, USA, 17–19 March 1952; pp. 1–19.
2. Townsend, A.A. The structure of the turbulent boundary layer. *Math. Proc. Camb. Philos. Soc.* **1951**, *47*, 375–395. [CrossRef]
3. Kline, S.J.; Reynolds, W.C.; Schraub, F.A.; Runstadler, P.W. The structure of turbulent boundary layers. *J. Fluid Mech.* **1967**, *30*, 741–773. [CrossRef]
4. Robinson, S.K. Coherent Motions in the Turbulent Boundary Layer. *Annu. Rev. Fluid Mech.* **1991**, *23*, 601–639. doi:10.1146/annurev.fl.23.010191.003125. [CrossRef]
5. Kim, K.C.; Adrian, R.J. Very large-scale motion in the outer layer. *Phys. Fluids* **1999**, *11*, 417–422. [CrossRef]
6. Guala, M.; Hommema, S.E.; Adrian, R.J. Large-scale and very-large-scale motions in turbulent pipe flow. *J. Fluid Mech.* **2006**, *554*, 521–542. [CrossRef]
7. Christensen, K.T.; Adrian, R.J. Statistical evidence of hairpin vortex packets in wall turbulence. *J. Fluid Mech.* **2001**, *431*, 433–443. [CrossRef]
8. Hutchins, N.; Marusic, I. Evidence of very long meandering features in the logarithmic region of turbulent boundary layers. *J. Fluid Mech.* **2007**, *579*, 1–28. [CrossRef]
9. Jimenez, J.; Del Alamo, J.C.; Flores, O. The large-scale dynamics of near-wall turbulence. *J. Fluid Mech.* **2004**, *505*, 179–199. [CrossRef]
10. Adrian, R.J. Hairpin vortex organization in wall turbulence. *Phys. Fluids* **2007**, *19*, 041301. [CrossRef]
11. Sillero, J.A.; Jiménez, J.; Moser, R.D. Two-point statistics for turbulent boundary layers and channels at Reynolds numbers up to $\delta + \approx 2000$. *Phys. Fluids* **2014**, *26*, 105109. [CrossRef]
12. Zhong, Q.; Li, D.; Chen, Q.; Wang, X. Coherent structures and their interactions in smooth open channel flows. *Environ. Fluid Mech.* **2013**, *15*, 653–672. [CrossRef]
13. Zhong, Q.; Chen, Q.; Wang, H.; Li, D.; Wang, X. Statistical analysis of turbulent super-streamwise vortices based on observations of streaky structures near the free surface in the smooth open channel flow. *Water Resour. Res.* **2016**, *52*, 3563–3578. [CrossRef]
14. Cameron, S.M.; Nikora, V.I.; Stewart, M.T. Very-large-scale motions in rough-bed open-channel flow. *J. Fluid Mech.* **2017**, *814*, 416–429. [CrossRef]
15. Cameron, S.M.; Nikora, V.I.; Marusic, I. Drag forces on a bed particle in open-channel flow: Effects of pressure spatial fluctuations and very-large-scale motions. *J. Fluid Mech.* **2019**, *863*, 494–512. [CrossRef]
16. Wang, G.; Richter, D.H. Two mechanisms of modulation of very-large-scale motions by inertial particles in open channel flow. *J. Fluid Mech.* **2019**, *868*, 538–559. [CrossRef]
17. Cameron, S.M.; Nikora, V.I.; Witz, M.J. Entrainment of sediment particles by very large-scale motions. *J. Fluid Mech.* **2020**, *888*, A7. [CrossRef]
18. Einstein, H.A.; El-Samni, E.S.A. Hydrodynamic forces on a rough wall. *Rev. Mod. Phys.* **1949**, *21*, 520–524. [CrossRef]
19. Coleman, N.L. A theoretical and experimental study of drag and lift forces acting on a sphere resting on a hypothetical streambed. *Int. Assoc. Hydraul. Res. Congr.* **1967**, *3*, 185–192.
20. Hofland, B.; Battjes, J.A.; Booij, R. Measurement of Fluctuating Pressures on Coarse Bed Material. *J. Hydraul. Eng.* **2005**, *131*, 770–781. [CrossRef]
21. Smart, G.; Habersack, H. Pressure fluctuations and gravel entrainment in rivers. *J. Hydraul. Res.* **2007**, *45*, 661–673. [CrossRef]
22. Schmeeckle, M.W.; Nelson, J.M.; Shreve, R.L. Forces on stationary particles in near-bed turbulent flows. *J. Geophys. Res. Earth Surf.* **2007**, *112*. [CrossRef]
23. Diplas, P.; Dancey, C.L.; Celik, A.O.; Valyrakis, M.; Greer, K.; Akar, T. The Role of Impulse on the Initiation of Particle Movement Under Turbulent Flow Conditions. *Science* **2008**, *322*, 717–720. [CrossRef] [PubMed]
24. Celik, A.O.; Diplas, P.; Dancey, C.L.; Valyrakis, M. Impulse and particle dislodgement under turbulent flow conditions. *Phys. Fluids* **2010**, *22*, 046601. [CrossRef]
25. Dwivedi, A.; Melville, B.W.; Shamseldin, A.Y.; Guha, T.K. Analysis of hydrodynamic lift on a bed sediment particle. *J. Geophys. Res. Earth Surf.* **2011**, *116*. [CrossRef]
26. Celik, A.O.; Diplas, P.; Dancey, C.L. Instantaneous turbulent forces and impulse on a rough bed: Implications for initiation of bed material movement. *Water Resour. Res.* **2013**, *49*, 2213–2227. [CrossRef]
27. Dey, S. *Fluvial Hydrodynamics Hydrodynamic and Sediment Transport Phenomena*; Springer Science & Business Media: Berlin/Heidelberg, Germany, 2014.
28. Chan-Braun, C.; García-Villalba, M.; Uhlmann, M. Force and torque acting on particles in a transitionally rough open-channel flow. *J. Fluid Mech.* **2011**, *684*, 441–474. [CrossRef]
29. Lee, H.; Balachandar, S. Critical shear stress for incipient motion of a particle on a rough bed. *J. Geophys. Res. Earth Surf.* **2012**, *117*. [CrossRef]
30. Chan-Braun, C.; García-Villalba, M.; Uhlmann, M. Spatial and temporal scales of force and torque acting on wall-mounted spherical particles in open channel flow. *Phys. Fluids* **2013**, *25*, 075103. [CrossRef]
31. Vowinckel, B.; Jain, R.; Kempe, T.; Fröhlich, J. Entrainment of single particles in a turbulent open-channel flow: A numerical study. *J. Hydraul. Res.* **2016**, *54*, 158–171. [CrossRef]

32. Mazzuoli, M.; Uhlmann, M. Direct numerical simulation of open-channel flow over a fully rough wall at moderate relative submergence. *J. Fluid Mech.* **2017**, *824*, 722–765. [CrossRef]
33. Mazzuoli, M.; Blondeaux, P.; Simeonov, J.; Calantoni, J. Direct Numerical Simulation of Oscillatory Flow Over a Wavy, Rough, and Permeable Bottom. *J. Geophys. Res. Ocean.* **2018**, *123*, 1595–1611. [CrossRef]
34. Yücesan, S.; Schobesberger, J.; Sindelar, C.; Hauer, C.; Habersack, H.; Tritthart, M. Large Eddy Simulation of a Sediment Particle under Entrainment Conditions. *J. Hydraul. Res.* **2021**, Revised.
35. Schobesberger, J.; Lichtneger, P.; Hauer, C.; Habersack, H.; Sindelar, C. Three-Dimensional Coherent Flow Structures during Incipient Particle Motion. *J. Hydraul. Eng.* **2020**, *146*, 04020027. [CrossRef]
36. Dwivedi, A.; Melville, B.W.; Shamseldin, A.Y.; Guha, T.K. Drag force on a sediment particle from point velocity measurements: A spectral approach. *Water Resour. Res.* **2010**, *46*. [CrossRef]
37. Amir, M.; Nikora, V.I.; Stewart, M.T. Pressure forces on sediment particles in turbulent open-channel flow: A laboratory study. *J. Fluid Mech.* **2014**, *757*, 458–497. [CrossRef]
38. De Villiers, E. The Potential of Large Eddy Simulation for the Modeling of Wall Bounded Flows Eugene de Villiers. Ph.D. Thesis, Imperial College London, London, UK, 2006.
39. Montorfano, A.; Piscaglia, F.; Ferrari, G. Inlet boundary conditions for incompressible LES: A comparative study. *Math. Comput. Model.* **2013**, *57*, 1640–1647. [CrossRef]
40. The OpenFOAM Foundation Ltd., UK. 2019. Available online: https://openfoam.org/ (accessed on 1 January 2021).
41. Yang, S.Q.; Tan, S.; Lim, S.Y. Velocity Distribution and Dip-Phenomenon in Smooth Uniform Open Channel Flows. *J. Hydraul. Eng.* **2004**, *130*. [CrossRef]
42. Zeng, L.; Balachandar, S.; Fischer, P. Wall-induced forces on a rigid sphere at finite Reynolds number. *J. Fluid Mech.* **2005**, *536*, 1–25. [CrossRef]
43. Chan-Braun, C. Turbulent Open Channel Flow, Sediment Erosion and Sediment Transport. Ph.D. Thesis, Karlsruhe Institute of Technology, Karlsruhe, Germany, 2012. [CrossRef]
44. Dwivedi, A. Mechanics of Sediment Entrainment. Ph.D. Thesis, University of Auckland, Auckland , New Zealand, 2010.
45. Hofland, B. Rock and Roll: Turbulence-Induced Damage to Granular Bed Protections. Ph.D. Thesis, Delft University of Technology, Delft, The Netherlands, 2005.

## 4.3 Adv. Water Resour. (2022): "LES two-phase modelling of suspended sediment transport using a two-way coupled Euler–Lagrange approach"

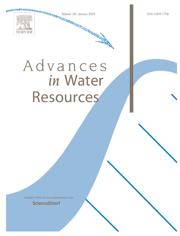


| | |
|---|---|
| Journal: | Advances in Water Resources |
| ISSN: | 0309-1708 |
| Volume: | 160 |
| Issue: | February 2022 |
| Article number: | 104095 |
| DOI: | `https://doi.org/10.1016/j.advwatres.2021.104095` |
| Authors: | Daniel Wildt, Christoph Hauer, Helmut Habersack and Michael Tritthart |
| Submitted: | 9th August 2021 |
| Accepted: | 1st December 2021 |
| Published online: | 31st December 2021 |

Article available open access: `https://www.sciencedirect.com/science/article/pii/S0309170821002463`

Highlights:

- Transient two-way coupled large-eddy simulations of a sediment plume
- Results of 41 simulations indicate three phases of the development of the sediment plume
- Two-way coupling particularly important in the initial sediment acceleration phase
- Significant slowdown of fluid flow primarily in the sediment acceleration phase
- Development of the sediment plume is influenced by particle sorting

Advances in Water Resources 160 (2022) 104095

Contents lists available at ScienceDirect

Advances in Water Resources

journal homepage: www.elsevier.com/locate/advwatres

# LES two-phase modelling of suspended sediment transport using a two-way coupled Euler–Lagrange approach

Daniel Wildt [a,b,*], Christoph Hauer [a,b], Helmut Habersack [b], Michael Tritthart [b]

[a] *Christian Doppler Laboratory for Sediment Research and Management, University of Natural Resources and Life Sciences, Vienna, Muthgasse 107, 1190 Vienna, Austria*

[b] *University of Natural Resources and Life Sciences, Vienna, Department of Water, Atmosphere and Environment, Institute of Hydraulic Engineering and River Research, Muthgasse 107, 1190 Vienna, Austria*

ARTICLE INFO

*Keywords:*
Computational fluid dynamics
Large-eddy simulation
Lagrangian particle tracking
Sediment plume
River

ABSTRACT

Sediment plume development was modelled using an Euler–Lagrangian two-way coupled large eddy simulation. Momentum exchange was calculated based on interaction forces in the Maxey–Riley equation. Validation showed good agreement with experimental data from literature. For analysis of interaction between sediment and fluid 6,859 particles were released into turbulent fluid flow. In order to ensure independence of the results from arbitrary turbulent velocity fluctuations in the initial fluid velocity field, 41 simulations of the test case starting from different initial flow fields were analysed. Results of these simulations are normally distributed. Mean values indicate three phases of the development of the sediment plume: (i) acceleration phase, (ii) transport phase and (iii) deposition phase. Significant slow down of fluid flow and particle sorting turned out to be relevant processes in the initial development of the sediment plume which are not accounted for in one-way coupled models.

## 1. Introduction

Sediment dumping is a frequently applied strategy following dredging operations in rivers (Hauer et al., 2018). However, only little is known about the development of a sediment plume after dumping. Observations in nature show highly dynamic processes in the area where the sediment enters the flow. While some sediment particles remain close to the water surface, others settle to the bottom of the channel (Haimann et al., 2018).

Detailed studies of this process in nature are difficult to realize due to the high spatial and temporal variability. Experiments in the laboratory are limited because of the difficulty of properly scaling sediment particles (Hauer et al., 2018). In addition simultaneous observations of the velocity of water and sediment are difficult to make (Zhong et al., 2014).

Haimann et al. (2018) carried out a detailed study of the development of a sediment plume after dumping of sediment from harbour dredging in Danube River. Their study included on-site monitoring during dumping accompanied by a three-dimensional sediment transport model. They concluded that the behaviour of sediment immediately after it is dumped into the river needs further investigation. Processes of particle–fluid interaction need to be included in respective models.

Based on theoretical considerations as well as physical and numerical models only some of the effects of sediment on turbulent fluid flow have been parametrized. Several studies show the reduction of the von Kármán constant in the logarithmic layer (e.g. Nezu and Azuma, 2004; Ferreira, 2015; Cheng et al., 2018b). The effect of particles on fluid turbulence have been incorporated into turbulence models (Hsu and Liu, 2004; Amoudry, 2014; Kranenburg et al., 2014). Equations for the sediment concentration profile have been developed by Rouse (1939) and Hunt and Inglis (1954).

Computational fluid dynamics provides an efficient way to obtain spatially and temporally highly resolved information about flow processes. During the last decade several studies of sediment transport in fluid flow have been carried out using different numerical modelling approaches. They can be divided into Euler–Euler (e.g. Hsu and Liu, 2004; Amoudry, 2014; Kranenburg et al., 2014; Dallali and Armenio, 2015; Cheng et al., 2017, 2018b), Euler–Lagrangian (e.g. Squires and Eaton, 1990; Vinkovic et al., 2011; Sun et al., 2017; Cheng et al., 2018a; Sun et al., 2018; Elghannay and Tafti, 2018; Ota et al., 2019) and Lagrangian–Lagrangian (e.g. Lobovský and Křena, 2007; Crespo et al.,

* Corresponding author at: University of Natural Resources and Life Sciences, Vienna, Department of Water, Atmosphere and Environment, Institute of Hydraulic Engineering and River Research, Muthgasse 107, 1190 Vienna, Austria.
*E-mail addresses:* daniel.wildt@boku.ac.at (D. Wildt), christoph.hauer@boku.ac.at (C. Hauer), helmut.habersack@boku.ac.at (H. Habersack), michael.tritthart@boku.ac.at (M. Tritthart).

https://doi.org/10.1016/j.advwatres.2021.104095
Received 9 August 2021; Received in revised form 5 November 2021; Accepted 1 December 2021
Available online 31 December 2021

2015; Canelas et al., 2016, 2017; Pahar and Dhar, 2017), based on the field theory used for fluid and particles, respectively.

Particle–fluid interaction is described in detail by the Maxey–Riley equations (Maxey and Riley, 1983). The equation describes forces relevant for particle–fluid momentum exchange: (i) lift and drag force, (ii) added mass force and (iii) Basset history forces. For general flows the Basset history term is difficult to implement, as it includes the storage of a large number of time steps. For this reason it is usually neglected, despite Prasath et al. (2019) showed the importance of the Basset integral in the solution.

Models in literature have implemented momentum coupling in different detail. The most basic method is the single-phase approach in which sediment transport is modelled using an advection–diffusion equation (one-way coupling). This has been extended by Dallali and Armenio (2015) who accounted for the excess density due to sediment concentration through a buoyancy term in the momentum equation. Their analysis shows that this approach enables more accurate results than the classical single-phase approach while still solving the momentum equation for the ambient phase only.

The complete two-phase Euler–Euler equations are, among others, solved in the model `SedFoam` developed by Cheng et al. (2017). Added mass force, lift force and basset forces were neglected in the model. A 3D validation of the model has been carried out by large eddy simulation (Cheng et al., 2018b).

Models using Lagrangian particle tracking for the dispersed phase allow studying the trajectory of individual particles. Turbulent particle dispersion can be accounted for through an eddy interaction model in which random velocities are added to the particle velocities (Cheng et al., 2018a). Sun et al. (2017) extended Lagrangian particle tracking to capture rotational in addition to translational motion. A set of common grain shapes was represented by bonded spheres.

Particle-turbulence interaction in steady-state fluid flow has been studied using direct numerical simulations. Squires and Eaton (1990) used a two-way coupled Euler–Lagrangian model to study both, the effect of particle loading of different grain sizes on the turbulence and vice-versa. Vinkovic et al. (2011) one-way coupled direct numerical simulation (DNS) of fluid dynamics with Lagrangian particle tracking for steady state suspended sediment transport. Their main focus was on the interaction of wall-near turbulence structures and particles. In both studies particles were distributed over the entire cross section of the channel. Thus it is difficult to draw conclusions on the development of a spatially confined sediment plume from their results.

Incorporating the effects of sediment on fluid turbulence in a single-phase model Hsu and Liu (2004) achieved concentration profiles for sheet flow similar to those that could be achieved with a two-phase model. Furthermore also respective results of two-phase Euler–Euler models could be improved including the effects of the presence of sediment particles on fluid turbulence (Amoudry, 2014; Kranenburg et al., 2014). Despite the improvements of turbulence models, particle fluid interactions are still modelled using highly empirical parametrizations and are very sensitive to model coefficients. Thus it is expected that turbulence-resolving modelling approaches are still the best option for detailed studies on sediment transport.

Particle–fluid velocity differences were experimentally studied by e.g. Greimann et al. (1999), Nezu and Azuma (2004) and Muste et al. (2005) as well as numerically by Zhong et al. (2014). Nezu and Azuma (2004) and Muste et al. (2005) carried out velocity measurements of particle laden turbulent fluid flow in a laboratory channel. Amongst others, they discussed the velocity difference between particles and fluid as well as turbulence modulation of particles. Turbulence intensities in the wall-near region were enhanced by the presence of particles. In the outer flow region no influence of particles on turbulence intensities has been observed by Nezu and Azuma (2004). This indicates that a detail model for sediment–fluid interaction is particularly important in areas of unsteady and non-uniform flow.

While a large number of studies dealing with steady sediment transport exist, only a limited number of investigations of the transient transport of an individual sediment plume could be found in literature. So far the flow of sediment suspensions has mainly been studied on the basis of time-averaged profiles of velocities and concentrations (e.g. Zhong et al., 2011, 2014; Cheng et al., 2018b,a). Thus the respective evaluations are limited to such conditions.

Gravity currents (e.g. De Cesare et al., 2001; Necker et al., 2002; Lavelli et al., 2002; La Rocca et al., 2008; An et al., 2012; Hillebrand et al., 2017) as well as test cases such as the failure of a column made of glass beads and dambreak cases (e.g. Pahar and Dhar, 2017) did include the unsteady movement of solid particles. However the surrounding fluid did not have a superimposed velocity as in dumping situations. Liu et al. (2018) study the saltation process of one individual particle using a LES-DEM model. No study investigating the development of a sediment plume in turbulent clear water flow could be found in literature.

In the present study a large eddy simulation of the development of a sediment plume released into fully developed turbulent fluid flow is investigated. The applied numerical model uses Euler–Lagrangian two-way coupling for fluid–solid momentum exchange and a stress term to account for particle–particle interactions. The results of the analysis should provide more detailed insights into the processes after dumping of sediment into a river. The focus is on the portion of particles which are immediately taken up by the flow and do not settle to the bottom at the dumping site. In order to study particle sorting processes, different particle sizes are used, covering Stokes numbers in the range of 0.18 to 19. The model is solved using the open-source package OpenFOAM (Greenshields, 2018). Verification and validation of the model are carried out using literature data from settling experiments in moving water.

## 2. Methods

### 2.1. Governing equations

#### 2.1.1. Fluid flow

Fluid flow is governed by the incompressible, three-dimensional Navier–Stokes equations representing conservation of mass (1) and momentum (2). Momentum exchange between particles and fluid is accounted for through a source term in the momentum equations representing the interface momentum transfer $\boldsymbol{F}$ (Andrews and O'Rourke, 1996).

$$\frac{\partial \alpha}{\partial t} + \nabla \cdot (\alpha \boldsymbol{u}) = 0 \tag{1}$$

$$\frac{\partial \alpha \boldsymbol{u}}{\partial t} + \nabla \cdot (\alpha \boldsymbol{u}\boldsymbol{u}) = \nabla \cdot \left(\nu_{\mathrm{eff}} \nabla \cdot \boldsymbol{u}\right) + \frac{1}{\rho} \cdot \nabla p + \frac{\boldsymbol{F}}{\rho} \tag{2}$$

$\alpha$ represents the volumetric fraction of water in a cell, $\rho$ the density of water, $\boldsymbol{u}$ the fluid velocity, $p$ the pressure and $\nu_{\mathrm{eff}}$ the effective viscosity (see Eq. (4)). For the derivation of the interface momentum transfer $\boldsymbol{F}$ see below and Eq. (8).

Subgrid-scale turbulence is modelled using the Smagorinsky turbulence model (Smagorinsky, 1963).

$$\nu_{\mathrm{sgs}} = C_k \sqrt{\frac{C_k}{C_\epsilon}} \Delta^2 |\bar{D}| \qquad \text{with :} \quad |\bar{D}| = \left(2\bar{D} : \bar{D}\right)^{\frac{1}{2}} \tag{3}$$

$$\nu_{\mathrm{eff}} = \nu + \nu_{\mathrm{sgs}} \tag{4}$$

The : operator denotes a double inner product.

Smagorinsky model constants are set to $C_k = 0.02$ and $C_\epsilon = 1.05$. These values have been obtained by Yücesan et al. (2021) in a parametric analysis using a similar simulation set-up. They agree with the findings of Lysenko et al. (2012). $\Delta$ is the filter length and $\bar{D}$ the deformation rate of the resolved large scale field Ferziger and Perić (2002). The kinematic viscosity $\nu$ is defined along with the fluid properties in Section 2.2.1.

*2.1.2. Particle transport*

Euler–Lagrangian two-way coupling is accomplished using the Multiphase Particle-In-Cell (MP-PIC) method. This algorithm combines the advantages of Lagrangian particle tracking and continuum Euler methods (Andrews and O'Rourke, 1996).

The particle volume fraction $\Theta$ is calculated from the particle distribution function $f$ (Andrews and O'Rourke, 1996).

$$\Theta = \iint f \frac{m}{\rho_s} \, \mathrm{d}m\boldsymbol{v} \tag{5}$$

with

$$\alpha + \Theta = 1, \tag{6}$$

$m$ is the particle mass and $\rho_s$ is the particle density.

Transport of the particle distribution function $f$ is governed by

$$\frac{\partial f}{\partial t} + \nabla_{\boldsymbol{x}} \cdot (f\boldsymbol{v}) + \nabla_{\boldsymbol{v}} \cdot \left(f \frac{\mathrm{d}\boldsymbol{v}}{\mathrm{d}t}\right) = \left(\frac{\partial f}{\partial t}\right)_{\mathrm{coll}} \tag{7}$$

where $\boldsymbol{x}$ is the particle position and $\boldsymbol{v}$ particle velocity (Andrews and O'Rourke, 1996; Snider, 2001). The source term on the right hand side of Eq. (7) is the return-to-isotropy term (O'Rourke and Snider, 2012) which is part of the particle–particle interaction model described at the end of this section.

Particle acceleration $\frac{\mathrm{d}\boldsymbol{v}}{\mathrm{d}t}$ is calculated from the forces acting on the particle using Newtons' law of motion (Fernandes et al., 2018; Cheng et al., 2018a).

$$m\frac{d\boldsymbol{v}}{\mathrm{d}t} = \sum \boldsymbol{F}_i \tag{8}$$

The forces $\boldsymbol{F}_i$ in unsteady particle–fluid momentum exchange are described in the Maxey–Riley equation (Maxey and Riley, 1983). The present model includes drag force $\boldsymbol{F}_D$, lift force $\boldsymbol{F}_L$, added mass force $\boldsymbol{f}_{am}$, pressure force, gravity and inter-particle stress $\tau$.

$$\frac{\mathrm{d}\boldsymbol{v}}{\mathrm{d}t} = \boldsymbol{F}_D + \boldsymbol{F}_L + \boldsymbol{f}_{am} - \frac{1}{\rho_s}\nabla p + \boldsymbol{g} - \frac{1}{\Theta\rho_s}\nabla\tau \tag{9}$$

Drag force $\boldsymbol{F}_D$ is calculated using the following approach:

$$\boldsymbol{F}_D = C_d \cdot \frac{\rho}{\rho_s} \cdot |\boldsymbol{u} - \boldsymbol{v}| \cdot (\boldsymbol{u} - \boldsymbol{v}) \tag{10}$$

The drag coefficient $C_d$ is calculated using an approach for non-spherical particles presented by (Haider and Levenspiel, 1989).

$$C_d = \frac{24}{Re_p} \cdot \left(1 + e^{2.3288-6.4581\phi+2.4486\phi^2} \cdot Re_p^{0.0964+0.5565\phi}\right) + \frac{Re_p \cdot e^{4.905-13.8944\phi+18.4222\phi^2-10.2599\phi^3}}{Re_p + e^{1.4681+12.2584\phi-20.7322\phi^2+15.8855\phi^3}} \tag{11}$$

$Re_p$ is the particle Reynolds number based on the diameter of an equivalent spherical particle and the terminal velocity of the particle in the fluid. The shape factor representing the ratio between the surface area of a spherical particle with the same volume as the non-spherical particle and the surface area of the actual particle is set to $\phi = 0.45$. This is the value which resulted from an analysis of particles by Worf et al. (2019). Results of these experiments will be used in this study for validation.

Lift force $\boldsymbol{F}_L$ and lift coefficient $C_l$ are estimated using the following equations by (Saffman, 1965).

$$\boldsymbol{F}_L = \frac{m_s}{\rho_s} \cdot \rho \cdot C_l \cdot (\boldsymbol{u} - \boldsymbol{v}) \times \frac{\nabla \times \boldsymbol{u}}{|\nabla \times \boldsymbol{u}|^{0.5}} \tag{12}$$

$$C_l = \frac{3}{2\pi\sqrt{\frac{|\nabla\times\boldsymbol{u}|\cdot d^2}{\nu}}} \cdot 6.46 \cdot 0.0524 \cdot \sqrt{0.5 \cdot \frac{|\nabla \times \boldsymbol{u}| \cdot d^2}{\nu}} \tag{13}$$

Added mass force $\boldsymbol{f}_{am}$ for each particle $i$ is calculated as:

$$\boldsymbol{f}_{\mathrm{am},i} = C_{\mathrm{am}}\rho V_{p,i} \cdot \left(\frac{\mathrm{D}\boldsymbol{u}}{\mathrm{D}t} - \frac{\mathrm{d}\boldsymbol{v}_i}{\mathrm{d}t}\right) \tag{14}$$

using $C_{\mathrm{am}} = 0.5$ for the added mass coefficient as it is commonly used in literature (e.g. Sun et al., 2017).

Basset history forces additionally included in the Maxey–Riley equation (Maxey and Riley, 1983) are not accounted for in the presented model. Although its relative importance needs more investigation, it is generally expected to be low. Hence those forces have also been ignored in similar models by other authors (e.g. Sun et al., 2017; Cheng et al., 2018b,a). Particularly when the relative acceleration between particles and fluid is small it is not expected that the Basset history forces play a crucial role.

Small particle sizes involved in the model in this study make the calculation of collision forces of individual particle pairs (e.g. Cundall and Strack, 1979; Tsuji et al., 1992) impractical. Thus particle properties are mapped to an Eulerian grid to compute a stress tensor $\tau$ based on kinetic theories for granular flow by (Lun et al., 1984; Snider, 2001).

$$\tau = \left(\Theta\rho_s + \Theta^2\rho_s(1+\gamma)g_0\right)\Phi \tag{15}$$

The coefficient of restitution is $\gamma = 0.80$ which is slightly less than the value measured by Durda et al. (2011) for 1 m diameter granite spheres.

The radial distribution function $g_0$ is defined as (Snider, 2001):

$$g_0 = \frac{3}{5}\left(1 - \left(\frac{\Theta}{\Theta_{\mathrm{cp}}}\right)^{\frac{1}{3}}\right)^{-1} \tag{16}$$

The volume fraction at close packing is set to $\Theta_{\mathrm{cp}} = 0.65$. Granular temperature $\Phi$ in Eq. (15) is calculated from the time average of the squared differences of the instantaneous and the hydrodynamic particle velocity $C$ (Snider, 2001):

$$\Phi = \frac{1}{3} \cdot \langle C^2 \rangle \tag{17}$$

Off-centre particle collisions bring about isotropic particle distributions (O'Rourke and Snider, 2012). This is accounted for in the model by adding the return-to-isotropy source term $\left(\frac{\partial f}{\partial t}\right)_{\mathrm{coll}}$ developed by O'Rourke and Snider (2012) to Eq. (7). This term causes the particles to scatter due to collisions away from the direction of their original velocities and drives their velocities towards an isotropic Gaussian distribution.

*2.2. Simulation set-up*

*2.2.1. Flow domain and boundary conditions*

Flow depth in the channel is set to $\delta = 0.17$ m. This is approximately the water depth used in the experiments by Worf et al. (2019) of which results will be used for validation. Streamwise and lateral extents of the channel are chosen large enough that all relevant turbulence structures are included. $l_x = 2\pi\delta \approx 1.25$ m for channel length and $l_z = \pi\delta \approx 0.55$ m for channel width are commonly accepted for smooth bed flows (Bomminayuni and Stoesser (2011), see Fig. 1 for a longitudinal section).

Cyclic boundary conditions are applied to inlet and outlet as well as to the lateral walls. A no-slip boundary condition is applied for the bottom wall and symmetry for the free-surface.

Turbulent fluid flow is initially generated in a single-phase simulation. Starting from an initial flow field with a bulk velocity of $\bar{u} = 0.5\,\mathrm{m\,s^{-1}}$ and random velocity fluctuations the flow is recycled through the domain for 120 flow-through times (300 s). A constant bulk velocity is maintained through a momentum source implemented by adopting the pressure gradient. This simulation for creating the initial turbulent flow field is referred to as precursor simulation. Flow fields from the precursor simulation results are stored from $t = 300$ s onwards in regular intervals of 0.04 flow-through times to be used as initial conditions for the test case. In addition those results are used for comparison with flow fields of the sediment plume.

Fluid properties are those of water with a kinematic viscosity of $\nu = 1.17 \times 10^{-6}\,\mathrm{m^2\,s^{-1}}$ and density $\rho = 1000\,\mathrm{kg\,m^{-3}}$. Based on a bulk

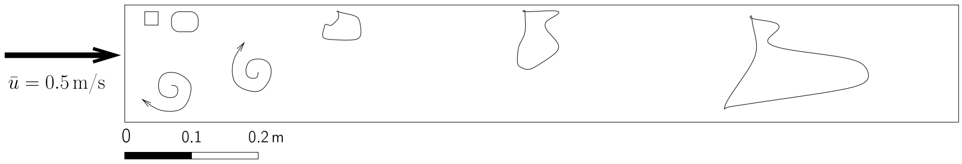


**Fig. 1.** Scheme of the simulation set-up: 6859 particles are released from a 2 cm edge-length, cube-shaped area into turbulent channel flow with a bulk velocity of $0.5\,\mathrm{m\,s^{-1}}$. The trajectory of each individual particle is calculated using the MP-PIC approach. In addition to the initial particle position, exemplary positions and shapes of the sediment plume are shown for four time steps.

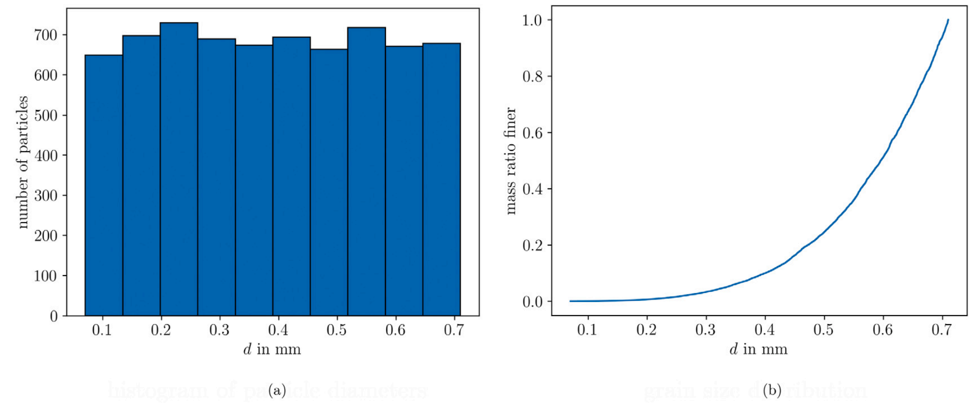


**Fig. 2.** Grain size distribution in the simulations of the test case. (a) histogram of particle diameters; (b) cumulative ratio of particle mass by particle diameter.

fluid velocity of $0.5\,\mathrm{m\,s^{-1}}$ and a channel height of $0.17\,\mathrm{m}$ the Reynolds number of the flow is $Re = 72\,650$.

Simulations are carried out with particles sizes uniformly distributed in the range of $0.07\,\mathrm{mm}$ to $0.71\,\mathrm{mm}$ (see Fig. 2). This corresponds to a non-dimensional grain size of $d^+ = 1.13$ and $d^+ = 11.4$ respectively, where $d^+$ is defined by e.g. Nezu and Azuma (2004) and Dallali and Armenio (2015) by the following equation:

$$d^+ = \frac{u_* d}{\nu} \tag{18}$$

Shear velocity $u_*$ is calculated from the wall shear stress which is determined by extrapolating the linear part of the Reynolds shear stress profile (see Section 3.1.1).

The particle Stokes number $St$ characterizes the ratio of the particle response time $\tau_p$ to fluid solicitation $\tau_f$ (Elghobashi, 1994; Vinkovic et al., 2011).

$$St = \frac{\tau_p}{\tau_f} \tag{19}$$

$$\text{with}: \qquad \tau_p = \frac{\rho_s d^2}{18 \rho \nu} \qquad \tau_f = \frac{\nu}{u_*^2} \tag{20}$$

For the particle diameters used in the model in this study the particle Stokes number ranges from 0.183 to 18.8.

#### 2.2.2. Sediment plume

Verification and validation of the model has been carried out, reproducing the experiments by Worf et al. (2019). Three measuring spoons ($\equiv 3 \cdot 0.24\,\mathrm{ml}$) of sediment of different grain fractions were introduced into turbulent channel flow through a pipe over a time of approximately 1 s. Sediment density was $2650\,\mathrm{kg\,m^{-3}}$ and the shape factor 0.45.

Fall velocities were obtained from the experiments by Worf et al. (2019) based on the slope of the regression line through the $(x, y)$-positions of the particles multiplied with the fluid velocity. $x$ is the flow direction of the fluid. Acceleration due to gravity is acting in negative $y$ direction.

The setup of the test case for studying the development of the sediment plume is similar to the validation case described above. The main difference is that particles are not continuously released over a certain period of time. 6859 particles are placed in a $l_0 = 2\,\mathrm{cm}$ edge length grid ($19 \times 19 \times 19$) in the upper area of the channel close to the inlet (see Fig. 1). This corresponds to an initial volumetric particle concentration of approximately 4.4 %. Particle properties are the same as in the validation cases.

### 2.3. Discretization and numerical solution

The governing equations described in Section 2.1 are discretized in space on a structured mesh with about 5.5 Million cells ($350 \times 106 \times 150$). This corresponds to a dimensionless cell size of $\Delta x^+ = \frac{\Delta x u_*}{\nu} \approx 60$ and $\Delta z^+ = \frac{\Delta z u_*}{\nu} \approx 60$ in streamwise and lateral direction, respectively. The mesh is refined towards the bottom wall (no-slip boundary condition) so that the boundary cell height is approximately $\Delta y^+ = \frac{\Delta y u_*}{\nu} = 1.6$. Wall-adjacent cell centres are at $y^+ = 0.78$ on average. Pressure coupling is accomplished by the PISO algorithm (pressure-implicit split operator).

Grid resolution in streamwise and lateral direction is evaluated based on two-point correlations of turbulent velocity fluctuations $B_{uu}(x)$ calculated from the instantaneous velocity samples by the following equation (Davidson, 2009):

$$B_{uu}(x) = \langle u'(x) \cdot u'(x - \hat{x}) \rangle \tag{21}$$

The model is solved using solvers of the package OpenFOAM 6 (Greenshields, 2018). `pisoFoam` is used for the model of fluid flow for initializing the flow field. An adopted version of `MPPICFoam`, neglecting hydrostatic pressure for the Eulerian phase, is used for the two-way coupled Euler–Lagrange model of fluid and particles.

A second order implicit scheme is used for time discretization. The time step is 0.5 ms which corresponds to a maximum Courant number of approximately 0.27. Advection of velocity is discretized using standard Gaussian finite volume integration with second order central differences interpolation (Greenshields, 2018).

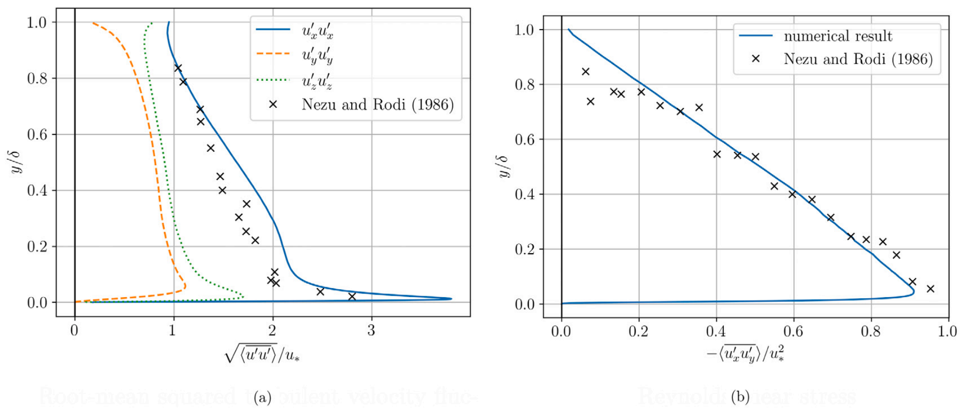


**Fig. 3.** Turbulence intensities (a) and Reynolds shear stress (b) in the precursor simulation spatially averaged in lateral direction.

### 2.4. Result evaluation

In order to analyse the influence of instantaneous turbulent velocity fluctuations, a total of 41 simulations using the same simulation setup and boundary conditions are carried out. Each of these simulations is started from a new initial flow field retrieved from the precursor simulation (see above). The results used as initial conditions for the test case cover a period of 16 flow-through times. After verifying normal distribution of the results of the 41 simulations further evaluation is done based on mean values.

Precursor simulation results are also used for the comparison of the flow field of clear water flow with the flow field around the sediment plume at corresponding time steps. This allows to directly observe the influence of the particles in each individual cell of the flow field.

Influence of sediment on fluid-flow is analysed based on differences between instantaneous fluid velocities in cells with particles present and time averaged fluid velocities of clear water flow in the respective cells from the precursor simulation. A one-sample Student t-test is used to test significance of the velocity difference averaged over all particles for each time step.

Development of the shape of the sediment plume is analysed on the basis of the dimensions of the bounding box enclosing the sediment particles for each time step. Preliminary tests showed that the shape of the sediment plume is quite sensitive to individual particles. With 2.5 % or more of the particles on the extreme ends of the sediment plume excluded from this evaluation, the qualitative results remain constant. Hence in order for this analysis to be less sensitive to individual particles separated from the core of the plume, 2.5 % of the particles on the extreme ends in each direction are not included in this analysis.

## 3. Results and discussion

### 3.1. Verification and validation

#### 3.1.1. Turbulent fluid flow

Validation of turbulent fluid flow is carried out based on spatial and temporal averages of velocity fluctuations (Fig. 3) and velocities (Fig. 4). Time averages are calculated from 14 200 instantaneous velocity samples which were collected from a $x$-normal sampling plane at $x = 1.0\,\mathrm{m}$ in regular intervals over a period of 56.8 flow-through times. Time averages are denoted by $\langle\cdot\rangle$ and spatial averages by $\bar{\cdot}$.

Fig. 3a displays root-mean squared turbulent velocity fluctuations normalized by the shear velocity $u_*$. These turbulence intensities normalized by the shear velocity are slightly over predicted by the model with respect to the experimental data by Nezu and Rodi (1986) particularly in the lower half of the channel. The reason for this is expected to be the relatively low shear velocity in the model (see below).

Fig. 3b displays spatial and temporal averages of Reynolds shear stress normalized by the square of the shear velocity $-\frac{\langle \overline{u'_x u'_y} \rangle}{u_*}$. Reynolds shear stress is 0 at the bottom wall and steeply increases in the viscous sublayer and the buffer layer. Above the peak Reynolds shear stress decreases linearly to 0 at the free surface which is consistent with theory (Pope, 2000; Dey, 2014). A comparison of the Reynolds stress profile with experimental data from literature (Nezu and Rodi, 1986) shows good agreement.

The extrapolation of the linear part of the Reynolds shear stress profile to the channel bed yields a wall shear stress of $\frac{\tau_w}{\rho} = 3.5476 \times 10^{-4}\,\mathrm{m^2\,s^{-2}}$. Thus the shear velocity is $u_* = \sqrt{\frac{\tau_w}{\rho}} = 0.018\,835\,\mathrm{m\,s^{-1}}$ and the shear Reynolds number $Re_* = 2737$.

Spatial and temporal averages of non-dimensional streamwise fluid velocities $u^+$ are plotted against channel height in Fig. 4a. Velocity is zero at the bottom wall and increases in wall-normal direction following a logarithmic curve.

Fig. 4b displays the normalized velocity profile $u^+$ together with a theoretical curve based on the velocity-defect law (Guo, 2017).

$$u^+_{\max} - u^+ = \frac{1}{\kappa} \ln\left(\frac{1}{2B_0\eta\,(2-\eta)} - \frac{1}{2B_0} + 1\right) \tag{22}$$

The von Kármán constant in Eq. (22) is $\kappa = 0.39$ and $B_0 = 0.2$ according to Guo (2017). $\eta = \frac{y}{\delta}$ is the normalized wall-normal coordinate. Maximum non-dimensional streamwise velocity $u^+_{\max} = 29.3$ is determined from the simulation results in Fig. 4a.

Despite the velocity profile in Fig. 4 being consistent with the velocity-defect law (22), streamwise velocities are slightly higher than respective experimental results by Nezu and Rodi (1986). At the same time velocities are relatively low in the near wall region. The reason for this is the relatively coarse mesh with a non-dimensional cell height of the bottom boundary cell of $\Delta y^+ = \frac{\Delta y u_*}{\nu} = 1.6$. Despite the wall-adjacent cell centre being at $y^+ < 1$, which is the generally accepted value (e.g. Davidson, 2009), there are only three cells resolving the laminar sublayer ($y^+ \leq 5$). It is not expected though that this has considerable effect on the particle sediment interaction. For this reason the flow field is considered accurate enough to be used as initial condition for the test case on sediment transport. In order to account for the non-resolved flow scales, non-dimensional wall units $y^+ = \frac{y u_*}{\nu_{\mathrm{eff}}}$ in Fig. 4b are calculated based on the effective viscosity of $\nu_{\mathrm{eff}} = 2 \times 10^{-6}\,\mathrm{m^2\,s^{-1}}$.

Fig. 5 displays two-point correlations (Eq. (21)) in streamwise and lateral direction normalized by the temporal average of the squared velocity fluctuations. In streamwise direction there are 29 cells with two-point correlation of streamwise velocity greater than 0.3 and 10 cells with two-point correlation for lateral velocity greater than 0.3, respectively. In lateral direction there are 10 cells with two-point

 Advances in Water Resources 160 (2022) 104095

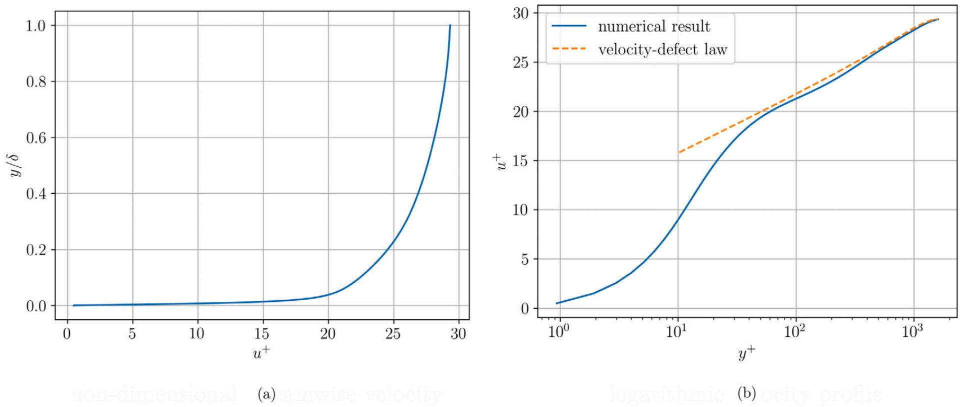


**Fig. 4.** Spatially and temporally averaged velocity profile: (a) non-dimensional streamwise velocity; (b) logarithmic velocity profile.

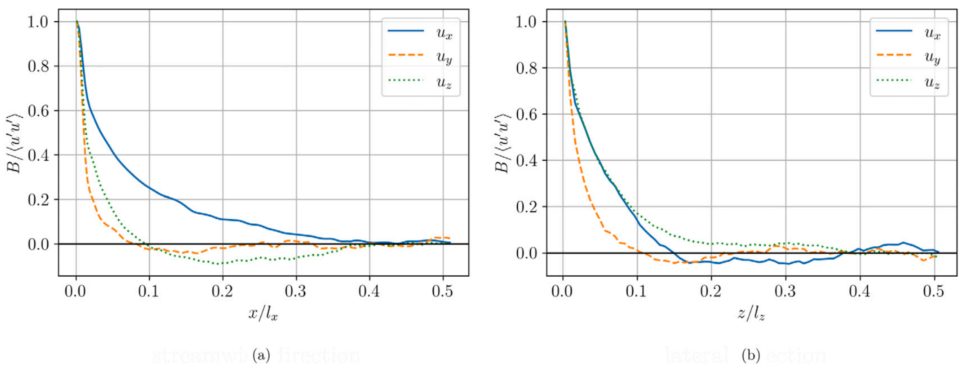


**Fig. 5.** Two-point correlation of turbulent velocity fluctuations: (a) streamwise direction; (b) lateral direction.

correlation greater than 0.3 for the streamwise and the lateral velocity component. This number of cells are considered enough to resolve large eddies but *"far from well resolved LES"* (Davidson, 2009). Similarly to the velocity profile above the fulfilment of this requirement is considered appropriate for the purpose of this study.

*3.1.2. Sediment transport*

Fall velocities $v_s$ of the sediment plume in turbulent fluid flow at a bulk velocity of $0.5\,\mathrm{m\,s^{-1}}$ are plotted against the particle diameter in Fig. 6. For particle sizes larger than 0.25 mm the fall velocity in the results of the numerical model lies within the range of fall velocities measured by Worf et al. (2019) in the laboratory. However, the fall velocity of the fraction $0.18\,\mathrm{mm} < d < 0.25\,\mathrm{mm}$ is overestimated in the numerical model with respect to the measurements from the physical model.

Worf et al. (2019) observed that some particles hardly settled at all and remained in the upper part of the channel during their experiments. They suggested that these particles have a very low shape factor (flat plates) and thus a low fall velocity. However, a constant shape factor is used in the numerical simulations. As a result the very low fall velocities of flat plates are not reproduced in the numerical model.

It is assumed that the lack of particles with very low shape factors in the numerical model causes the overestimation of the fall velocity of the fraction $0.18\,\mathrm{mm} < d < 0.25\,\mathrm{mm}$. In order to compensate for this and also include particles with Stokes numbers < 1 in the model, the range of particle sizes is extended by another fraction $0.07\,\mathrm{mm} < d < 0.18\,\mathrm{mm}$.

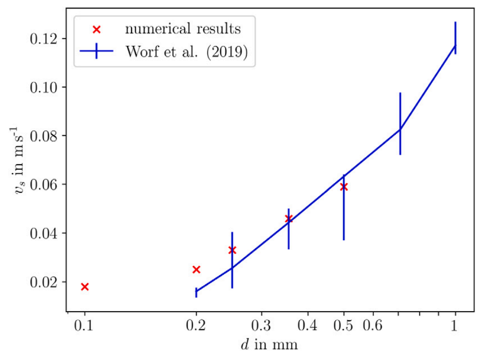


**Fig. 6.** Comparison of fall velocities in turbulent fluid flow from physical measurements and numerical model results (median and error bars).

Fig. 7 displays the particles at different timesteps after their release from the start of the channel in one exemplary simulation of the test case. The sediment plume is transported by the fluid in direction of the fluid velocity. This motion is superimposed by a gravity current as a result of the higher density of the sediment suspension compared to the surrounding clear water. In addition particles settle in negative $y$ direction. As a result of diffusion, turbulent dispersion and varying

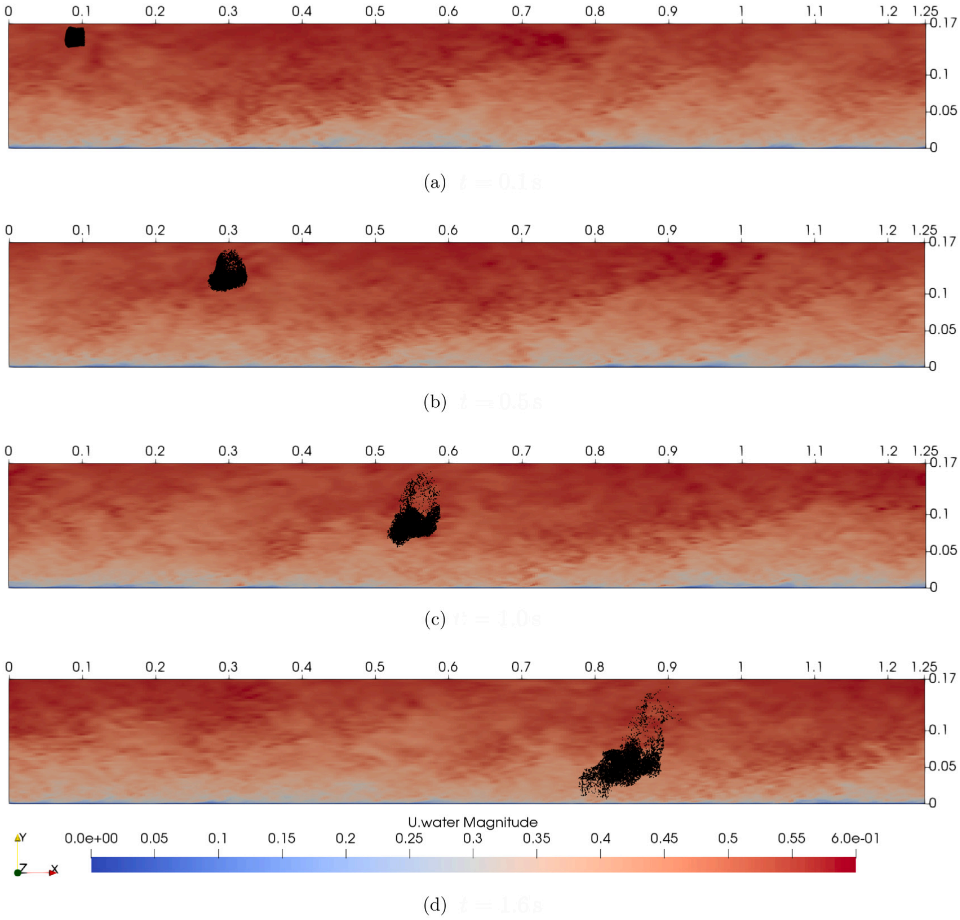


**Fig. 7.** Development of the sediment plume at different time steps after the release of sediment into turbulent flow. Velocity contours in the background are in m s$^{-1}$ and channel coordinates in m. (a) $t = 0.1$ s, (b) $t = 0.5$ s, (c) $t = 1.0$ s, (d) $t = 1.6$ s.

particle diameters the shape of the sediment plume gets distorted from its original shape.

### 3.2. Time dependent variability of the results

Fig. 8 displays the distribution of the differences $\Delta u$ of fluid velocities in cells with particles present and time-averaged fluid velocities of clear water flow in the respective cells for all 41 simulations. The velocity differences are averaged over all cells with particles present (see also Section 2.4) and normalized by the bulk flow velocity $\bar{u}$.

The one-sample Student t-test shows that streamwise fluid velocities in the sediment plume are significantly different from the respective velocity component in clear water flow over the first 0.9 s of the development of the sediment plume. For the vertical velocity component this difference is significant for the entire development of the sediment plume ($p < 0.05$). The implications of these observations on the importance of two-way coupling will be discussed in Section 3.5 below.

Development of the shape of the sediment plume is analysed on the basis of the dimensions of the bounding box enclosing the sediment particles (see Section 2.4). The development of the streamwise and vertical edge length of this bounding box, normalized by the initial edge length $l_0$ is displayed in Fig. 9.

In contrast to velocity differences, the variation of edge length of the bounding box around the sediment plume from the 41 simulations increases with time (Fig. 9). Several outliers are visible in Fig. 9a for $t \geq 1.7$ s. In these runs a number of particles have reached the bottom of the channel, from where they are not transported any further. As other particles are still in suspension and transported by the flow, the particle distribution in streamwise direction increases at a high rate.

With the exception of the streamwise plume extents for $t \geq 1.7$ s, velocity differences and plume extents in Figs. 8 and 9 show a normal distribution. This indicates that further discussion based on means over all 41 runs of the test case is justified.

### 3.3. Fluid and particle velocities

Fig. 10 displays the streamwise component of the particle velocities $v_x$ plotted against instantaneous fluid velocities $u_x$ in the respective cells. The points are coloured by the diameter of the particle they represent. Black polygons show the range of particle velocities plotted against time averaged fluid velocities in the respective cells from the precursor simulation (single-phase). An equivalent analysis for the vertical velocity components $v_y$ and $u_y$ is shown in Fig. 11.

The average overall magnitude of instantaneous fluid and particle velocities is almost equal. Only at $t = 0.5$ s and $t = 1.0$ s large particles have a slightly higher velocity than their surrounding fluid. The differences between particle and fluid velocities are decreasing with the development of the plume.

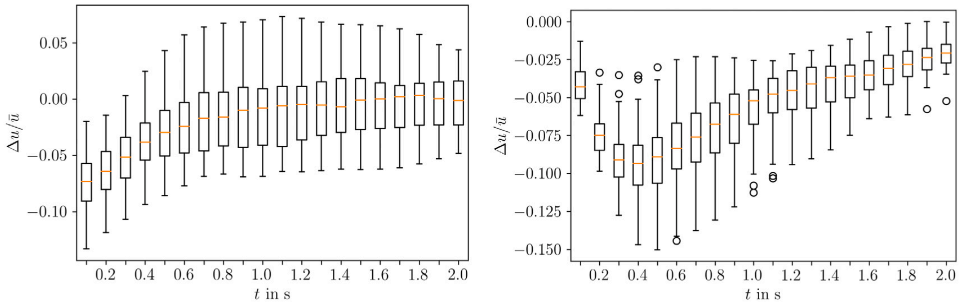


(a) (b)

**Fig. 8.** Streamwise and vertical differences between time-averaged velocities of clear water flow and fluid velocities in the area of the sediment plume. Each boxplot shows the distribution of the results from the 41 simulations at a specific time step after release of the particles. (a) streamwise velocity component; (b) vertical velocity component.

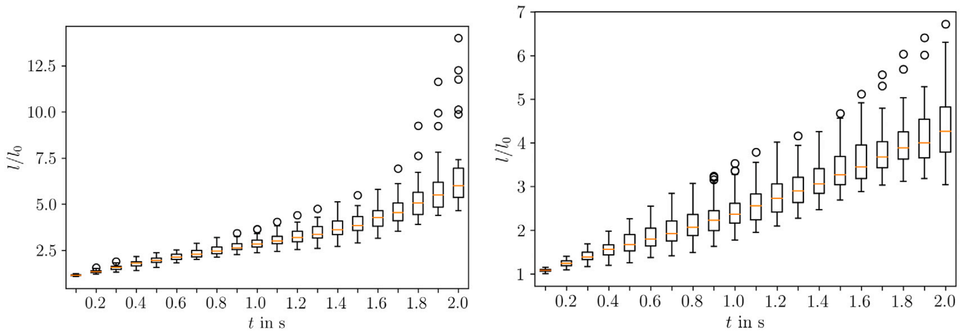


(a) (b)

**Fig. 9.** Streamwise and vertical extent of the sediment plume from the different runs in proportion to the edge length of the original cube-shaped sediment plume $l_0$. Each boxplot shows the distribution of the results from the 41 simulations at a specific time step after release of the particles. (a) streamwise extent; (b) vertical extent.

For the earlier time steps $t \leq 1.0\,\mathrm{s}$ displayed in Fig. 10 the distribution of instantaneous fluid velocities is tilted towards the lower velocities compared to clear water velocities. With advancing time and evolution of the sediment plume the range of fluid velocities in the sediment plume approaches the respective range of clear water flow from the precursor simulation. In contrast to the lower end of the fluid velocity distribution, maximum values for fluid velocities in the area of the sediment plume are hardly affected by the presence of sediment.

At $t = 0.1\,\mathrm{s}$ and $t = 0.5\,\mathrm{s}$ velocity differences between large particles and their surrounding fluid in Fig. 10 are higher than those between smaller particles and fluid. This shows the lower response time $\tau_p$ of particles with lower Stokes numbers.

In contrast to the streamwise velocity components, a clear offset between fluid and particle velocities in direction of gravity $u_y$ is visible at all time steps displayed in Fig. 11. Negative $y$ particle velocity components $v_y$ are higher than the respective fluid velocity components. The reason for this is particle settling. As large particles have higher fall velocities than small particles, particle sorting with respect to grain size is visible at all time steps in Fig. 11.

Typical single-phase models of sediment transport account for the vertical velocity difference between sediment and fluid by adding the terminal fall velocity to the particle velocity. However, a comparison of the median value of the particle–fluid vertical velocity differences in the model and the terminal velocity of the particles according to the formula by Haider and Levenspiel (1989) shows that the particle–fluid velocity difference ($0.030\,\mathrm{m\,s^{-1}}$) is slightly lower than the theoretical terminal velocity ($0.039\,\mathrm{m\,s^{-1}}$) of the particles. This is consistent with studies of fall velocities in turbulent fluid flow in literature (e.g. Worf et al., 2019).

Similarly to streamwise fluid velocities, the range of vertical fluid velocities is also extended towards negative $y$ by the particles. The reason for this is the higher density of the water sediment suspension. This phenomenon will be discussed in more detail in the following sections.

For $t \geq 0.5\,\mathrm{s}$ after the release of the sediment plume higher negative $y$-fluid velocity components are related to the presence of smaller particle diameters. This can be explained by the lower fall velocities of fine grains. Due to their lower fall velocity a larger part of their potential energy is available for the formation of the gravity current driven by the density difference between the sediment plume and the surrounding clear water (Gladstone et al., 1998). This effect is less clearly visible at $t = 0.1\,\mathrm{s}$. The reason is that larger particles have not yet separated from the smaller particles due to their higher fall velocity. Thus there are no areas in the sediment plume where certain particle sizes are dominating.

This process driven by initial particle sorting also results in a more narrow range of vertical particle velocities at later time steps $t \geq 1\,\mathrm{s}$. On the one hand small particle fractions have a lower terminal velocity but at the same time form a stronger gravity current in negative $y$ direction. On the other hand large particles have a higher fall velocity while a lower amount of their potential energy is available for acceleration of the gravity current.

In addition to buoyancy, settling particles may accelerate their surrounding fluid in the direction of gravity via drag force. While gravity currents have already been investigated in several studies in literature (e.g. Dallali and Armenio, 2015), this process is expected to play a less important role. This assumption is supported by the above described observation that fluid surrounding large particles with high

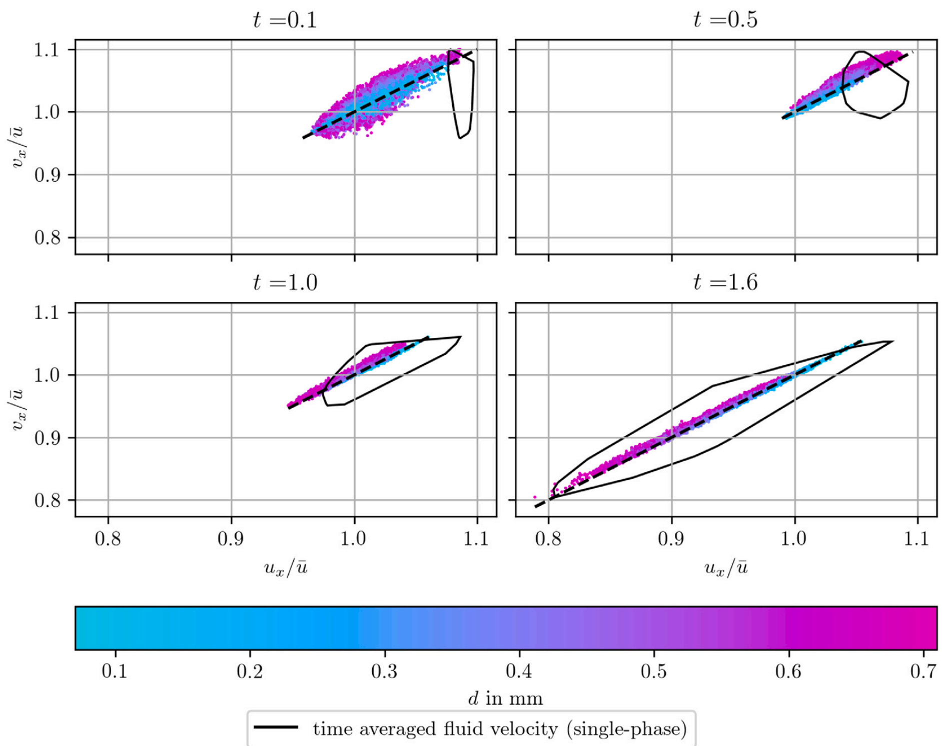


**Fig. 10.** Fluid–particle velocity comparison: streamwise component. The velocity of each particle $v_x$ is plotted on the $y$-axis against the velocity of its surrounding fluid $u_x$ on the $x$-axis. Solid black lines indicate the range of the time-averaged fluid velocities from the precursor simulation (single-phase) in the area of the sediment plume. The dashed line represents $u = v$ for reference. (For interpretation of the references to colour in this figure legend, the reader is referred to the web version of this article.)

fall velocities is less influenced by the presence of particles than fluid surrounding fine particles. Thus while the effect of buoyancy appears to be crucial for an accurate model of sediment transport, vertical momentum transfer through drag is not expected to play a major role.

### 3.4. Particle influence on fluid flow

Quadrant analysis is an efficient means of obtaining a quantitative measure for the influence of the sediment on the turbulent fluid flow (Vinkovic et al., 2011). Instantaneous fluid velocities in cells with particles present are compared to time-averaged fluid velocities of clear water flow in the respective cells. These $(u'_x, u'_y)$ fluid velocity fluctuations are displayed in Fig. 12. The colour of the points shows the volumetric sediment concentration $\Theta$ in the respective cell.

Fig. 12 shows that fluid velocities are tilted towards the third quadrant (lower streamwise velocity and higher negative vertical velocity) particularly in the earlier two time steps displayed. This again shows the slowdown of the fluid by the inertia of the sediment (see also Fig. 10) and the vertical acceleration due to the higher density of the water-sediment suspension (see also Fig. 11). Maximum positive fluid velocity fluctuations in the sediment plume are similar to those of clear water flow.

As the sediment plume evolves, particles and fluid accelerate in streamwise direction. Approximately 1 s after the particles have been placed into the fluid, streamwise velocity fluctuations are approximately within the same range as they are in clear water flow. This is consistent with observations by Nezu and Azuma (2004) who observed no influence of particles on the fluid turbulence modulation in the outer region. The offset of fluid velocity in vertical direction remains throughout the simulation, but decreases with decreasing sediment concentration.

At the first time step displayed fluid velocities in cells with the highest particle concentration deviate most from time-averaged fluid velocities. This shows that the major part of the sediment plume has not yet accelerated with the flow. Only some individual particles have been separated from the plume and transported to higher velocity flow areas. At $t = 0.5$ s streamwise fluid velocities in high concentration cells are closer to the time-averaged clear water velocity than in cells with lower concentration.

### 3.5. Development of the sediment plume

Fig. 13 displays the temporal development of velocity differences $\Delta u$ between fluid influenced by the particles and time averaged clear water flow (top). The development of the size of the sediment plume is displayed in the bottom panel. The values displayed in Fig. 13 are means of the distributions visualized as boxplots in Figs. 8 and 9, respectively. The figure is used to analyse the temporal development of the processes identified in the sections above. In addition their influence on sediment dispersion is discussed based on the extents of the sediment plume.

Temporal development of fluid velocity differences and the extents of the sediment plume in Fig. 13 indicates the existence of three phases during the development of the sediment plume:

**acceleration phase:** Initially the streamwise velocity in the sediment plume is significantly lower than in clear water flow (see also Section 3.2). At the same time the negative $y$ component continuously increases during this initial phase. The sediment plume grows in streamwise and vertical direction while its width in lateral direction is remaining constant during the first 0.2 s after particles were added to the flow.

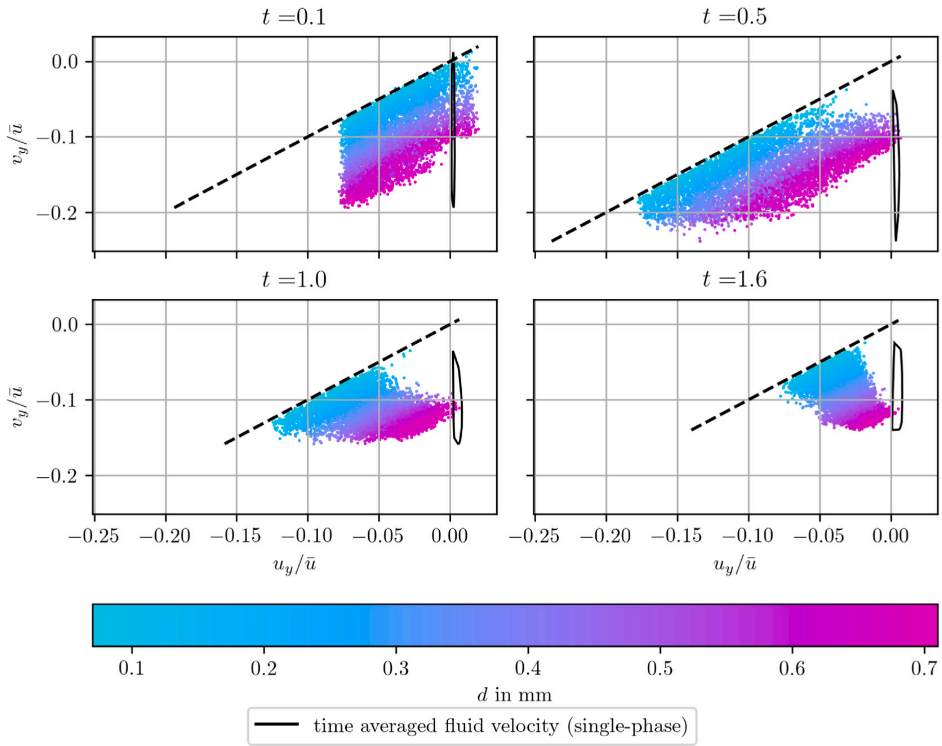


**Fig. 11.** Fluid–particle velocity comparison: vertical component. The velocity of each particle $v_y$ is plotted on the $y$-axis against the velocity of its surrounding fluid $u_y$ on the $x$-axis. Solid black lines indicate the range of time-averaged fluid velocities from the precursor simulation in the area of the sediment plume. The dashed line represents $u = v$ for reference. (For interpretation of the references to colour in this figure legend, the reader is referred to the web version of this article.)

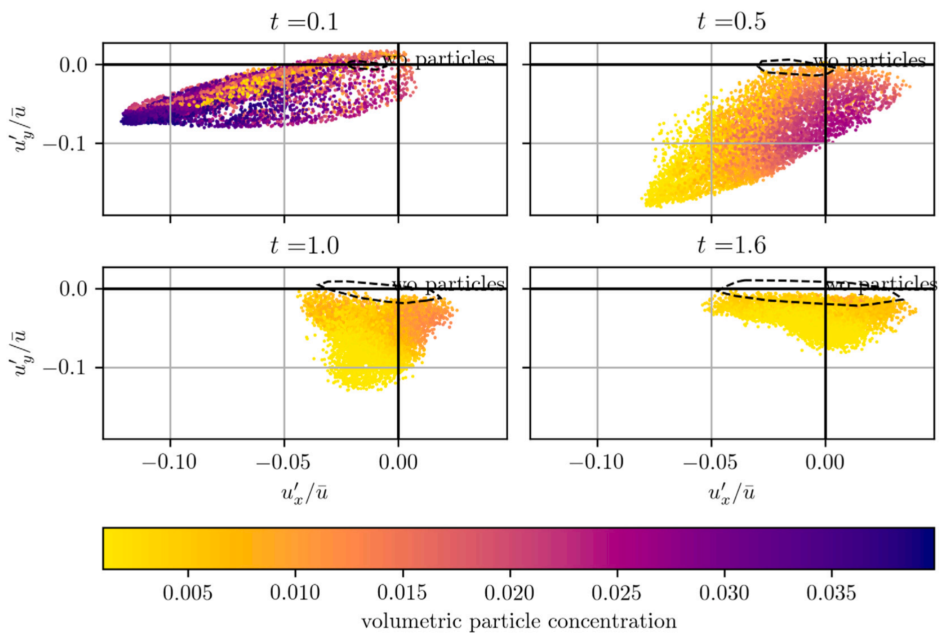


**Fig. 12.** Quadrant analysis of the average fluid velocity fluctuations in the area of the sediment plume of 41 simulations (points). Hypothetical velocity fluctuations in the same area without sediment are marked with dashed lines. (For interpretation of the references to colour in this figure legend, the reader is referred to the web version of this article.)

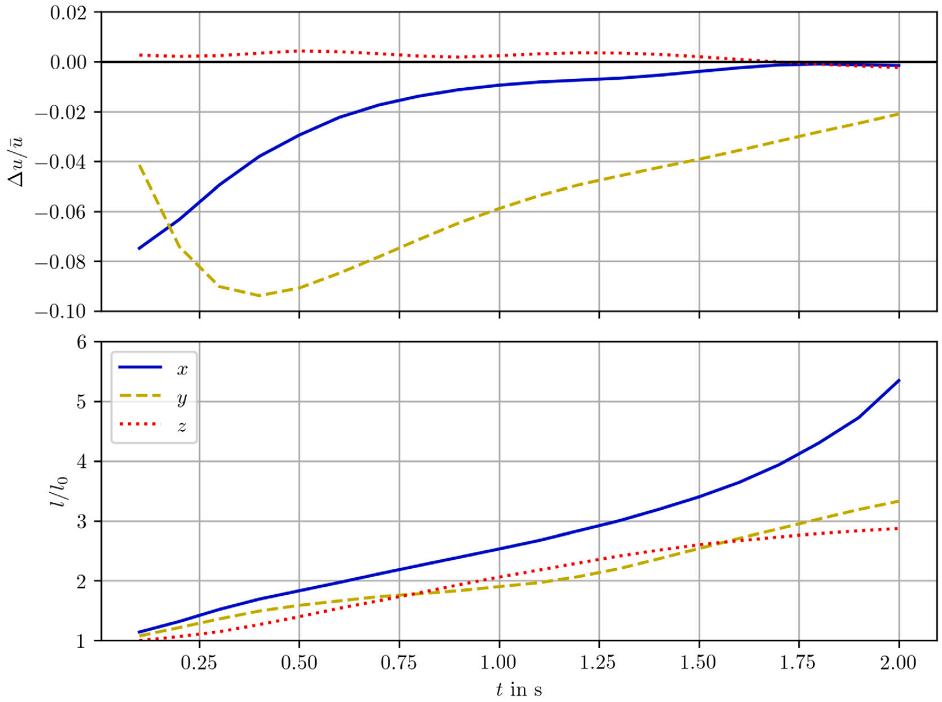


**Fig. 13.** Top: Development of three-dimensional fluid velocity differences between fluid in the area of the sediment plume and clear water flow in spatial directions $x$, $y$ and $z$. Average of all cells, weighted by the number of particles in the respective cell; bottom: Development of the edge length of a bounding box enclosing the sediment particles. In order for this analysis to be less sensitive to individual particles separated from the plume the 2.5 % of the particles on the extreme ends in each direction are not included in the bounding box.

**transport phase:** After approximately 0.4 s the sediment plume has accelerated to a streamwise velocity which is within the range of turbulent fluid velocity fluctuations of clear water flow. The rate of acceleration continuously decreases. At the same time the negative $y$ component of the fluid velocity has reached a maximum and starts to decrease. While the rate of extension of the sediment plume is decaying in $y$ direction the plume in this phase increasingly grows in lateral direction. Over a large part of the transport phase the lateral extension of the sediment plume even exceeds the vertical extension.

**deposition phase:** Approximately 1.6 s after the sediment has been placed into the channel, the mean of the instantaneous fluid velocity from all 41 simulations of the sediment plume reaches the time-averaged velocity of the clear water flow. Sediment dispersion is increasing in $x$ direction. Vertical extent of the sediment plume exceeds the lateral one.

As particles are placed into the channel at an initial velocity of zero, sediment acts as an obstacle for fluid flow. The resulting decrease of streamwise fluid velocity has already been observed in Figs. 10 and 12 for $t = 0.1$ s and $t = 0.5$ s. Fig. 13 now shows that it takes approximately 0.5 s for the sediment plume to be accelerated by the surrounding water through drag forces. At the end of the acceleration phase, streamwise acceleration of the sediment plume decreases. In the transport phase a significant lag between streamwise velocities in the sediment plume and time-averaged fluid velocities of clear water remains (see also Fig. 8). This is consistent with the observations of Nezu and Azuma (2004) and Muste et al. (2005).

The high difference between streamwise velocities of clear water flow and fluid velocities in the sediment plume (Figs. 10, 12 and 13) shows the importance of two-way coupling particularly in the acceleration phase. Alternatively a time dependent velocity correction could be applied in one-way coupled models for this initial phase of sediment transport. With such a correction accounting for the lower fluid velocities in the initial phase of the development of the sediment plume it is expected that particle trajectories can also be captured with reasonable accuracy e.g. using an eddy interaction model (Cheng et al., 2018a).

The acceleration in negative $y$ direction in the acceleration phase is a result of the surplus density of the water-sediment suspension in the area of the sediment plume compared to the surrounding clear water. Heavier water-sediment suspension falls below the lighter clear water. The process has already been observed in Figs. 11 and 12 at four particular time steps. Fig. 13 shows that at the transition from the acceleration phase to the transport phase this gravity current reaches its maximum velocity. In the transport phase the gravity current is decaying due to ongoing dispersion and thus reduction of sediment concentration.

At its peak the average buoyancy induced vertical velocity differences between sediment plume and clear water flow reach a magnitude of almost 10 % of the bulk velocity. Hence this process should be included in models for the development of a sediment plume. The influence of the buoyancy can be implemented relatively easy by a source term in the fluid momentum equation without the need for a complete two-way coupled model (Necker et al., 2002; An et al., 2012; Dallali and Armenio, 2015). Dallali and Armenio (2015) particularly showed the effect of buoyancy on steady sediment transport in turbulent fluid flow using this method.

In the transport phase a one-way coupling approach for sediment transport modelling can be sufficient for achieving acceptable modelling results. In such a case effects of sediment on the fluid which have already been parametrized should still be accounted for. These include the reduction of the von Kármán constant (Nezu and Azuma, 2004; Ferreira, 2015; Cheng et al., 2018b), effects of sediment particles on fluid turbulence (Hsu and Liu, 2004) and turbulent dispersion (e.g. using an eddy-interaction model; Cheng et al., 2018a)

In the deposition phase the concentration in the sediment plume has reduced to the point that drag forces only have a minor effect on the fluid flow. Thus mean streamwise and lateral velocities in the sediment approach the time-averaged respective fluid velocity of clear water flow. For the vertical velocity component an offset remains resulting from buoyancy.

Temporal development of the dimensions of the bounding box encircling the sediment plume in Fig. 13b also shows the three phases analysed above for fluid velocity. While hardly any dispersion takes place in lateral direction particularly in the beginning of the acceleration phase, the sediment plume grows in streamwise and vertical direction at a relatively high rate.

The streamwise velocity difference between clear water flow and the sediment plume in the acceleration phase provides an explanation for the low initial dispersion in lateral direction. Sediment leaving the core of the plume in lateral direction is immediately taken up by the flow inhibiting further movement normal to the flow. This results in an increased dispersion in streamwise direction and at the same time reduced dispersion in lateral direction. None of these processes are accounted for in one-way coupled models and even many two-way coupled Euler–Euler models.

The relatively high dispersion of sediment in the acceleration phase in vertical direction, particularly compared to lateral dispersion, is a result of the high range of particle sizes included in the model (Fig. 11). The difference in fall velocities causes the continuous extension in direction of gravity.

In the transport phase the sediment plume has accelerated in streamwise and vertical direction but at the same time still is compact so that the flow is highly stratified in the area of the sediment plume. According to literature stratification inhibits vertical dispersion (Dallali and Armenio, 2015). The flattening of the growth rate of the sediment plume in the transport phase is consistent with this.

In addition further vertical separation of small and large particles is inhibited by small particles inducing higher vertical fluid velocities than large particles. This compensates for lower fall velocities of small particles. This process, already described above and visible in Fig. 11, additionally causes lower vertical dispersion in the transport phase compared to the acceleration phase.

As the major part of the sediment plume has accelerated with the bulk of the flow, the velocity difference between sediment plume and surrounding water is lower. Hence lateral dispersion increases in the transport phase. At $t = 1\,\mathrm{s}$ after the release of the sediment the streamwise extent amounts to $2.5l_0$, the vertical extent to $1.9l_0$ and the lateral extent to $2.1l_0$, respectively.

When the sediment plume approaches the bottom wall of the channel the vertical velocity gradient increases. Fig. 10 shows the high range of velocities in cells with particles present at the beginning of the deposition phase ($t = 1.6\,\mathrm{s}$). Particularly larger particles have already fallen to an area of the flow field where streamwise velocities are substantially lower due to wall friction. The high velocity difference between different areas of the sediment plume causes a distortion of the sediment plume in streamwise direction and hence an increasing streamwise extent.

In addition turbulent velocity fluctuations are higher close to the bottom wall. This enhances sediment dispersion also in vertical direction which exceeds lateral dispersion in the deposition phase. This is consistent with findings of Vinkovic et al. (2011).

## 4. Conclusions

Average values of the simulation results show that the development of the sediment plume is dependent on the time passed since the particles have been released. In addition the position of the sediment within the channel cross section influences the sediment transport processes. Three phases of the development of the sediment plume are identified: (i) acceleration phase, (ii) transport phase and (iii) deposition phase.

Transport processes of the sediment plume can be related to these three phases. Particularly in the acceleration phase fluid velocities are decreased by the inertia of the sediment. In addition the surplus density of the sediment suspension compared to the surrounding clear fluid induces a gravity current resulting in a shift of fluid velocities in direction of gravity. The development of the sediment plume is driven by high temporal and spatial velocity gradients.

In the transport phase initial acceleration of the sediment plume is completed. Streamwise velocity components of the sediment plume remain slightly lower than the respective component in clear water flow, but the difference is not statistically significant any more as the plume evolves. Turbulent dispersion and thus continuous reduction of sediment concentration are the main processes driving the development of the sediment plume. From the results of the simulations in this study it is expected that the development of the sediment plume in this phase can be modelled with sufficient accuracy using a less detailed approach for particle–fluid interaction as long as the effect of buoyancy is considered.

The final deposition phase is characterized by a higher vertical velocity gradient close to the bottom boundary. This causes a distortion of the sediment plume in streamwise direction due to faster movement of particles in the upper area of the plume compared to particles close to the channel bed.

The simulation results of this study show the following processes related to the development of the sediment plume which are not captured by one-way coupled models:

- significant slow down of streamwise fluid velocity in the acceleration phase as a result of the inertia of the sediment
- additional streamwise dispersion in the acceleration phase due to increased variability of fluid velocities in the sediment plume
- reduced streamwise velocity in the transport phase, depending on particle concentration
- reduced vertical dispersion in the transport phase due to stratification as well as particle sorting
- vertical acceleration of the fluid due to buoyancy (already implemented in many models through a source term in the fluid momentum equation)

For both, fluid velocities as well as the development of the sediment plume, the acceleration phase turned out to be the phase of the sediment transport with the highest dynamics. Many processes in this phase are not accounted for in numerical models of sediment transport. This explains challenges in modelling the development of a sediment plume.

Our findings related to the development of the sediment plume in the acceleration phase can be used to improve results of models using a less detailed approach for particle–fluid interaction. For example a sediment plume can be initialized at a position and shape which is expected to occur after the acceleration phase (e.g. using $2.5l_0$ for the streamwise extent, $1.9l_0$ for the vertical extent and $2.1l_0$ for the lateral extent $1\,\mathrm{s}$ after the sediment was added to the flow, see Fig. 13). This way modelling the acceleration phase using a possibly unsuitable approach is avoided. This would allow to model particle–fluid interaction and turbulence in lower detail in the transport phase. Thus a larger spatial and temporal extent can be covered by the model for instance to optimize sediment dumping throughout an entire river section.

## CRediT authorship contribution statement

**Daniel Wildt:** Conceptualization, Data curation, Formal analysis, Investigation, Methodology, Software, Validation, Visualization, Writing – original draft. **Christoph Hauer:** Funding acquisition, Project administration, Resources, Supervision, Validation, Writing – review & editing. **Helmut Habersack:** Funding acquisition, Supervision, Writing

– review & editing. **Michael Tritthart:** Conceptualization, Funding acquisition, Methodology, Project administration, Resources, Software, Supervision, Validation, Writing – review & editing.

## Declaration of competing interest

The authors declare that they have no known competing financial interests or personal relationships that could have appeared to influence the work reported in this paper.

## Acknowledgements

The authors would like to thank Prof. Rui M.L. Ferreira for his valuable advice on particle–fluid momentum exchange as well as Dominik Worf for providing data for the validation of the numerical model. The computational results presented have been achieved using the Vienna Scientific Cluster (VSC). All authors have read and agreed to the published version of the manuscript.

## Funding

This paper was written as a contribution to the Christian Doppler Laboratory for Sediment Research and Management. In this context, the financial support by the Christian Doppler Research Association, Austria, the Austrian Federal Ministry for Digital and Economic Affairs and the National Foundation for Research, Technology and Development is gratefully acknowledged.

## References

Amoudry, L.O., 2014. Extension of k-omega turbulence closure to two-phase sediment transport modelling: Application to oscillatory sheet flows. Adv. Water Resour. (ISSN: 0309-1708) 72, 110–121. http://dx.doi.org/10.1016/j.advwatres.2014.07.006.

An, S., Julien, P.Y., Venayagamoorthy, S.K., 2012. Numerical simulation of particle-driven gravity currents. Environ. Fluid Mech. (ISSN: 1567-7419) 12 (6), 495–513. http://dx.doi.org/10.1007/s10652-012-9251-6.

Andrews, M., O'Rourke, P., 1996. The multiphase particle-in-cell (MP-PIC) method for dense particulate flows. Int. J. Multiph. Flow. (ISSN: 0301-9322) 22 (2), 379–402. http://dx.doi.org/10.1016/0301-9322(95)00072-0.

Bomminayuni, S., Stoesser, T., 2011. Turbulence statistics in an open-channel flow over a rough bed. J. Hydraul. Eng. 137 (11), 1347–1358. http://dx.doi.org/10.1061/(ASCE)HY.1943-7900.0000454.

Canelas, R., Crespo, A., Domínguez, J., Ferreira, R., Gómez-Gesteira, M., 2016. SPH-DCDEM model for arbitrary geometries in free surface solid-fluid flows. Comput. Phys. Comm. (ISSN: 0010-4655) 202, 131–140. http://dx.doi.org/10.1016/j.cpc.2016.01.006.

Canelas, R., Domínguez, J., Crespo, A., Gómez-Gesteira, M., Ferreira, R., 2017. Resolved simulation of a granular-fluid flow with a coupled SPH-dcdem model. J. Hydraul. Eng. (ISSN: 0733-9429) 143 (9), http://dx.doi.org/10.1061/(ASCE)HY.1943-7900.0001331.

Cheng, Z., Chauchat, J., Hsu, T.-J., Calantoni, J., 2018a. Eddy interaction model for turbulent suspension in Reynolds-averaged Euler-Lagrange simulations of steady sheet flow. Adv. Water Resour. (ISSN: 0309-1708) 111, 435–451. http://dx.doi.org/10.1016/j.advwatres.2017.11.019.

Cheng, Z., Hsu, T.-J., Calantoni, J., 2017. SedFoam: A multi-dimensional Eulerian two-phase model for sediment transport and its application to momentary bed failure. Coast. Eng. (ISSN: 0378-3839) 119, 32–50. http://dx.doi.org/10.1016/j.coastaleng.2016.08.007.

Cheng, Z., Hsu, T.-J., Chauchat, J., 2018b. An Eulerian two-phase model for steady sheet flow using large-eddy simulation methodology. Adv. Water Resour. (ISSN: 0309-1708) 111, 205–223. http://dx.doi.org/10.1016/j.advwatres.2017.11.016.

Crespo, A., Domínguez, J., Rogers, B., Gómez-Gesteira, M., Longshaw, S., Canelas, R., Vacondio, R., Barreiro, A., García-Feal, O., 2015. DualSPHysics: Open-source parallel CFD solver based on smoothed particle hydrodynamics (SPH). Comput. Phys. Comm. (ISSN: 0010-4655) 187, 204–216. http://dx.doi.org/10.1016/j.cpc.2014.10.004.

Cundall, P.A., Strack, O.D.L., 1979. A discrete numerical model for granular assemblies. Geotechnique 29 (1), 47–65, URL: www.scopus.com.

Dallali, M., Armenio, V., 2015. Large eddy simulation of two-way coupling sediment transport. Adv. Water Resour. (ISSN: 0309-1708) 81, 33–44. http://dx.doi.org/10.1016/j.advwatres.2014.12.004.

Davidson, L., 2009. Large eddy simulations: How to evaluate resolution. Int. J. Heat Fluid Flow (ISSN: 0142-727X) 30 (5), 1016–1025. http://dx.doi.org/10.1016/j.ijheatfluidflow.2009.06.006.

De Cesare, G., Schleiss, A., Hermann, F., 2001. Impact of turbidity currents on reservoir sedimentation. J. Hydraul. Eng. (ISSN: 0733-9429) 127 (1), 6–16. http://dx.doi.org/10.1061/(ASCE)0733-9429(2001)127:1(6).

Dey, S., 2014. In: Rowiński, P. (Ed.), Fluvial Hydrodynamics. Springer, ISBN: 978-3-642-19062-9, http://dx.doi.org/10.1007/978-3-642-19062-9.

Durda, D.D., Movshovitz, N., Richardson, D.C., Asphaug, E., Morgan, A., Rawlings, A.R., Vest, C., 2011. Experimental determination of the coefficient of restitution for meter-scale granite spheres. Icarus (ISSN: 0019-1035) 211 (1), 849–855. http://dx.doi.org/10.1016/j.icarus.2010.09.003.

Elghannay, H., Tafti, D., 2018. Les-dem simulations of sediment transport. Int. J. Sediment Res. (ISSN: 1001-6279) 33 (2), 137–148. http://dx.doi.org/10.1016/j.ijsrc.2017.09.006.

Elghobashi, S., 1994. On predicting particle-laden turbulent flows. Appl. Sci. Res. (ISSN: 0003-6994) 52 (4), 309–329.

Fernandes, C., Semyonov, D., Ferrás, L.L., Nóbrega, J.M., 2018. Validation of the CFD-dpm solver dpmfoam in *OpenFOAM*® through analytical, numerical and experimental comparisons. Granul. Matter (ISSN: 1434-5021) 20 (4), 1–18. http://dx.doi.org/10.1007/s10035-018-0834-x.

Ferreira, R., 2015. The von Kármán constant for flows over rough mobile beds. Lessons learned from dimensional analysis and similarity. Adv. Water Resour. (ISSN: 0309-1708) 81, 19–32. http://dx.doi.org/10.1016/j.advwatres.2014.10.004.

Ferziger, J.H., Perić, M., 2002. Computational Methods for Fluid Dynamics, third ed. Springer-Verlag, ISBN: 3-540-42074-6.

Gladstone, C., Phillips, J.C., Sparks, R.S.J., 1998. Experiments on bidisperse, constant-volume gravity currents: propagation and sediment deposition. Sedimentology 45 (5), 833–843. http://dx.doi.org/10.1046/j.1365-3091.1998.00189.x.

Greenshields, C.J., 2018. OpenFOAM. Ed. by OpenFOAM Foundation Ltd., User Guide. Version 6, URL: http://openfoam.org.

Greimann, B.P., Muste, M., Holly, Jr., F.M., 1999. Two-phase formulation of suspended sediment transport. J. Hydraul. Res. 37 (4), 479–500. http://dx.doi.org/10.1080/00221686.1999.9628264.

Guo, J., 2017. Eddy viscosity and complete log-law for turbulent pipe flow at high Reynolds numbers. J. Hydraul. Res. 55 (1), 27–39. http://dx.doi.org/10.1080/00221686.2016.1212945.

Haider, A., Levenspiel, O., 1989. Drag coefficient and terminal velocity of spherical and nonspherical particles. Powder Technol. (ISSN: 0032-5910) 58 (1), 63–70. http://dx.doi.org/10.1016/0032-5910(89)80008-7.

Haimann, M., Hauer, C., Tritthart, M., Prenner, D., Leitner, P., Moog, O., Habersack, H., 2018. Monitoring and modelling concept for ecological optimized harbour dredging and fine sediment disposal in large rivers. Hydrobiologia (ISSN: 1573-5117) 814 (1), 89–107. http://dx.doi.org/10.1007/s10750-016-2935-z.

Hauer, C., Wagner, B., Aigner, J., Holzapfel, P., Flödl, P., Liedermann, M., Tritthart, M., Sindelar, C., Pulg, U., Klösch, M., Haimann, M., Donnum, B.O., Stickler, M., Habersack, H., 2018. State of the art, shortcomings and future challenges for a sustainable sediment management in hydropower: A review. Renew. Sustain. Energy Rev. (ISSN: 1364-0321) 98, 40–55. http://dx.doi.org/10.1016/j.rser.2018.08.031.

Hillebrand, G., Klassen, I., Olsen, N.R.B., 2017. 3D CFD modelling of velocities and sediment transport in the iffezheim hydropower reservoir. Hydrol. Res. (ISSN: 1998-9563) 48 (1), 147–159. http://dx.doi.org/10.2166/nh.2016.197.

Hsu, T., Liu, P., 2004. Toward modeling turbulent suspension of sand in the nearshore. J. Geophys. Res. Oceans (ISSN: 2169-9275) 109 (C6), http://dx.doi.org/10.1029/2003JC002240.

Hunt, J.N., Inglis, C.C., 1954. The turbulent transport of suspended sediment in open channels. Proc. R. Soc. London. Ser. A 224 (1158), 322–335. http://dx.doi.org/10.1098/rspa.1954.0161.

Kranenburg, W.M., Hsu, T.-J., Ribberink, J.S., 2014. Two-phase modeling of sheet-flow beneath waves and its dependence on grain size and streaming. Adv. Water Resour. (ISSN: 0309-1708) 72, 57–70. http://dx.doi.org/10.1016/j.advwatres.2014.05.008.

La Rocca, M., Adduce, C., Sciortino, G., Pinzon, A., 2008. Experimental and numerical simulation of three-dimensional gravity currents on smooth and rough bottom. Phys. Fluids (ISSN: 1070-6631) 20 (10), http://dx.doi.org/10.1063/1.3002381.

Lavelli, A., Boillat, J.J., De Cesare, G., 2002. Numerical 3D modelling of the vertical mass exchange induced by turbidity currents in lake lugano (Switzerland). In: 5th International Conference on Hydro-Science and – Engineering (ICHE-2002).

Liu, D., Liu, X., Fu, X., 2018. Les-dem simulations of sediment saltation in a rough-wall turbulent boundary layer. J. Hydraul. Res. 1–12. http://dx.doi.org/10.1080/00221686.2018.1509384.

Lobovský, L., Křena, J., 2007. Smoothed particle hydrodynamics modelling of fluids and solids. Appl. Comput. Mech. 1, 521–530.

Lun, C.K.K., Savage, S.B., Jeffrey, D.J., Chepurniy, N., 1984. Kinetic theories for granular flow: inelastic particles in couette flow and slightly inelastic particles in a general flowfield. J. Fluid Mech. 140, 223–356. http://dx.doi.org/10.1017/S0022112084000586.

Lysenko, D., Ertesvåg, I., Rian, K., 2012. Large-eddy simulation of the flow over a circular cylinder at Reynolds number 3900 using the OpenFOAM toolbox. Flow Turbulence Combust. 491–518. http://dx.doi.org/10.1007/s10494-012-9405-0.

Maxey, M., Riley, J., 1983. Equation of motion for a small rigid sphere in a nonuniform flow. Phys. Fluids (ISSN: 1070-6631) 26 (4), 883–889. http://dx.doi.org/10.1063/1.864230.

Muste, M., Yu, K., Fujita, I., Ettema, R., 2005. Two-phase versus mixed-flow perspective on suspended sediment transport in turbulent channel flows. Water Resour. Res. (ISSN: 0043-1397) 41 (10), http://dx.doi.org/10.1029/2004WR003595.

Necker, F., Härtel, C., Kleiser, L., Meiburg, E., 2002. High-resolution simulations of particle-driven gravity currents. Int. J. Multiph. Flow. (ISSN: 0301-9322) 28 (2), 279–300. http://dx.doi.org/10.1016/S0301-9322(01)00065-9.

Nezu, I., Azuma, R., 2004. Turbulence characteristics and interaction between particles and fluid in particle-laden open channel flows. J. Hydraul. Eng. 130 (10), 988–1001. http://dx.doi.org/10.1061/(ASCE)0733-9429(2004)130:10(988).

Nezu, I., Rodi, W., 1986. Open-channel flow measurements with a laser Doppler anemometer. J. Hydraul. Eng. 112 (5), 335–355. http://dx.doi.org/10.1061/(ASCE)0733-9429(1986)112:5(335).

O'Rourke, P.J., Snider, D.M., 2012. Inclusion of collisional return-to-isotropy in the MP-PIC method. Chem. Eng. Sci. (ISSN: 0009-2509) 80, 39–54. http://dx.doi.org/10.1016/j.ces.2012.05.047.

Ota, K., Sato, T., Nakagawa, H., 2019. Quantification of spatial lag effect on sediment transport around a hydraulic structure using Eulerian–Lagrangian model. Adv. Water Resour. (ISSN: 0309-1708) 129, 281–296. http://dx.doi.org/10.1016/j.advwatres.2017.11.009.

Pahar, G., Dhar, A., 2017. Coupled incompressible smoothed particle hydrodynamics model for continuum-based modelling sediment transport. Adv. Water Resour. 102, 84–98. http://dx.doi.org/10.1016/j.advwatres.2017.02.003.

Pope, S.B., 2000. Turbulent Flows. Cambridge University Press, ISBN: 978-0-521-59886-6, p. 769.

Prasath, S.G., Vasan, V., Govindarajan, R., 2019. Accurate solution method for the maxey-riley equation, and the effects of basset history. J. Fluid Mech. 868, 428–460. http://dx.doi.org/10.1017/jfm.2019.194.

Rouse, H., 1939. An analysis of sediment transportation in the light of fluid turbulence. California Institute of Technology.

Saffman, P.G., 1965. The lift on a small sphere in a slow shear flow. J. Fluid Mech. 22 (2), 385–400. http://dx.doi.org/10.1017/S0022112065000824.

Smagorinsky, J., 1963. General circulation experiments with primitive equations: I. the basic experiment. Mon. Weather Rev. 91 (3), 99–164. http://dx.doi.org/10.1175/1520-0493(1963)091<0099:GCEWTP>2.3.CO;2.

Snider, D., 2001. An incompressible three-dimensional multiphase particle-in-cell model for dense particle flows. J. Comput. Phys. (ISSN: 0021-9991) 170 (2), 523–549. http://dx.doi.org/10.1006/jcph.2001.6747.

Squires, K.D., Eaton, J.K., 1990. Particle response and turbulence modification in isotropic turbulence. Phys. Fluids A 2 (7), 1191–1203. http://dx.doi.org/10.1063/1.857620.

Sun, R., Sun, H., Xiao, H., 2017. Realistic representation of grain shapes in CFD-DEM simulations of sediment transport with a bonded-sphere approach. Adv. Water Resour. (ISSN: 0309-1708) 107, 421–438. http://dx.doi.org/10.1016/j.advwatres.2017.04.015.

Sun, R., Sun, H., Xiao, H., 2018. Investigating the settling dynamics of cohesive silt particles with particle-resolving simulations. Adv. Water Resour. (ISSN: 0309-1708) 111, 406–422. http://dx.doi.org/10.1016/j.advwatres.2017.11.012.

Tsuji, Y., Tanaka, T., Ishida, T., 1992. Lagrangian numerical simulation of plug flow of cohesionless particles in a horizontal pipe. Powder Technol. (ISSN: 0032-5910) 71 (3), 239–250. http://dx.doi.org/10.1016/0032-5910(92)88030-L.

Vinkovic, I., Doppler, D., Lelouvetel, J., Buffat, M., 2011. Direct numerical simulation of particle interaction with ejections in turbulent channel flows. Int. J. Multiph. Flow. (ISSN: 0301-9322) 37 (2), 187–197. http://dx.doi.org/10.1016/j.ijmultiphaseflow.2010.09.008.

Worf, D., Schobesberger, J., Lichtneger, P., Habersack, H., Sindelar, C., 2019. Sedimentation velocity of Saualm crystalline using image processing methods. In: 16th International Symposium on Water Management and Hydraulic Engineering. (Skopje, North Macedonia).

Yücesan, S., Wildt, D., Gmeiner, P., Schobesberger, J., Hauer, C., Sindelar, C., Habersack, H., Tritthart, M., 2021. Interaction of very large scale motion of coherent structures with sediment particle exposure. Water (ISSN: 2073-4441) 13 (3), http://dx.doi.org/10.3390/w13030248.

Zhong, D., Wang, G., Sun, Q., 2011. Transport equation for suspended sediment based on two-fluid model of solid/liquid two-phase flows. J. Hydraul. Eng. (ISSN: 0733-9429) 137 (5), 530–542. http://dx.doi.org/10.1061/(ASCE)HY.1943-7900.0000331.

Zhong, D., Wang, G., Wu, B., 2014. Drift velocity of suspended sediment in turbulent open channel flows. J. Hydraul. Eng. (ISSN: 0733-9429) 140 (1), 35–47. http://dx.doi.org/10.1061/(ASCE)HY.1943-7900.0000798.

# 5 Conference proceedings

## 5.1 UACEG (2019): "CFD Modelling of Turbidity Currents"

UNIVERSITY
OF ARCHITECTURE
CIVIL ENGINEERING
AND GEODESY

| | |
|---|---|
| Event: | International Jubilee Scientific Conference 70th anniversary FHE of the UACEG |
| Venue: | University of Architecture, Civil Engineering and Geodesy<br>Faculty of Hydraulic Engineering<br>Sofia, Bulgaria |
| Date: | 7 – 8 November 2019 |
| Page: | 48 |
| Authors: | Daniel Wildt and Michael Tritthart |

International Jubilee Scientific Conference
70th anniversary FHE of the UACEG

7-8 NOVEMBER 2019
7-8 НОЕМВРИ 2019

Международна Юбилейна Научна Конференция
70 години ХТФ на УАСГ

# CFD MODELLING OF TURBIDITY CURRENTS

**D. Wildt[1], M. Tritthart[2]**

***Keywords***: *turbidity currents, sediment, reservoir, computational fluid dynamics*

## ABSTRACT

Reservoir sedimentation results in ongoing loss of storage capacity all around the world. Thus effective sediment management in reservoirs is becoming an increasingly important task. Turbidity currents are the main transport medium for fine sediments in reservoirs and can even redistribute sediments within a reservoir. In the current project the capability of modelling particle driven gravity currents has been implemented into the RSim-3D hydrodynamic code. This has been realised through a buoyancy term which was added as a source term to the z-momentum equation. The model was successfully validated using literature data from lock exchange experiments. Additional focus is put on sediment deposition and remobilization caused by turbidity currents. These phenomena were studied by numerically modelling a flume experiment and observing sediment depositions on a horizontal plane at the end of the flume. In future the model will be applied to a real reservoir to support optimising sediment management.

[1] D. Wildt, MSc, University of Natural Resources and Life Sciences, Vienna, e-mail: daniel.wildt@boku.ac.at
[2] M. Tritthart, PhD, University of Natural Resources and Life Sciences, Vienna, e-mail: michael.tritthart@boku.ac.at

## 5.2 IAHR Europe (2021): "LES two phase modelling of suspended sediment transport using a two way coupled Euler-Lagrangian approach"


| | |
|---|---|
| Event: | 6th IAHR Europe Congress "No Frames no Borders" |
| Venue: | Warsaw, Poland; online |
| Date: | 14 – 18 February 2021 |
| ISBN: | 978-83-66847-01-9 |
| Pages: | 643 – 644 |
| Authors: | Daniel Wildt, Sencer Yücesan, Christoph Hauer, Helmut Habersack and Michael Tritthart |

6th IAHR Europe Congress
Warsaw Poland 2020

6th IAHR Europe Congress, June 30th – July 2nd, 2020, Warsaw, Poland

# LES two phase modelling of suspended sediment transport using a two way coupled Euler-Lagrangian approach

Daniel WILDT[1,2], Sencer YÜCESAN[1,2], Christoph HAUER[1,2], Helmut HABERSACK[2], Michael TRITTHART[1,2]

[1] Christian Doppler Laboratory for Sediment Research and Management,
[2] Institute of Hydraulic Engineering and River Research, Department of Water, Atmosphere and Environment, University of Natural Resources and Life Sciences, Vienna
Muthgasse 107, 1190, Vienna, Austria

email: daniel.wildt@boku.ac.at

ABSTRACT

A two phase LES model using Euler-Lagrangian two-way coupling has been developed in OpenFOAM. The model shall be used for the analysis of the development of a sediment plume in a river. Calibration and validation of the model has been performed using literature values for fall velocity and settling experiments.

## 1. Aims and objectives

Efficient sediment management requires detailed process understanding of sediment transport in rivers. Despite this fact current literature is still lacking information on that subject. Models of suspended sediment transport are often based on simple advection-diffusion equations (Hauer et al., 2018). To enhance process understanding the aim of this study is to develop a high fidelity computational fluid dynamics model of suspended sediment transport in a channel.

## 2. Methods

### *2.1. Governing equations and modeling approach*

The development of a sediment plume in a channel is studied using a two phase LES model. The flow of the continuous phase is governed by the three-dimensional Navier-Stokes equations. It is modeled using the Eulerian approach on a structured mesh (5.2 Mio. cells). The movement of the dispersed phase (particles) is governed by Newton's law of motion and modeled using the Lagrangian approach. Momentum exchange between the two phases is modeled on the basis of the drag force calculated using an approach by Haider et al. (1989). The model is solved using a modified version of the OpenFOAM-solver MPPICFoam, neglecting gravity for the continuous phase and using the PISO alogrithm for pressure coupling (Greenshields, 2018).

Turbulent channel flow is simulated in a rectangular channel of the same cross-sectional dimensions as the channel used in the experiments by Worf et al. (2019). No-slip boundary conditions are applied for walls, a slip boundary for the free surface, a von Neumann boundary condition at the outlet and a Dirichlet boundary condition at the inlet. For the latter turbulent flow has been recorded on a plane in a precursor-simulation of a channel with the same cross-sectional dimensions and cyclic boundary conditions for outlet and inlet. The LES model of turbulent channel flow has been validated by Yücesan et al. (2020).

### *2.2. Calibration and validation test cases*

Momentum exchange between the two phases is validated on the basis of fall velocity in still water. Nine perfectly rounded, spherical particles ($\rho_s$ = 2650 kgm$^{-3}$, $D_n$ = 0.5 mm), are released from the top of a rectangular domain. Their fall velocity is compared to an empirical formula developed by Dietrich (1982). The boundary conditions for the Eulerian model of the continuous phase are cyclic in all directions. In order to reproduce the settling behavior of the particles used by Worf et al. (2019) ($\rho_s$ = 2650 kgm$^{-3}$, $D_n$ = 0.6 mm) as accurately as possible, the shape factor is then calibrated with respect to the measured fall velocity in the experiments from Worf et al. (2019) using the same model setup as above.

Validation of the model of suspended sediment transport in turbulent channel flow is done on the basis of observations by Worf et al. (2019). In this experiment sediment is released into a laboratory channel at an averaged velocity of 0.5 m/s and its trajectories are recorded. The experiment is numerically reproduced on the basis of the LES model of turbulent channel flow described above (Yücesan et al., 2020).

6th IAHR Europe Congress
Warsaw Poland 2020

## 3. Results and discussion

### 3.1. Fall velocity in still water

The fall velocity of the spherical particles in still water is $v_s = 0.0688\,\text{ms}^{-1}$ according to an empirical equation developed by Dietrich (1982). The fall velocity of the same particles in the numerical model was $0.0706\,\text{ms}^{-1}$. The difference of only 2.5 % suggests that the model is capable of accurately reproducing the momentum exchange between the fluid and the particles.

The calibration to reproduce the settling behavior of particles in the experiment by Worf et al. (2019) resulted in a shape factor of 0.5 for a fall velocity of $0.075\,\text{ms}^{-1}$ in still water.

### 3.2. Development of the sediment plume in turbulent channel flow

Figure 1 displays the sediment plume after release into turbulent channel flow. A visual comparison of this image from the numerical model and a photograph of the physical model by Worf et al. (2019) shows that the development of the plume is similar in the numerical and physical model. The only difference between the two models is a higher spread of particles in the physical model, probably due to higher particle variety.

The results are quantitatively analyzed based on $(x, y)$ positions of the particles 0.2 s after sediment supply has stopped. The fall velocity of the particles in turbulent channel flow can be calculated as the product of the slope of the regression line of the $(x, y)$ positions of the particles and the average fluid flow velocity (Worf et al., 2019). Using this method Worf et al. (2019) measured a fall velocity in the range of $0.03\,\text{ms}^{-1}$ to $0.06\,\text{ms}^{-1}$ for particles with a diameter of $0.5\,\text{mm} < D_n < 0.71\,\text{mm}$ in turbulent channel flow with an average flow velocity of $0.5\,\text{ms}^{-1}$. The fall velocity in the numerical simulation of this experiment is $0.06\,\text{ms}^{-1}$.

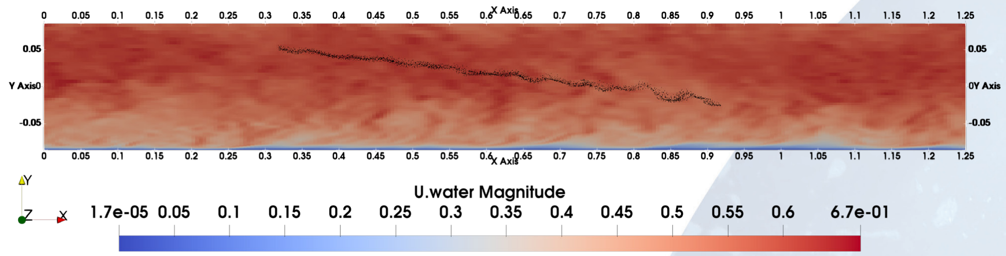


**Fig. 1.** Sediment release into turbulent channel flow (length in m, velocity in $\text{ms}^{-1}$)

## 4. Conclusions

The study shows the feasibility of a highly accurate model of suspended sediment transport in turbulent channel flow using an LES model for fluid flow together with two way coupled Lagrangian particle tracking. In the next step, the model shall be used to study the development of a sediment plume after dumping of fine sediment into a river. This way the inaccuracy of the advection-diffusion equation to model sediment transport in the immediate area where dumping is taking place (cf. e.g. Haimann et al., 2018) can be overcome.

**Acknowledgements**

This paper was written as a contribution to the Christian Doppler Laboratory for Sediment Research and Management. In this context, the financial support by the Christian Doppler Research Association, the Austrian Federal Ministry for Digital and Economic Affairs and the National Foundation for Research, Technology and Development is gratefully acknowledged. The computational results presented have been achieved using the Vienna Scientific Cluster (VSC).

**References**

Dietrich WE (1982) Settling velocity of natural particles, Water Resources Research, 18(6), 1615-1626
Greenshields CJ (2018) OpenFOAM User Guide version 6, The OpenFOAM Foundation Ltd, 237 pp.
Haider A, Levenspiel O (1989) Drag coefficient and terminal velocity of spherical and nonspherical particles, Powder Technology, 58(1), 63–70
Haimann M, Hauer C, Tritthart M, Prenner D, Leitner P, Moog O, Habersack H (2018) Monitoring and modelling concept for ecological optimized harbour dredging and fine sediment disposal in large rivers, Hydrobiologia, 814(1), 89-105
Hauer C, Wagner B, Aigner J, Holzapfel P, Flödl P, Liedermann M, Tritthart M, Sindelar C, Pulg U, Klösch M, Haimann M, Donnum BO, Stickler M, Habersack H (2018) State of the art, shortcomings and future challenges for a sustainable sediment management in hydropower: A review, Renewable and Sustainable Energy Reviews, 98, 40–55
Worf D, Schobesberger J, Lichtneger P, Habersack H, Sindelar C (2019) Sedimentation velocity of Saualm crystalline using image processing methods, 16th International Symposium on Water Management and Hydraulic Engineering (Skopje, North Macedonia)
Yücesan S, Schobesberger J, Sindelar C, Hauer C, Habersack H, Tritthart M (2020) Large Eddy Simulation of a Sediment Particle under Entrainment Conditions, Journal of Hydraulic Research (submitted)

## 5.3 IAHR World (2022): “Variability of Shape and Extent of a Sediment Plume in a two-way Coupled LES Model Using an Euler-Lagrange Approach” (in print)

International Association for Hydro-Environment Engineering and Research

Hosted by Spain Water and IWHR, China

39th IAHR WORLD CONGRESS GRANADA, SPAIN 2022 From Snow to Sea 19-24 June 2022

| | |
|---|---|
| Event: | 39th IAHR World Congress “From Snow to Sea” |
| Venue: | Granada, Spain |
| Date: | 19 – 24 June 2022 |
| Authors: | Daniel Wildt, Christoph Hauer, Helmut Habersack and Michael Tritthart |
| Paper number (ID): | 594 |
| Submitted: | 31st January 2022 |
| Accepted: | 29th March 2022 |

39th IAHR WORLD CONGRESS GRANADA, SPAIN 2022 From Snow to Sea 19-24 June 2022

Proceedings of the 39th IAHR World Congress
19-24 June
2022 Granada, Spain
DOI number

# Variability of Shape and Extent of a Sediment Plume in a two-way Coupled LES Model Using an Euler-Lagrange Approach

Daniel Wildt[1], Christoph Hauer[2], Helmut Habersack[3] and Michael Tritthart[4]
[1,2] Christian Doppler Laboratory for Sediment Research and Management, University of Natural Resources and Life Sciences, Vienna, Vienna, Austria
e-mail: daniel.wildt@boku.ac.at; christoph.hauer@boku.ac.at
[1,2,3,4] University of Natural Resources and Life Sciences, Vienna, Department of Water, Atmosphere and Environment, Institute of Hydraulic Engineering and River Research, Vienna, Austria
e-mail: helmut.habersack@boku.ac.at; michael.tritthart@boku.ac.at

**Abstract**

Large-eddy simulations of a sediment plume in turbulent channel flow differing in arbitrary fluctuations in the initial fluid velocity field are discussed. Results show dependence of the development of the sediment plume based on these turbulent velocity fluctuations. Differences between maximum and minimum streamwise extents of the sediment plume can amount up to 50% of the length of the sediment plume. Extreme cases selected based on maximum and minimum extents of the sediment plume are compared. Shape and extents are related to instantaneous fluid velocities in the area of the sediment plume, visualized using quadrant analysis.

**Keywords:** *Computational fluid dynamics; Large-eddy simulation; Lagrangian particle tracking; Sediment plume; River.*

## 1. INTRODUCTION

Sediment plumes are developing in rivers in consequence of sediment management practices in which dumping is involved (Hauer et al., 2018). For instance, sediment from harbor dredging is dumped downstream into the river (Haimann et al., 2018). Information and process understanding of the development of the sediment plume after dumping is crucial for several reasons. The efficiency of the measure can be improved by models capable of predicting sediment transport after dumping (Paarlberg et al., 2015). In addition, environmental impact of sediment dumping can be reduced using a prediction tool for the development of the sediment plume (Hauer et al., 2018; Haimann et al., 2018).

Wildt et al. (2022) set up a large eddy simulation of turbulent channel flow which is two-way coupled with a Lagrangian model of sediment transport. Based on results of 41 simulations which are identical apart from the arbitrary turbulence structures in the initial flow fields they analyzed the processes during the development of the sediment plume immediately after dumping. They observed considerable influence of the initial turbulence field on the development of the sediment plume. The aim of the present study is to work out and discuss this influence based on the simulation results from Wildt et al. (2022).

## 2. METHODOLOGY

### 2.1. Governing Equations

The model of the sediment plume set up by Wildt et al. (2022) is comprised of two components. Sediment transport is modelled using a Lagrangian approach. Particle acceleration is calculated based on Newtons' law of motion. Fluid-particle interaction forces are described by the Maxey-Riley equation (Maxey and Riley, 1983). Forces implemented in the model include (i) lift $\boldsymbol{F_L}$ and drag $\boldsymbol{F_D}$ forces, (ii) added mass forces $\boldsymbol{f_{am}}$, (iii) pressure gradient force, (iv) gravitational forces and (v) interparticle stress. The latter is treated in a lumped manner through a stress tensor $\tau$ computed using an approach by Lun et al. (1984) for which particle properties are mapped to an Eulerian grid (Snider, 2001).

$$\frac{\mathrm{d}\boldsymbol{v}}{\mathrm{d}t} = \boldsymbol{F_D} + \boldsymbol{F_L} + \boldsymbol{f_{am}} - \frac{1}{\rho_s}\nabla p + \boldsymbol{g} - \frac{1}{\Theta\rho_s}\nabla\boldsymbol{\tau} \qquad [1]$$

$\boldsymbol{v}$ is the particle velocity, $t$ time, $\rho_s = 2650\,\mathrm{kgm^{-3}}$ particle density, $p$ pressure and $\boldsymbol{g}$ acceleration due to gravity. The particle volume fraction $\Theta$ and the fluid volume fraction $\alpha$, respectively can be derived from the particle distribution function $f$ by the following equation (Andrews and O'Rouke, 1996).

Proceedings of the 39th IAHR World Congress
19-24 June 2022, Granada, Spain

$$\Theta = \int \int f \frac{m}{\rho_s} \mathrm{d}m\boldsymbol{v} \qquad [2]$$

$$\alpha + \Theta = 1 \qquad [3]$$

Particle fluid momentum coupling is implemented through the Multiphase Particle-In-Cell (MP-PIC) algorithm (Andrews and O'Rourke, 1996). The algorithm builds on the particle distribution function $f$ which is transported through the domain by the following function (Andrews and O'Rourke, 1996).

$$\frac{\partial f}{\partial t} + \nabla_{\boldsymbol{x}} \cdot (f\boldsymbol{v}) + \nabla_{\boldsymbol{v}} \cdot \left(f \frac{\mathrm{d}\boldsymbol{v}}{\mathrm{d}t}\right) = \left(\frac{\partial f}{\partial t}\right)_{\mathrm{coll}} \qquad [4]$$

This allows the following formulation of mass (Eq. [5]) and momentum (Eq. [6]) continuity using the incompressible Navier-Stokes equations for the fluid phase (Andrews and O'Rourke, 1996).

$$\frac{\partial \alpha}{\partial t} + \nabla \cdot (\alpha \boldsymbol{u}) = 0 \qquad [5]$$

$$\frac{\partial \alpha \boldsymbol{u}}{\partial t} + \nabla \cdot (\alpha \boldsymbol{u}\boldsymbol{u}) = \nabla \cdot (\nu_{\mathrm{eff}} \nabla \cdot \boldsymbol{u}) + \frac{1}{\rho} \cdot \nabla p + \frac{\boldsymbol{F}}{\rho} \qquad [6]$$

$\boldsymbol{u}$ is the fluid velocity, $\nu_{\mathrm{eff}}$ the sum of the kinematic viscosity $\nu = 1.17$ $\mathrm{m^2 s^{-1}}$ and the subgrid scale turbulent viscosity from the Smagorinsky turbulence model (Smagorinsky, 1963) and $\rho = 1000\,\mathrm{kgm^{-3}}$ the fluid density. Interaction forces $\boldsymbol{F}$ from the particulate phase come into the equation via the source term on the right-hand side. The PISO algorithm is used for pressure coupling (Wildt et al., 2022).

The Eulerian equations are solved on structured mesh with more than 5.5 Mio hexahedral cells. Solvers of the open-source package OpenFOAM (Greenshields, 2018) are used.

### 2.2. Simulation set-up

Cyclic boundary conditions are applied at inlet and outlet as well as at the lateral walls of the rectangular channel. A no-slip boundary condition is used for the bottom boundary and a symmetry boundary condition for the free surface. Bulk velocity in the initial flow field amounts to 0.5 $\mathrm{ms^{-1}}$ in $x$ direction. Based on a channel height of 0.17 m in $y$ direction the Reynolds number is 72,650. Initial conditions for the simulations of the sediment plume are retrieved from different time steps of the results of a precursor simulation modelling turbulent fluid flow only (Yücesan et al., 2022; Wildt et al., 2022).

Validation of the model was based on laboratory measurements of fall velocity of particles in standing water as well as in turbulent channel flow carried out by Worf et al. (2019). Comparison of the experimentally determined fall velocities with those from the numerical model showed good agreement (Wildt et al., 2021; Wildt et al., 2022).

For the study of the development of the sediment plume 6859 particles were placed into the channel. The particles were initially arranged in a grid of 2 cm edge length in the top left corner of the channel (see also Figure 1). Particle diameters range from 0.07 mm to 0.71 mm covering theoretical fall velocities of 0.003 $\mathrm{ms^{-1}}$ to 0.059 $\mathrm{ms^{-1}}$ according to the equation by Haider and Levenspiel (1989) (shape factor 0.45; Wildt et al., 2022).

## 3. RESULTS AND DISCUSSION

Figure 1 displays the development of the sediment plume after release of the sediment into turbulent fluid flow from one exemplary simulation. The plot shows how the sediment plume is taken up by the flow and transported along the channel. The shape of the plume is distorted due to turbulent dispersion effects. As a result of the differing fall velocities due to the range of particle diameters in the simulations, the sediment plume is additionally stretched in direction of gravity (Wildt et al., 2022).

Although the processes identified in Figure 1 from the results of one exemplary simulation can be observed in each result of the 41 simulations, their specific manifestation can vary between the individual simulations. Figure 2 shows the shape of the sediment plume 0.5 s and 1.0 s after release of the sediment in selected simulations. The simulations differ only in the arbitrary initial turbulent fluid velocity field. Simulations of which results are displayed in Figure 2 are those in which the sediment plume reached furthest and least far in streamwise and vertical direction (see also Table 1).

Proceedings of the 39th IAHR World Congress
19-24 June 2022, Granada, Spain

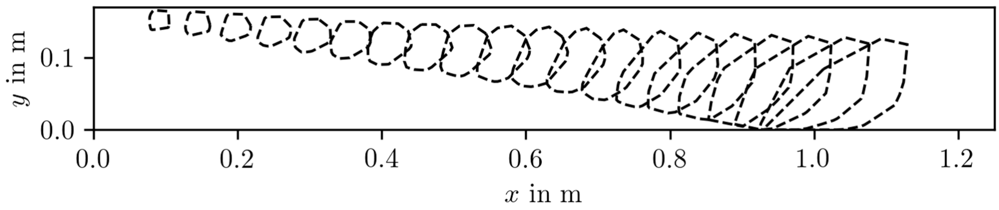


**Figure 1**. Shape and position of the sediment plume in 0.1 s time intervals after release of the sediment into turbulent fluid flow (case F).

**Table 1**. Description of the selected extreme cases based on the extent 0.5 s after release of the sediment

| Case | Description | Legend for Fig. 2 |
|---|---|---|
| A | highest extent in negative $x$ | solid blue |
| B | highest extent in positive $x$ | dashed, orange |
| C | highest extent in positive and negative $y$ | dotted, green |
| D | smallest extent in positive $x$ | dash-dotted, red |
| E | smallest extent in negative $x$ | solid, purple |
| F | smallest extent in positive $y$ | dashed, brown |
| G | smallest extent in negative $y$ | dotted, pink |

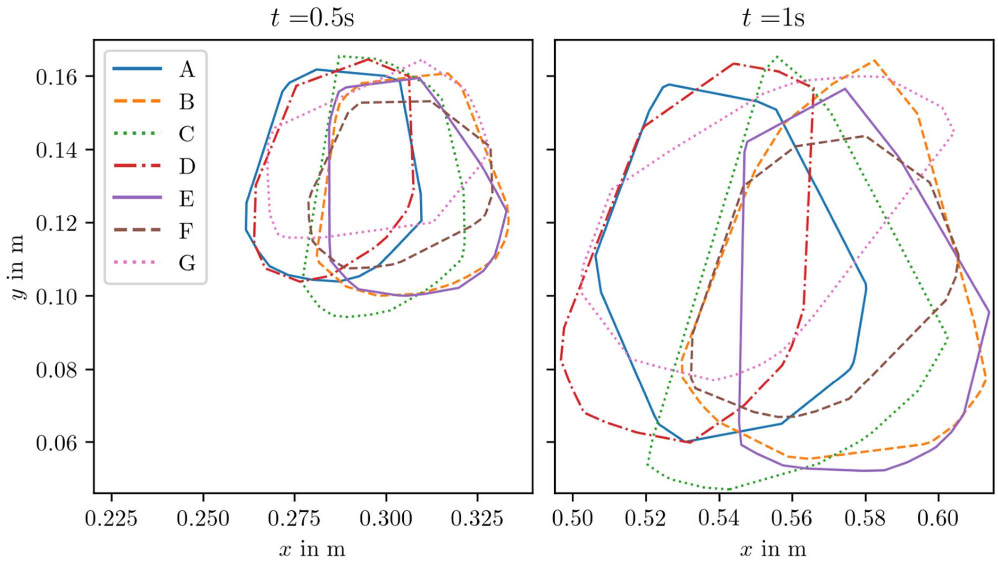


**Figure 2**. Shape of the sediment plume from selected simulations started with different initial turbulent flow fields 0.5 s and 1.0 s after release of the sediment into the flow. For description of the cases A to G see Table 1.

Figure 2 shows that extents of the sediment plumes vary substantially in $x$ and negative $y$ direction. For the streamwise direction the difference of the extents of the sediment plume can amount to up to 50% of the length of the sediment plume. Maximum extents in positive $y$ direction are not varying as much as they vary in the other directions. One reason for this is that the sediment cannot move above the water surface and hence the dispersion is limited in this direction.

The earlier time step in Figure 2 represents a situation right after the initial acceleration of the sediment plume. The latter time step displays a situation from the transport phase. Although some differences in the shape and extent of the sediment plumes can be noticed, their general positions at the two time steps displayed

Proceedings of the 39th IAHR World Congress
19-24 June 2022, Granada, Spain

in Figure 2 are similar. At both time steps A and D have been transported least far while B, E and F are located at higher $x$ coordinates. In addition, C is stretched longest in vertical direction at both time steps displayed in Figure 2. This suggests that the variation in extents and shape of the sediment plumes is mainly a result of the acceleration phase.

Quadrant analysis is used in Figures 3 and 4 to discuss the effect of instantaneous turbulent velocity fields 0.5 s after release of the sediment on shape and position of the sediment plume. The relative position of the point cloud representing fluid velocity fluctuations in cells with particles present and the dashed polygon representing clear fluid velocity fluctuations in the same cells is similar in all runs. This comparison enables to distinguish influence of particles on fluid flow from arbitrary turbulent velocity fluctuations. The averaged influence of particles on fluid flow can be observed in the bottom-right panel of Figure 3. It shows the quadrant analysis of the streamwise and vertical fluid velocity differences between time averaged clear water flow and the average of the 41 simulations of the sediment plume. The plot shows the slow-down of the fluid velocity in streamwise direction and the downward acceleration of fluid velocities due to the presence of sediment (Wildt et al., 2022).

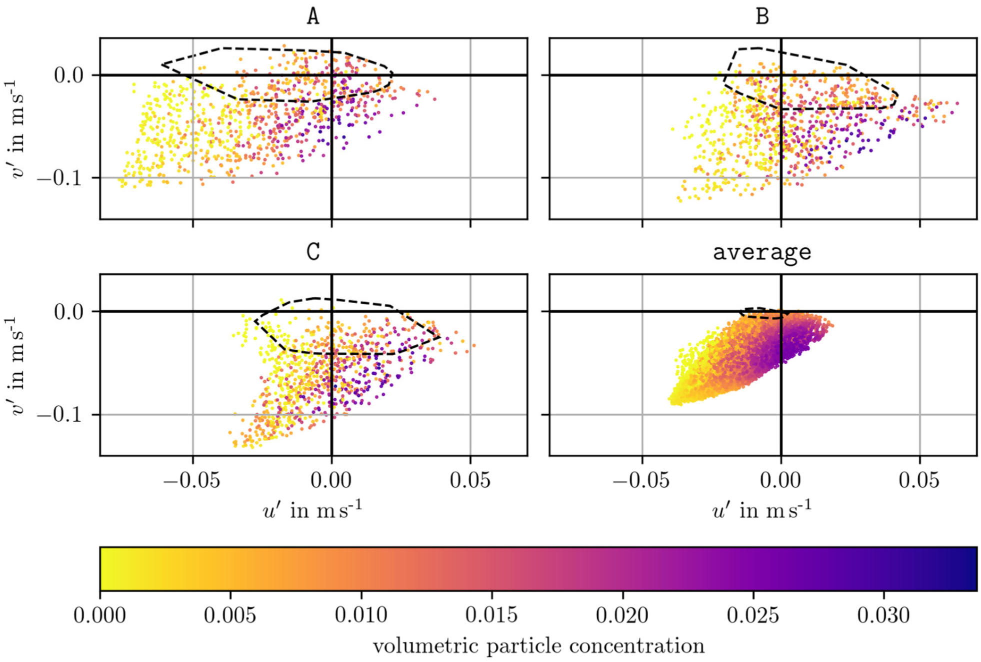


**Figure 3**. Quadrant analysis for cells with particles present 0.5 s after release of the sediment plume for cases with highest extent in positive and negative streamwise and vertical direction (see also Table 1). Points show velocity fluctuations of cells with particles present, dashed black polygons show velocity fluctuations of clear water flow in the same area. The bottom right panel displays the quadrant analysis averaged for all 41 simulations carried out by Wildt et al. (2022).

Relatively high streamwise velocities have occurred in run B (Figure 3) and E (Figure 4). Thus, in those simulations the sediment plume has reached furthest in streamwise direction (highest extent in positive $x$ and lowest extent in negative $x$; see Table 1 and Figure 2). Run G (Figure 4) has the lowest negative vertical velocity fluctuations. Hence the low downward extent of the sediment plume in this simulation can be explained. Only a small number of particles in regions with positive vertical velocity fluctuations are visible in the quadrant analysis of run F (Figure 4). Although other simulations have a similarly low number of particles in areas of upward turbulent velocity fluctuations this simulation has the smallest extent in positive $y$ direction. It is expected that particles in areas of upward moving fluid in this particular simulation are mainly large particles with high fall velocities. They are moving downward despite the upward moving surrounding fluid. Finally, the extension of the sediment plume is largest in positive and negative $y$ direction in run C. This simulation has regions with highest downward fluid velocities (Figure 3).

Proceedings of the 39th IAHR World Congress
19-24 June 2022, Granada, Spain

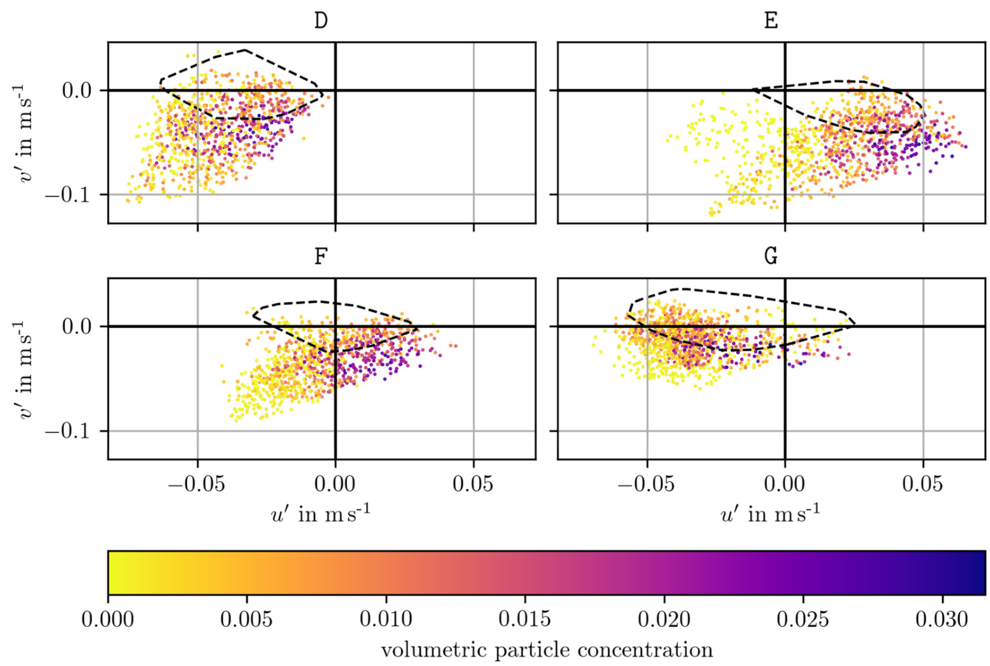


**Figure 4**. Quadrant analysis for cells with particles present 0.5 s after release of the sediment plume for cases with lowest extent in positive and negative streamwise and vertical direction (see also Table 1). Points show velocity fluctuations of cells with particles present, dashed black polygons show velocity fluctuations of clear water flow in the same area.

## 4. CONCLUSIONS

Large-eddy simulations of a sediment plume in turbulent fluid flow show considerable dependence of the development of the sediment plume on the initial turbulent fluid velocity field. Although certain processes can be worked out concerning the general development of the sediment plume the maximum extents of the sediment plumes can differ in streamwise direction up to 50% of the length of the sediment plume. In vertical direction variability can predominantly be observed in the downward extents of the sediment plumes. This is mainly because the extent of the sediment plume is limited in upward direction by the water surface. A relation between the extents of the sediment plume and instantaneous fluid velocities in cells with particles present could be observed in a quadrant analysis.

## 5. ACKNOWLEDGEMENTS

The authors would like to thank Prof. Rui M.L. Ferreira for his valuable advice on particle–fluid momentum exchange as well as Dominik Worf for providing data for the validation of the numerical model. The computational results presented have been achieved using the Vienna Scientific Cluster (VSC). This paper was written as a contribution to the Christian Doppler Laboratory for Sediment Research and Management. In this context, the financial support by the Christian Doppler Research Association, Austria, the Austrian Federal Ministry for Digital and Economic Affairs and the National Foundation for Research, Technology and Development is gratefully acknowledged.

## 6. REFERENCES

Andrews, M., O'Rourke, P. (1996). The multiphase particle-in-cell (MP-PIC) method for dense particulate flows. *International Journal of Multiphase Flow* 22(2), 379-403. http://dx.doi.org/10.1016/0301-9322(95)00072-0
Greenshields, C.J. (2018). OpenFOAM. Edited by: OpenFOAM Foundation Ltd. User Guide Version 6. URL: http://openfoam.org

Proceedings of the 39th IAHR World Congress
19-24 June 2022, Granada, Spain

Haider, A. and Levenspield, O. (1989). Drag coefficient and terminal velocity of spherical and nonspherical particles. *Powder Technology* 58(1), 63-70. http://dx.doi.org/10.1016/0032-5910(89)80008-7

Haimann, M., Hauer, C., Tritthart, M., Prenner, D., Leitner, P., Moog, O. and Habersack, H. (2018). Monitoring and modelling concept for ecological optimized harbour dredging and fine sediment disposal in large rivers. *Hydrobiologia*. 814(1), 89-107. http://dx.doi.org/10.1007/s10750-016-2935-z.

Hauer, C., Wagner, B., Aigner, J., Holzapfel, P., Flödl, P., Liedermann, M., Tritthart, M., Sindelar, C., Pulg, U., Klösch, M., Haimann, M., Donnum, B.O., Stickler, M. and Habersack, H. (2018). State of the art, shortcomings and future challenges for a sustainable sediment management in hydropower: A review. *Renewable and Sustainable Energy Reviews,* 98, 40-55. http://dx.doi.org/10.1016/j.rser.2018.08.031.

Lun, C.K.K., Savage, S.B., Jeffrey, D.J. and Chepurniy, N. (1984). Kinetic theories for granular flow: inelastic particles in couette flow and slightly inelastic particles in a general flowfield. *Journal of Fluid Mechanics* 140. http://dx.doi.org/10.1017/S0022112084000586

Maxey, M. and Riley, J. (1983). Equation of motion for a small rigid sphere in a nonuniform flow. *Physics of Fluids* 26(4), 883-889. http://dx.doi.org/10.1063/1.864230

Paarlberg, A.J., Guerrero, M., Huthoff, F. and Re, M. (2015). Optimizing dredge-and-dump activities for river navigability using a hydro-morphodynamic model. *Water (Switzerland)* 7.7, 3943-3962. http://dx.doi.org/10.3390/w7073943

Smagorinsky, J. (1963). General circulation experiments with primitive equations: I. the basic experiment. *Monthly Weather Review* 91(3), 99-164. http://dx.doi.org/10.1175/1520-0493(1963)091<0099:GCEWTP> 2.3.CO;2.

Snider, D. (2001). An incompressible three-dimensional multiphase particle-in-cell model for dense particle flows. *Journal of Computational Physics* 170(2). 523-549. http://dx.doi.org/10.1006/jcph.2001.6747

Wildt, D., Yücesan, S., Hauer, C., Habersack, H. and Tritthart, M. (2021). LES two-phase modelling of suspended sediment transport using a two-way coupled Euler-Lagrange approach. In: 6th IAHR Europe Congress Abstract Book (Warsaw, Poland). Edited by: Kalinowska, M. p. 641 – 642. http://doi.org/10.24425/136660

Wildt, D., Hauer, C. Habersack, H. and Tritthart, M. (2022). LES two-phase modelling of suspended sediment transport using a two-way coupled Euler-Lagrange approach. *Advances in Water Resources* 160. https://doi.org/10.1016/j.advwatres.2021.104095

Worf, D., Schobesberger, J., Lichtneger, P., Habersack, H. and Sindelar, C. (2019). Sedimentation velocity of of Saualm crystalline using image processing methods. In: 16th International Symposium on Water Management and Hydraulic Engineering (Skopje, North Macedonia)

Yücesan, S., Schobesberger, J., Sindelar, C., Hauer, C., Habersack, H and Tritthart, M. (2022). Large eddy simulation of a sediment particle under entrainment conditions. Journal of Hydraulic Research (in press). https://doi.org/10.1080/00221686.2021.2022026

# Part III

# Summary and conclusions

# 6 Findings from the developed CFD models

Hydrodynamic and sediment transport CFD models have been set up on different scales. The RANS-solver RSim-3D (Tritthart, 2005; Tritthart and Gutknecht, 2007) has been extended for modelling particle-driven gravity currents in reservoirs (Section 4.1; Wildt et al., 2020). Application of the developed code for a real world reservoir still remains to be done as future work. Nevertheless results of the test cases presented show good agreement with experimental data. Thus it is expected that the developed code can be used as a strategic evaluation tool for planning sediment management measures in reservoirs, particularly venting of turbidity currents. Comparison of simulation results with and without the module accounting for buoyancy effects showed the strong influence of turbidity currents on sediment transport in reservoirs. This agrees well with literature (e. g. De Cesare et al., 2001).

Small-scale processes related to sediment transport in rivers were investigated using LES models. Time series of lift and drag forces on a sediment particle mounted to the channel bed were studied in Section 4.2 (Yücesan et al., 2021). Particular focus was put on the effect of particle exposure and its interaction with very large-scale turbulent motion. Results of this study show a bi-modal distribution of the premultiplied frequency spectra of the lift force on the particle at full exposure, but a unimodal distribution only at lower levels of exposure. This suggests that incipient motion of particles is strongly influenced by very large-scale turbulent structures.

Suspended sediment transport in turbulent channel flow has been studied using the second LES model in Section 4.3 (Wildt et al., 2022a). Momentum exchange between fluid and particles was two-way coupled using purely physical descriptions for all relevant interaction processes. In contrast to studies of suspended sediment transport previously published in literature, the investigated test case featured a fully transient process. Thus evaluation based on time averaged parameters was not possible. Sediment was initially placed in a small, confined part of the channel only. 41 runs of the model using different initial turbulent fluid velocity fields were averaged in order to distinguish relevant transport processes from arbitrary phenomena related to turbulence.

The reproducibility of numerical model results allowed a unique comparison of instantaneous turbulent fluid flow situations with and without the presence of particles. Analysis of individual simulation results enables a detailed investigation of different phenomena related to the effect of particles on fluid flow in certain regions. The variety of results from the different initial velocity fields were discussed in Section 5.3 (Wildt et al., 2022b). Further investigation of processes leading to this variety might enable additional insights into suspended sediment transport processes in future.

A number of processes related to the influence of sediment on fluid flow have been observed in the large scale RANS-model of particle-driven gravity currents (Section 4.1; Wildt et al., 2020) as well in the small scale LES-model of the development of a sediment plume (Section 4.3; Wildt et al., 2022a). In addition to the general formation of gravity currents, this also includes the influence of particle size on the particular development of the current. Small particles are forming a stronger turbidity current than large particles as more of their potential energy is available due to their lower fall velocity (Necker et al., 2002). Results of lock exchange experiments in Section 4.1 (Wildt et al., 2020) with large particles show a faster deceleration of the turbidity current compared to the respective experiments with fine particles. This phenomenon causes stratification of the sediment plume which has been observed in the LES-model in Section 4.3 (Wildt et al., 2022a).

Due to limited computational resources turbulence resolving models and detailed particle-fluid momentum coupling are in general not yet applicable to real world river engineering problems. Thus the effect of processes on small scales needs to be parametrized to be accounted for in large scale models of rivers and reservoirs. Three phases of the development of a sediment plume in turbulent channel flow have been defined based on the simulation results of the model in Section 4.3 (Wildt et al., 2022a). It is expected that different approaches for the parametrization of particle fluid interaction processes need to be applied for each of the phases:

1. In the *acceleration phase* initial acceleration of the sediment plume by the fluid through drag forces leads to a highly unsteady process. In addition a detailed analysis in the study in Section 5.3 (Wildt et al., 2022b) showed a high dependence of shape and extent of the sediment plume at the end of this phase on arbitrary turbulent velocity fluctuations. This suggests that a stochastic approach is most suitable for a parametrization of the development of the sediment plume in this phase.

2. Initial acceleration of the sediment plume has finished in the *transport phase*. Arbitrary turbulent velocity fluctuations showed lower influence on shape and extent of the sediment plume in the analysis in Section 5.3 (Wildt et al., 2022b). Parametrization of sediment transport in this phase can be implemented based on physical consideration of processes such as effects from stratification, change of viscosity and buoyancy effects (e. g. Section 4.1; Wildt et al., 2020).

3. When sediment approaches the channel bed in the *deposition phase* its transport is influenced by the wall. The shape of the sediment plume gets distorted due the wall normal velocity gradient. Interaction processes of sediment with the river bed including deposition and remobilization become relevant. This was also shown in an analysis of sediment deposition heights in the results of the RANS model in Section 4.1 (Wildt et al., 2020). Accurate results for sediment transport near the bed can only be achieved when transport as bed load is considered.

The findings from the study in Section 4.3 (Wildt et al., 2022a) should be used to improve Reynolds averaged simulations for more accurate simulations of the development of sediment plumes also on larger scales. Data of shape and extent of sediment plumes from small-scale, high fidelity models e. g. as displayed in Figure 9 in the study in Section 4.3 (Wildt et al., 2022a) can be used for inference of a stochastic model of sediment transport in the acceleration phase. Influence of different parameters on the development of the sediment plume can be tested using e. g. a Bayesian data analysis approach.

Efficient parametrization of particle-driven gravity currents to be accounted for in large-scale models of reservoirs has been achieved in the study in Section 4.1 (Wildt et al., 2020). Based on numerical simulations using the newly developed module, hydrodynamics and sediment transport driven by buoyancy effects inside a real world reservoir can be studied. This way e. g. the location of bottom outlets and timing of reservoir venting can be optimized.

It is expected that this code, despite initially developed for turbidity currents in reservoirs, can also be used to improve accuracy of models of a sediment plume in a river in the transport phase. In addition parametrizations developed based on time averaged simulations in literature can be used to improve RANS models of sediment transport in this phase. Examples are additional considerations for the diffusion coefficient in the advection-diffusion equation (e. g. Zhong et al., 2011) or the incorporation of the effect of particles on fluid turbulence into turbulence models (e. g. Hsu and P. Liu, 2004; Amoudry, 2014; Kranenburg et al., 2014, see Section 1.4).

Bed load transport, deposition and remobilization which are relevant in the deposition phase have so far been implemented into CFD models mainly using empirical equations based on time averaged parameters (see Section 1.2). Despite ongoing research investigating initiation of motion of bed load (see Section 1.3) an improved parametrization of this process remains difficult. As it can be seen from the results of the study in Section 4.2 (Yücesan et al., 2021) as well as similar studies in literature, accounting for turbulent motion is one important key to improve accuracy of bed load transport models.

# 7 Process scale and required model resolution

Despite large spatial extents of river reaches and reservoirs up to several kilometres inaccuracies occur in models averaging small scale processes. The above described definition of three phases of the development of a sediment plume can be related to scale issues in hydrological processes discussed by Blöschl and Sivapalan (1995).

The acceleration phase is characterized by high spatial and temporal dynamics. In consequence a high model resolution is necessary for an accurate representation of the processes in this phase. Those dynamics decrease in the transport phase. Hence processes can be aggregated. This is done e. g. by using an advection-diffusion equation for sediment transport or the source term in the fluid momentum equation accounting for buoyancy (Section 4.1; Wildt et al., 2020). In addition the reduction of the von Kármán constant (e. g. Nezu and Azuma, 2004; Ferreira, 2015; Cheng et al., 2018b) and turbulence models accounting for sediment load (e. g. Hsu and P. Liu, 2004; Amoudry, 2014; Kranenburg et al., 2014) are examples for possible parametrizations of influence of sediment on fluid flow in literature. Finally, in the deposition phase peaks of force and torque are relevant for particle entrainment. Upscaling through aggregation by averaging is not possible as extreme values get smoothed out (Blöschl and Sivapalan, 1995). This makes modelling sediment transport particularly difficult in this phase.

Glock et al. (2019) also carried out an analysis of the effect of resolution of numerical models of rivers. They compared results of a 1D, 2D and 3D model. Water depth could be represented with all three models. Accurate aggregation of three-dimensional processes in the 2D and 1D model has been achieved through calibration of relevant parameters as e. g. the roughness coefficient. Despite this, bed shear stress differed substantially between the three models. This shows that while individual processes can be aggregated for large-scale models accuracy may be lost for sub-processes or related processes.

Similarly to the findings of Glock et al. (2019) it is expected from the results of the research carried out in the course of this thesis that upscaling through process aggregation reduces the generality of model results. This highlights the importance of model calibration and validation with respect to parameters which are later analysed in the simulation results (Roache, 2009). Particularly when large-scale models are used it should be avoided to analyse parameters which have not been validated directly, i. e. are only derived from validated parameters.

With regard to field measurements and laboratory experiments numerical modelling has advantages as it enables to fulfil the objective stated by Blöschl and Sivapalan (1995) that a process should be modelled or observed at its process scale. This applies to all three definitions of observation scale:

1. In a numerical model a process can be observed at its entire spatial and temporal extent;
2. The required discretization for the numerical solution of the equations is usually finer than the relevant spacing of the process;
3. A finite number of samples is not necessary as detailed information exists over the entire extent (Blöschl and Sivapalan, 1995).[1]

[1]This part has been worked out in the module “Principles and challenges of research in socio-economics, natural resources and life sciences” (SE 940.401) completed as part of the PhD project.

# References

Ackers, P. and W. R. White (1973). 'Sediment transport: new approach and analysis'. In: *Proceedings of the American Scociety of Civil Engineers, Journal of the Hydraulics Division*. Vol. 99, pp. 2041–2060.

Amir, M., V. I. Nikora and M. T. Stewart (2014). 'Pressure forces on sediment particles in turbulent open-channel flow: a laboratory study'. *Journal of Fluid Mechanics* 757, pp. 458–497. DOI: 10.1017/jfm.2014.498.

Amoudry, L. O. (2014). 'Extension of k-omega turbulence closure to two-phase sediment transport modelling: Application to oscillatory sheet flows'. *Advances in Water Resources* 72, pp. 110–121. ISSN: 0309-1708. DOI: 10.1016/j.advwatres.2014.07.006.

An, S. and P. Y. Julien (2014). 'Three-dimensional modeling of turbid density currents in Imha Reservoir, South Korea'. *Journal of Hydraulic Engineering* 140 (5). ISSN: 0733-9429. DOI: 10.1061/(ASCE)HY.1943-7900.0000851.

An, S., P. Y. Julien and S. K. Venayagamoorthy (2012). 'Numerical simulation of particle-driven gravity currents'. *Environmental Fluid Mechanics* 12, pp. 495–513. ISSN: 1567-7419. DOI: 10.1007/s10652-012-9251-6.

Andrews, M. and P. O'Rourke (1996). 'The multiphase particle-in-cell (MP-PIC) method for dense particulate flows'. *International Journal of Multiphase Flow* 22 (2), pp. 379–402. ISSN: 0301-9322. DOI: 10.1016/0301-9322(95)00072-0.

Auel, C. (2014). *Flow characteristics, particle motion and invert abrasion in sediment bypass tunnels*. Ed. by R. M. Boes. Vol. 229. Mitteilungen. Zurich, Switzerland: Versuchsanstalt für Wasserbau, Hydrologie und Glaziologie (VAW) der Eidgenössischen Technischen Hochschule Zürich (ETH). 320 pp.

Baas, J. H., W. Van Kesteren and G. Postma (2004). 'Deposits of depletive high-density turbidity currents: a flume analogue of bed geometry, structure and texture'. *Sedimentology* 51 (5), pp. 1053–1088. DOI: 10.1111/j.1365-3091.2004.00660.x.

Blöschl, G. and M. Sivapalan (1995). 'Scale issues in hydrological modelling: A review'. *Hydrological Processes* 9 (3–4), pp. 251–290. DOI: 10.1002/hyp.3360090305.

Boes, R., C. Auel, M. Müller-Hagmann and I. Albayrak (2014). 'Sediment bypass tunnels to mitigate reservoir sedimentation and restore sediment continuity'. In: *Reservoir Sedimentation*. Ed. by A. J. Schleiss, G. de Cesare, M. J. Franca and M. Pfister. 1st ed. London, United Kingdom: Taylor & Francis Group, pp. 221–228. ISBN: 978-1-138-02675-9. DOI: 10.1201/b17397-27.

Bonnecaze, R. T., H. E. Huppert and J. R. Lister (1993). 'Particle-driven gravity currents'. *Journal of Fluid Mechanics* 250, pp. 339–369. DOI: 10.1017/S002211209300148X.

Canelas, R., A. Crespo, J. Domínguez, R. Ferreira and M. Gómez-Gesteira (2016). 'SPH-DCDEM model for arbitrary geometries in free surface solid-fluid flows'. *Computer Physics Communications* 202, pp. 131–140. ISSN: 0010-4655. DOI: 10.1016/j.cpc.2016.01.006.

Canelas, R., J. Domínguez, A. Crespo, M. Gómez-Gesteira and R. Ferreira (2017). 'Resolved simulation of a granular-fluid flow with a coupled SPH-DCDEM model'. *Journal of Hydraulic Engineering* 143 (9). ISSN: 0733-9429. DOI: 10.1061/(ASCE)HY.1943-7900.0001331.

Cantero, M. I., S. Balachandar and M. H. García (2008a). 'An Eulerian–Eulerian model for gravity currents driven by inertial particles'. *International Journal of Multiphase Flow* 34 (5), pp. 484–501. ISSN: 0301-9322. DOI: 10.1016/j.ijmultiphaseflow.2007.09.006.

Cantero, M. I., M. García and S. Balachandar (2008b). 'Effect of particle inertia on the dynamics of depositional particulate density currents'. *Computers and Geosciences* 34 (10), pp. 1307–1318. ISSN: 0098-3004. DOI: 10.1016/j.cageo.2008.02.002.

Celik, A. O., P. Diplas, C. L. Dancey and M. Valyrakis (2010). 'Impulse and particle dislodgement under turbulent flow conditions'. *Physics of Fluids* 22 (4). DOI: 10.1063/1.3385433.

Celik, A. O., P. Diplas and C. L. Dancey (2013). 'Instantaneous turbulent forces and impulse on a rough bed: Implications for initiation of bed material movement'. *Water Resources Research* 49 (4), pp. 2213–2227. DOI: 10.1002/wrcr.20210.

Chamoun, S., G. De Cesare and A. J. Schleiss (2016). 'Managing reservoir sedimentation by venting turbidity currents: A review'. *International Journal of Sediment Research* 31 (3), pp. 195–204. ISSN: 1001-6279. DOI: 10.1016/j.ijsrc.2016.06.001.

Chamoun, S., G. De Cesare and A. J. Schleiss (2017). 'Management of turbidity current venting in reservoirs under different bed slopes'. *Journal of Environmental Management* 204.1, pp. 519–530. ISSN: 0301-4797. DOI: 10.1016/j.jenvman.2017.09.030.

Chamoun, S., G. De Cesare and A. J. Schleiss (2018a). 'Influence of operational timing on the efficiency of venting turbidity currents'. *Journal of Hydraulic*

*Engineering* 144 (9). ISSN: 0733-9429. DOI: 10.1061/(ASCE)HY.1943-7900.0001508.

Chamoun, S., G. De Cesare and A. J. Schleiss (2018b). 'Venting of turbidity currents approaching a rectangular opening on a horizontal bed'. *Journal of Hydraulic Research* 56 (1), pp. 44–58. ISSN: 0022-1686. DOI: 10.1080/00221686.2017.1289266.

Chan-Braun, C., M. García-Villalba and M. Uhlmann (2013). 'Spatial and temporal scales of force and torque acting on wall-mounted spherical particles in open channel flow'. *Physics of Fluids* 25 (7). DOI: 10.1063/1.4813806.

Chan-Braun, C., M. García-Villalba and M. Uhlmann (2011). 'Force and torque acting on particles in a transitionally rough open-channel flow'. *Journal of Fluid Mechanics* 684, pp. 441–474. DOI: 10.1017/jfm.2011.311.

Cheng, Z., J. Chauchat, T.-J. Hsu and J. Calantoni (2018a). 'Eddy interaction model for turbulent suspension in Reynolds-averaged Euler-Lagrange simulations of steady sheet flow'. *Advances in Water Resources* 111, pp. 435–451. ISSN: 0309-1708. DOI: 10.1016/j.advwatres.2017.11.019.

Cheng, Z., T.-J. Hsu and J. Calantoni (2017). 'SedFoam: A multi-dimensional Eulerian two-phase model for sediment transport and its application to momentary bed failure'. *Coastal Engineering* 119, pp. 32–50. ISSN: 0378-3839. DOI: 10.1016/j.coastaleng.2016.08.007.

Cheng, Z., T.-J. Hsu and J. Chauchat (2018b). 'An Eulerian two-phase model for steady sheet flow using large-eddy simulation methodology'. *Advances in Water Resources* 111, pp. 205–223. ISSN: 0309-1708. DOI: 10.1016/j.advwatres.2017.11.016.

Crespo, A., J. Domínguez, B. Rogers, M. Gómez-Gesteira, S. Longshaw, R. Canelas, R. Vacondio, A. Barreiro and O. García-Feal (2015). 'DualSPHysics: Open-source parallel CFD solver based on smoothed particle hydrodynamics (SPH)'. *Computer Physics Communications* 187, pp. 204–216. ISSN: 0010-4655. DOI: 10.1016/j.cpc.2014.10.004.

Dallali, M. and V. Armenio (2015). 'Large eddy simulation of two-way coupling sediment transport'. *Advances in Water Resources* 81, pp. 33–44. ISSN: 0309-1708. DOI: 10.1016/j.advwatres.2014.12.004.

De Cesare, G., A. Schleiss and F. Hermann (2001). 'Impact of turbidity currents on reservoir sedimentation'. *Journal of Hydraulic Engineering* 127 (1), pp. 6–16. ISSN: 0733-9429. DOI: 10.1061/(ASCE)0733-9429(2001)127:1(6).

De Rooij, F. and S. B. Dalziel (2001). 'Time- and space-resolved measurements of deposition under turbidity currents'. In: *Particulate Gravity Currents*. 31. Oxford, United Kingdom: Blackwell Science Ltd., pp. 207–215. ISBN: 0-632-05921-4. DOI: 10.1002/9781444304275.ch15.

Deltares (2014). *Delft3D-FLOW. Simulation of multi-dimensional hydrodynamic flows and transport phenomena, including sediments*. Hydro-Morphodynamics. User Manual. Version 3.15.34158. Delft, The Netherlands.

Diplas, P., C. L. Dancey, A. O. Celik, M. Valyrakis, K. Greer and T. Akar (2008). 'The role of impulse on the Initiation of particle movement under turbulent flow conditions'. *Science* 322 (5902), pp. 717–720. ISSN: 0036-8075. DOI: 10.1126/science.1158954.

Druzhinin, O. A. (1995). 'Dynamics of concentration and vorticity modification in a cellular flow laden with solid heavy particles'. *Physics of Fluids* 7 (9), pp. 2132–2142. DOI: 10.1063/1.868756.

Du Boys, M. (1879). 'Le Rhone et les rivières a lit affouillable'. *Annales des Ponts et Chaussees* 49.

Dwivedi, A., B. W. Melville, A. Y. Shamseldin and T. K. Guha (2010). 'Drag force on a sediment particle from point velocity measurements: A spectral approach'. *Water Resources Research* 46 (10). DOI: 10.1029/2009WR008643.

Dwivedi, A., B. W. Melville, A. Y. Shamseldin and T. K. Guha (2011). 'Analysis of hydrodynamic lift on a bed sediment particle'. *Journal of Geophysical Research: Earth Surface* 116 (F2). DOI: 10.1029/2009JF001584.

Einstein, H. A. and Ning Chien (1955). *Effects of heavy sediment concentration near the bed on velocity and sediment distribution*. 8. Berkeley, California: University of California, Institute of Engineering Research.

Einstein, H. A. (1950). 'The bed-Load function for sediment transport in open channel flows'. In: *Technical Bulletin*. 1026. Washington, D.C.: United States Department of Agriculture, Soil Conservation Service.

Elghannay, H. and D. Tafti (2018a). 'LES-DEM simulations of sediment transport'. *International Journal of Sediment Research* 33 (2), pp. 137–148. ISSN: 1001-6279. DOI: 10.1016/j.ijsrc.2017.09.006.

Elghannay, H. and D. Tafti (2018b). 'Sensitivity of numerical parameters on DEM predictions of sediment transport'. *Particulate Science and Technology* 36 (4), pp. 438–446. ISSN: 02726351. DOI: 10.1080/02726351.2017.1352638.

Engelund, F. and E. Hansen (1967). *A monograph on sediment transport in alluvial streams*. Hydraulic Engineering Reports. Copenhagen, Denmark: Tekniskforlag. URL: http://resolver.tudelft.nl/uuid:81101b08-04b5-4082-9121-861949c336c9.

Esmaeili, T., T. Sumi, S. A. Kantoush, Y. Kubota, S. Haun and N. Ruther (2017). ‘Three-dimensional numerical study of free-flow sediment flushing to increase the flushing efficiency: A case-study reservoir in Japan’. *Water (Switzerland)* 9 (11). ISSN: 2073–4441. DOI: 10.3390/w9110900.

European Comission (2000). *Directive 2000/60/EC, The EU Water Framework Directive – integrated river basin management for Europe.*

Fan, J.-H. (1960). ‘Experimental studies on density currents’. *Scientia Sinica* (2), pp. 275–303. DOI: 10.1360/ya1960-9-2-275.

Ferreira, R. (2015). ‘The von Kármán constant for flows over rough mobile beds. Lessons learned from dimensional analysis and similarity’. *Advances in Water Resources* 81, pp. 19–32. ISSN: 0309-1708. DOI: 10.1016/j.advwatres.2014.10.004.

Ferziger, J. H. and M. Perić (2002). *Computational methods for fluid dynamics.* 3rd ed. Berlin, Germany: Springer-Verlag. 423 pp. ISBN: 3-540-42074-6.

Gaeuman, D., E. D. Andrews, A. Krause and W. Smith (2009). ‘Predicting fractional bed load transport rates: Application of the Wilcock-Crowe equations to a regulated gravel bed river’. *Water Resources Research* 45 (6). DOI: 10.1029/2008WR007320.

Georgoulas, A., P. Angelidis, T. Panagiotidis and N. Kotsovinos (2010). ‘3D Numerical modelling of turbidity currents’. *Environmental Fluid Mechanics* 10, pp. 603–635. ISSN: 15677419. DOI: 10.1007/s10652-010-9182-z.

Gladstone, C., J. C. Phillips and R. S. J. Sparks (1998). ‘Experiments on bidisperse, constant-volume gravity currents: propagation and sediment deposition’. *Sedimentology* 45 (5), pp. 833–843. DOI: 10.1046/j.1365-3091.1998.00189.x.

Glock, K., M. Tritthart, H. Habersack and C. Hauer (2019). ‘Comparison of hydrodynamics simulated by 1D, 2D and 3D models focusing on bed shear stresses’. *Water (Switzerland)* 11 (2). ISSN: 2073-4441. DOI: 10.3390/w11020226.

Greenshields, C. J. (2018). *OpenFOAM.* Ed. by OpenFOAM Foundation Ltd. User Guide. Version 6. URL: http://openfoam.org.

Greimann, B. P., M. Muste and F. M. H. Jr. (1999). ‘Two-phase formulation of suspended sediment transport’. *Journal of Hydraulic Research* 37 (4), pp. 479–500. DOI: 10.1080/00221686.1999.9628264.

Habersack, H., K. Bogner, J. Schneider and M. Brauner (2000). 'Catchment-wide analysis of the sediment regime with respect to reservoir sedimentation'. *International journal of sediment research* 16 (2), pp. 159–169. ISSN: 1001-6279.

Haimann, M., C. Hauer, M. Tritthart, D. Prenner, P. Leitner, O. Moog and H. Habersack (2018). 'Monitoring and modelling concept for ecological optimized harbour dredging and fine sediment disposal in large rivers'. *Hydrobiologia* 814, pp. 89–107. ISSN: 1573-5117. DOI: 10.1007/s10750-016-2935-z.

Hauer, C., B. Wagner, J. Aigner, P. Holzapfel, P. Flödl, M. Liedermann, M. Tritthart, C. Sindelar, U. Pulg, M. Klösch, M. Haimann, B. O. Donnum, M. Stickler and H. Habersack (2018). 'State of the art, shortcomings and future challenges for a sustainable sediment management in hydropower: A review'. *Renewable and Sustainable Energy Reviews* 98, pp. 40–55. ISSN: 1364-0321. DOI: 10.1016/j.rser.2018.08.031.

Hillebrand, G., I. Klassen and N. R. B. Olsen (2017). '3D CFD modelling of velocities and sediment transport in the Iffezheim hydropower reservoir'. *Hydrology Research* 48 (1), pp. 147–159. ISSN: 1998-9563. DOI: 10.2166/nh.2016.197.

Hjulström, F. (1935). 'Studies of the morphological activity of rivers as Illustrated by the river Fyris'. In: *Bulletin of the Geological Institute of the University of Uppsala*.

Hofland, B., J. A. Battjes and R. Booij (2005). 'Measurement of fluctuating pressures on coarse bed material'. *Journal of Hydraulic Engineering* 131 (9), pp. 770–781. ISSN: 0733-9429. DOI: 10.1061/(ASCE)0733-9429(2005)131:9(770).

Hsu, T. and P. Liu (2004). 'Toward modeling turbulent suspension of sand in the nearshore'. *Journal of Geophysical Research: Oceans* 109 (C6). ISSN: 2169-9275. DOI: 10.1029/2003JC002240.

Huang, C.-C., W.-C. Lin, H.-C. Ho and Y.-C. Tan (June 2019). 'Estimation of reservoir sediment flux through bottom outlet with combination of numerical and empirical methods'. *Water (Switzerland)* 11 (7). ISSN: 2073-4441. DOI: 10.3390/w11071353.

Hunt, J. N. and C. C. Inglis (1954). 'The turbulent transport of suspended sediment in open channels'. *Proceedings of the Royal Society of London. Series A. Mathematical and Physical Sciences* 224 (1158), pp. 322–335. DOI: 10.1098/rspa.1954.0161.

Hunziker, R. (1995). 'Fraktionsweiser Geschiebetransport'. *Mitteilungen der Versuchsanstalt für Wasserbau, Hydrologie und Glaziologie der Eidgenössischen Technischen Hochschule Zürich* 139, pp. 9–191.

Huppert, H. E. and J. E. Simpson (1980). 'The slumping of gravity currents'. *Journal of Fluid Mechanics* 99 (4), pp. 785–799. DOI: 10.1017/S0022112080000894.

IWHW – Insitut für Wasserwirtschaft, Hydrologie und konstruktiven Wasserbau (2016). *Proposal for the establishment and funding of a new Christian Doppler Laboratory*.

Joshi, J. B., K. Nandakumar, A. W. Patwardhan, A. K. Nayak, V. Pareek, M. Gumulya, C. Wu, N. Minocha, E. Pal, M. Kumar, V. Bhusare, S. Tiwari, D. Lote, C. Mali, A. Kulkarni and S. Tamhankar (2019). 'Computational fluid dynamics'. In: *Advances of Computational Fluid Dynamics in Nuclear Reactor Design and Safety Assessment*. Ed. by J. B. Joshi and A. K. Nayak. Woodhead Publishing Series in Energy. Duxford, United Kingdom: Woodhead Publishing. Chap. 2, pp. 21–238. ISBN: 978-0-08-102337-2. DOI: 10.1016/B978-0-08-102337-2.00002-X.

Kranenburg, W. M., T.-J. Hsu and J. S. Ribberink (2014). 'Two-phase modeling of sheet-flow beneath waves and its dependence on grain size and streaming'. *Advances in Water Resources* 72, pp. 57–70. ISSN: 0309-1708. DOI: 10.1016/j.advwatres.2014.05.008.

La Rocca, M., C. Adduce, G. Sciortino and A. Pinzon (2008). 'Experimental and numerical simulation of three-dimensional gravity currents on smooth and rough bottom'. *Physics of Fluids* 20 (10). ISSN: 1070-6631. DOI: 10.1063/1.3002381.

La Rocca, M., C. Adduce, G. Sciortino, A. Pinzon and M. Boniforti (2012). 'A two-layer, shallow-water model for 3D gravity currents'. *Journal of Hydraulic Research* 50 (2), pp. 208–217. ISSN: 0022-1686. DOI: 10.1080/00221686.2012.667680.

La Rocca, M., P. Prestininzi, C. Adduce, G. Sciortino and R. Hinkelmann (2013). 'Lattice Boltzmann simulation of 3D gravity currents around obstacles'. *International Journal of Offshore and Polar Engineering* 23 (3), pp. 178–185. ISSN: 1053-5381. DOI: 10.17736/10535381.

Lai, Y. G., J. Huang and K. Wu (2015). 'Reservoir turbidity current modeling with a two-dimensional layer-averaged model'. *Journal of Hydraulic Engineering* 141 (12). ISSN: 0733-9429. DOI: 10.1061/(ASCE)HY.1943-7900.0001041.

Launder, B. and D. Spalding (1974). 'The numerical computation of turbulent flows'. *Computer Methods in Applied Mechanics and Engineering* 3 (2), pp. 269–289. ISSN: 0045-7825. DOI: 10.1016/0045-7825(74)90029-2.

Lavelli, A., J. J. Boillat and G. De Cesare (2002). 'Numerical 3D modelling of the vertical mass exchange induced by turbidity currents in Lake Lugano (Switzerland)'. In: *Proceedings 5th International Conference on Hydro-Science and- Engineering (ICHE-2002)*. URL: http://infoscience.epfl.ch/record/103516.

Lee, F.-Z., J.-S. Lai, Y.-C. Tan and C.-C. Sung (2014). 'Turbid density current venting through reservoir outlets'. *KSCE Journal of Civil Engineering* 18, pp. 694–705. ISSN: 1976-3808. DOI: 10.1007/s12205-014-0275-y.

Lee, H. and S. Balachandar (2012). 'Critical shear stress for incipient motion of a particle on a rough bed'. *Journal of Geophysical Research: Earth Surface* 117 (F1). DOI: 10.1029/2011JF002208.

Liu, D., X. Liu and X. Fu (2018). 'LES-DEM simulations of sediment saltation in a rough-wall turbulent boundary layer'. *Journal of Hydraulic Research* 57 (6), pp. 1–12. DOI: 10.1080/00221686.2018.1509384.

Lobovský, L. and J. Křena (2007). 'Smoothed particle hydrodynamics modelling of fluids and solids'. *Applied and Computational Mechanics* 1, pp. 521–530.

Lysenko, D., Ertesvåg and K. I.S. & Rian (2012). 'Large-eddy simulation of the flow over a circular cylinder at reynolds number 3900 using the OpenFOAM toolbox'. *Flow Turbulence Combustion* 89, pp. 491–518. DOI: 10.1007/s10494-012-9405-0.

Maxey, M. and J. Riley (1983). 'Equation of motion for a small rigid sphere in a nonuniform flow'. *Physics of Fluids* 26 (4), pp. 883–889. ISSN: 1070-6631. DOI: 10.1063/1.864230.

Mazzuoli, M., P. Blondeaux, J. Simeonov and J. Calantoni (2018). 'Direct numerical simulation of oscillatory flow over a wavy, rough, and permeable bottom'. *Journal of Geophysical Research: Oceans* 123 (3), pp. 1595–1611. ISSN: 2169-9275. DOI: 10.1002/2017JC013447.

Mazzuoli, M. and M. Uhlmann (2017). 'Direct numerical simulation of open-channel flow over a fully rough wall at moderate relative submergence'. *Journal of Fluid Mechanics* 824, pp. 722–765. DOI: 10.1017/jfm.2017.371.

Meyer-Peter, E. and R. Müller (1948). 'Formulas for bed load transport'. In: *Proceedings of the 2nd Meeting of the International Association for Hydraulic Structures Research* (Stockholm, Sweden). International Association of Hydraulic Research, pp. 39–64.

Muste, M., K. Yu, I. Fujita and R. Ettema (2005). 'Two-phase versus mixed-flow perspective on suspended sediment transport in turbulent channel flows'. *Water Resources Research* 41 (10). ISSN: 0043-1397. DOI: 10.1029/2004WR003595.

Musumeci, R., A. Viviano and E. Foti (2017). 'Influence of regular surface waves on the propagation of gravity currents: Experimental and numerical modeling'.

*Journal of Hydraulic Engineering* 143 (8). ISSN: 0733-9429. DOI: 10.1061/(ASCE)HY.1943-7900.0001308.

Necker, F., C. Härtel, L. Kleiser and E. Meiburg (2002). 'High-resolution simulations of particle-driven gravity currents'. *International Journal of Multiphase Flow* 28 (2), pp. 279–300. ISSN: 0301-9322. DOI: 10.1016/S0301-9322(01)00065-9.

Necker, F., C. Härtel, L. Kleiser and E. Meiburg (2005). 'Mixing and dissipation in particle-driven gravity currents'. *Journal of Fluid Mechanics* 545, pp. 339–372. ISSN: 0022-1120. DOI: 10.1017/S0022112005006932.

Nezu, I. and R. Azuma (2004). 'Turbulence characteristics and interaction between particles and fluid in particle-laden open channel flows'. *Journal of Hydraulic Engineering* 130 (10), pp. 988–1001. DOI: 10.1061/(ASCE)0733-9429(2004)130:10(988).

NTNU – Norwegian University of Science and Technology (2019). *SSIIM*. URL: http://folk.ntnu.no/nilsol/ssiim/.

Olsen, N. R. B. (2018). *SSIIM*. Trondheim, Norway: Norwegian University of Science and Technology.

Ota, K., T. Sato and H. Nakagawa (2019). 'Quantification of spatial lag effect on sediment transport around a hydraulic structure using Eulerian–Lagrangian model'. *Advances in Water Resources* 129, pp. 281–296. ISSN: 0309-1708. DOI: 10.1016/j.advwatres.2017.11.009.

Paarlberg, A. J., M. Guerrero, F. Huthoff and M. Re (2015). 'Optimizing dredge-and-dump activities for river navigability using a hydro-morphodynamic model'. *Water (Switzerland)* 7 (7), pp. 3943–3962. ISSN: 2073-4441. DOI: 10.3390/w7073943.

Pahar, G. and A. Dhar (2017). 'Coupled incompressible smoothed particle hydrodynamics model for continuum-based modelling sediment transport'. *Advances in Water Resources* 102, pp. 84–98. ISSN: 0309-1708. DOI: 10.1016/j.advwatres.2017.02.003.

Parker, G. (1990). 'Surface-based bedload transport relation for gravel rivers'. *Journal of Hydraulic Research* 28 (4), pp. 417–436. DOI: 10.1080/00221689009499058.

Pope, S. B. (2000). *Turbulent Flows*. Cambridge: Cambridge University Press. 769 pp. ISBN: 978-0-521-59886-6.

Prasath, S. G., V. Vasan and R. Govindarajan (2019). 'Accurate solution method for the Maxey-Riley equation, and the effects of Basset history'. *Journal of Fluid Mechanics* 868, pp. 428–460. DOI: 10.1017/jfm.2019.194.

Rickenmann, D. (1991). 'Hyperconcentrated flow and sediment transport at steep slopes'. English. *Journal of Hydraulic Engineering* 117 (11), pp. 1419–1439. ISSN: 0733-9429. DOI: 10.1061/(ASCE)0733-9429(1991)117:11(1419).

Rickenmann, D. (2001). 'Comparison of bed load transport in torrents and gravel bed streams'. *Water Resources Research* 37 (12), pp. 3295–3305. ISSN: 0043-1397. DOI: 10.1029/2001WR000319.

Roache, P. J. (2009). *Fundamentals of verification and validation*. New Mexico, USA: Hermosa Publishers. ISBN: 978-0-913478-12-7.

Rouse, H. (1939). *An analysis of sediment transportation in the light of fluid turbulence*. California Institute of Technology.

Schmeeckle, M. W., J. M. Nelson and R. L. Shreve (2007). 'Forces on stationary particles in near-bed turbulent flows'. *Journal of Geophysical Research: Earth Surface* 112 (F2). DOI: 10.1029/2006JF000536.

Schobesberger, J., P. Lichtneger, C. Hauer, P. Habersack H. and C. Sindelar (2020). 'Three-dimensional coherent flow structures during Incipient particle motion'. English. *Journal of Hydraulic Engineering* 146 (5). ISSN: 0733-9429. DOI: 10.1061/(ASCE)HY.1943-7900.0001717.

Schobesberger, J., D. Worf, P. Lichtneger, S. Yücesan, C. Hauer, H. Habersack and C. Sindelar (2021). 'Role of low-order proper orthogonal decomposition modes and large-scale coherent structures on sediment particle entrainment'. *Journal of Hydraulic Research*. ISSN: 0022-1686. DOI: 10.1080/00221686.2020.1869604.

Schoklitsch, A. (1934). 'Der Geschiebetrieb und Geschiebefracht'. *Wasserkraft und Wasserwirtschaft* 29 (4).

Shields, A. (1936). 'Anwendung der Ähnlichkeitsmechanik und der Turbulenzforschung auf die Geschiebebewegung'. *Mitteilungen der Preußischen Versuchsanstalt für Wasser- Erd- und Schiffbau* 26.

Smagorinsky, J. (1963). 'General circulation experiments with primitive equations: I. the basic experiment'. *Monthly Weather Review* 91 (3), pp. 99–164. DOI: 10.1175/1520-0493(1963)091<0099:GCEWTP>2.3.CO;2.

Smart, G. and M. N. R. Jäggi (1983). 'Sedimenttransport in steilen Gerinnen'. *Mitteilungen der Preußischen Versuchsanstalt für Wasserbau, Hydrologie und Glaziologie der Eidgenössischen Technischen Hochschlule Zürich* 64, pp. 9–188.

Smart, G. and H. Habersack (2007). 'Pressure fluctuations and gravel entrainment in rivers'. *Journal of Hydraulic Research* 45 (5), pp. 661–673. DOI: 10.1080/00221686.2007.9521802.

Snider, D. (2001). ‘An incompressible three-dimensional multiphase particle-in-cell model for dense particle flows’. *Journal of Computational Physics* 170 (2), pp. 523–549. ISSN: 0021-9991. DOI: 10.1006/jcph.2001.6747.

Squires, K. D. and J. K. Eaton (1990). ‘Particle response and turbulence modification in isotropic turbulence’. *Physics of Fluids A: Fluid Dynamics* 2 (7), pp. 1191–1203. DOI: 10.1063/1.857620.

Stancanelli, L. M., R. E. Musumeci and E. Foti (2018a). ‘Computational fluid dynamics for modeling gravity currents in the presence of oscillatory ambient flow’. *Water (Switzerland)* 10 (5). ISSN: 2073-4441. DOI: 10.3390/w10050635.

Stancanelli, L. M., R. E. Musumeci and E. Foti (2018b). ‘Dynamics of gravity currents in the presence of surface waves’. *Journal of Geophysical Research: Oceans* 123 (3), pp. 2254–2273. ISSN: 2169-9275. DOI: 10.1002/2017JC013273.

Sun, R., H. Sun and H. Xiao (2017). ‘Realistic representation of grain shapes in CFD-DEM simulations of sediment transport with a bonded-sphere approach’. *Advances in Water Resources* 107, pp. 421–438. ISSN: 0309-1708. DOI: 10.1016/j.advwatres.2017.04.015.

Sun, R., H. Sun and H. Xiao (2018). ‘Investigating the settling dynamics of cohesive silt particles with particle-resolving simulations’. *Advances in Water Resources* 111, pp. 406–422. ISSN: 0309-1708. DOI: 10.1016/j.advwatres.2017.11.012.

Sun, Z. and J. Donahue (2000). ‘Statistically derived bedload formula for any fraction of nonuniform sediment’. *Journal of Hydraulic Engineering* 126. ISSN: 0733-9429. DOI: 10.1061/(ASCE)0733-9429(2000)126:2(105).

Tritthart, M., M. Liedermann, B. Schober and H. Habersack (2011a). ‘Non-uniformity and layering in sediment transport modelling 2: River application’. *Journal of Hydraulic Research* 49 (3), pp. 335–344. ISSN: 0022-1686. DOI: 10.1080/00221686.2011.583487.

Tritthart, M. (2005). ‘Three-dimensional numerical modelling of turbulent river flow using polyhedral finite volumes’. In: *Wiener Mitteilungen*. Vol. 193. ISBN: 3-85234-084-5.

Tritthart, M. (2012). ‘Numerical modelling in hydraulic engineering : hydrodynamics, sediment transport and simulation of hydroecosystems’. Habilitation. University of Natural Resources and Life Sciences, Vienna.

Tritthart, M. (2021). ‘Advanced modeling strategies for hydraulic engineering and river research’. *Water (Switzerland)* 13 (22). ISSN: 2073-4441. DOI: 10.3390/w13223261.

Tritthart, M. and D. Gutknecht (2007). 'Three-dimensional simulation of free-surface flows using polyhedral finite volumes'. *Engineering Applications of Computational Fluid Mechanics* 1 (1), pp. 1–14. DOI: 10.1080/19942060.2007.11015177.

Tritthart, M., M. Hengl, D. Rickenmann, M. Klösch and H. Habersack (2011b). 'Kapitel 3 – Mathematische Beschreibung'. In: *Fließgewässermodellierung – Arbeitsbehelf Feststofftransport und Gewässermorphologie*. Ed. by Bundesministerium für Land- und Forstwirtschaft, Umwelt und Wasserwirtschaft and Österreichischer Wasser- und Abfallwirtschaftsverband. Vienna, Austria, pp. 35–59. URL: https://www.oewav.at/Publikationen?current=294021&mode=form.

Tritthart, M., B. Schober and H. Habersack (2011c). 'Non-uniformity and layering in sediment transport modelling 1: Flume simulations'. *Journal of Hydraulic Research* 49 (3), pp. 325–334. ISSN: 0022-1686. DOI: 10.1080/00221686.2011.583528.

van Rijn, L. C. (1984a). 'Sediment transport, part I: Bed load transport'. *Journal of Hydraulic Engineering* 110 (10), pp. 1431–1456. ISSN: 0733-9429. DOI: 10.1061/(ASCE)0733-9429(1984)110:10(1431).

van Rijn, L. C. (1984b). 'Sediment transport, part II: Suspended load transport'. *Journal of Hydraulic Engineering* 110 (11), pp. 1613–1641. ISSN: 0733-9429. DOI: 10.1061/(ASCE)0733-9429(1984)110%3A11(1613).

van Rijn, L. C. (1993). *Principles of sediment transport in rivers, estuaries and coastal seas*. Amsterdam, The Netherlands: Aqua Publications.

Vinkovic, I., D. Doppler, J. Lelouvetel and M. Buffat (2011). 'Direct numerical simulation of particle interaction with ejections in turbulent channel flows'. *International Journal of Multiphase Flow* 37 (2), pp. 187–197. ISSN: 0301-9322. DOI: 10.1016/j.ijmultiphaseflow.2010.09.008.

Vowinckel, B., R. Jain, T. Kempe and J. Fröhlich (2016). 'Entrainment of single particles in a turbulent open-channel flow: a numerical study'. *Journal of Hydraulic Research* 54 (2), pp. 158–171. DOI: 10.1080/00221686.2016.1140683.

Wilcock, P. R. and J. C. Crowe (2003). 'Surface-based transport model for mixed-size sediment'. *Journal of Hydraulic Engineering* 129 (2), pp. 120–128. ISSN: 0733-9429. DOI: 10.1061/(ASCE)0733-9429(2003)129:2(120).

Wildt, D., C. Hauer, H. Habersack and M. Tritthart (2020). 'CFD modelling of particle-driven gravity currents in reservoirs'. *Water (Switzerland)* 12 (5). ISSN: 2073-4441. DOI: 10.3390/w12051403.

Wildt, D., C. Hauer, H. Habersack and M. Tritthart (2022a). 'LES two-phase modelling of suspended sediment transport using a two-way coupled Euler-Lagrange approach'. *Advances in Water Resources* 160. ISSN: 0309-1708. DOI: 10.1016/j.advwatres.2021.104095.

Wildt, D., C. Hauer, H. Habersack and M. Tritthart (2022b). 'Variability of shape and extent of a sediment plume in a two-way coupled LES model using an Euler-Lagrange approach'. In: *Proceedings of the 39th IAHR World Congress, 19–24 June 2022*. 39th IAHR World Congress "From Snow to Sea" (Granada, Spain).

Wildt, D. and M. Tritthart (2019). 'CFD modelling of turbidity currents'. In: *University of Architecture, Civil Engineering and Geodesy, International Jubilee Scientific Conference, Abstracts, 7–8 November 2019*. International Jubilee Scientific Conference 70th anniversary FHE of the UACEG (Sofia, Bulgaria), p. 48.

Wildt, D., S. Yücesan, C. Hauer, H. Habersack and M. Tritthart (2021). 'LES two phase modelling of suspended sediment transport using a two way coupled Euler-Lagrangian approach'. In: *6th IAHR Europe Congress Abstract Book*. 6th IAHR Europe Congress, 15–18 February 2021. Ed. by M. Kalinowska, P. Rowinski, T. Okruszko and M. Nones. Warsaw, Poland, pp. 643–644. ISBN: 978-83-66847-01-9. DOI: 10.24425/136660.

Wu, W., S. S. Wang and Y. Jia (2000). 'Nonuniform sediment transport in alluvial rivers'. *Journal of Hydraulic Research* 38 (6), pp. 427–434. DOI: 10.1080/00221680009498296.

Yücesan, S., J. Schobesberger, C. Sindelar, C. Hauer, H. Habersack and M. Tritthart (2022). 'Large Eddy Simulation of a sediment particle under entrainment conditions'. *Journal of Hydraulic Research* 60 (4), pp. 568–587. DOI: 10.1080/00221686.2021.2022026.

Yücesan, S., D. Wildt, P. Gmeiner, J. Schobesberger, C. Hauer, C. Sindelar, H. Habersack and M. Tritthart (2021). 'Interaction of very large scale motion of coherent structures with sediment particle exposure'. *Water (Switzerland)* 13 (3). ISSN: 2073-4441. DOI: 10.3390/w13030248.

Zhong, D., G. Wang and Q. Sun (2011). 'Transport equation for suspended sediment based on two-fluid model of solid/liquid two-phase flows'. *Journal of Hydraulic Engineering* 137 (5), pp. 530–542. ISSN: 0733-9429. DOI: 10.1061/(ASCE)HY.1943-7900.0000331.

Zhong, D., G. Wang and B. Wu (2014). 'Drift velocity of suspended sediment in turbulent open channel flows'. *Journal of Hydraulic Engineering* 140 (1), pp. 35–47. ISSN: 0733-9429. DOI: 10.1061/(ASCE)HY.1943-7900.0000798.